

## TOPICAL REVIEW

# Effects of confinement on freezing and melting

C Alba-Simionesco<sup>1</sup>, B Coasne<sup>2</sup>, G Dosseh<sup>1</sup>, G Dudziak<sup>3</sup>,  
K E Gubbins<sup>2</sup>, R Radhakrishnan<sup>4</sup> and M Sliwinska-Bartkowiak<sup>3</sup>

<sup>1</sup> Laboratoire de Chimie Physique, CNRS-UMR 8000, Bâtiment 349, Université de Paris-Sud, F-91405 Orsay, France

<sup>2</sup> Center for High Performance Simulation and Department of Chemical and Biomolecular Engineering, North Carolina State University, Raleigh, NC 27695-7905, USA

<sup>3</sup> Institute of Physics, Adam Mickiewicz University, Umultowska 85, 61-614 Poznan, Poland

<sup>4</sup> Department of Bioengineering, University of Pennsylvania, Philadelphia, PA 19104, USA

Received 15 August 2005, in final form 21 November 2005

Published 23 January 2006

Online at [stacks.iop.org/JPhysCM/18/R15](http://stacks.iop.org/JPhysCM/18/R15)

## Abstract

We present a review of experimental, theoretical, and molecular simulation studies of confinement effects on freezing and melting. We consider both simple and more complex adsorbates that are confined in various environments (slit or cylindrical pores and also disordered porous materials). The most commonly used molecular simulation, theoretical and experimental methods are first presented. We also provide a brief description of the most widely used porous materials. The current state of knowledge on the effects of confinement on structure and freezing temperature, and the appearance of new surface-driven and confinement-driven phases are then discussed. We also address how confinement affects the glass transition.

## Contents

1. Introduction	16
2. Methods and materials	19
2.1. Porous materials	19
2.2. Experimental methods	23
2.3. Molecular simulation and theoretical methods	30
3. Effect of confinement on structure and freezing temperature	37
3.1. Simple systems	37
3.2. Complex systems	44
4. New surface-driven and confinement-driven phases	49
4.1. Contact layer phases	49
4.2. Hexatic phase and two-dimensional melting	50
4.3. Glass transition in nanoporous materials	52
5. Global phase diagrams	57
6. Conclusion	59

Acknowledgments	60
References	61

## 1. Introduction

An understanding of freezing and melting in confined systems is of practical importance in lubrication, adhesion, nanotribology and fabrication of nanomaterials. The use of nanoporous materials as templates for forming nanomaterials such as composites, nanowires and nanotube arrays is receiving wide attention (e.g. [1–6]). Formation of the nanomaterial in the porous template is usually achieved by infiltration of molten material [2, 4, 5], vapour phase deposition [7] or electrochemical deposition [8]. Freezing in narrow pores is also of importance in understanding frost heaving and the distribution of pollutants in soils. Freezing in porous media has been widely employed in the characterization of porous materials using the method of thermoporometry [9]. In this method the change in the freezing temperature is related to the pore size through the Gibbs–Thomson equation.

The fundamental interest in this area is the desire to understand the new physics that occurs due to finite-size effects, surface forces and reduced dimensionality. Examples of such systems are phases confined within narrow pores, in reverse micelles, in the slit-shaped confined spaces involved in lubrication of magnetic hard disks and between the mica surfaces of the surface forces apparatus. Micro- and mesoporous materials (with pore widths under 2 and 2–50 nm, respectively) can have pores with approximately slit-shaped (e.g. activated carbon fibres, microporous boron nitride, clays), cylindrical (e.g. MCM-41, SBA-15) or spherical (carbon aerogels, mesocellular foams) geometry; simple models of the pore structure of these materials assume such simple geometries throughout the pore structure. On reducing the width of the confined space to approach the range of the intermolecular forces we can expect significant shifts in the freezing temperature, and in some cases we might anticipate new surface- or confinement-induced phases to occur. In such systems the confined phase is usually termed the *adsorbate* and the solid material in which it is confined is the *adsorbent*. As is the case for wetting phenomena and capillary condensation, we can anticipate that the physical behaviour of the confined system will be sensitive to the competition between the adsorbate–adsorbate and adsorbate–adsorbent intermolecular forces. These expectations are confirmed by experiment. The nature of these phases, their structure and properties (e.g. diffusion rates, shear properties etc) and their relation to the surface forces, pore dimensions and pore morphology and topology are of considerable interest, and are at present not well understood.

Although numerous complications (metastable states, surface heterogeneity, pore connectivity etc—see below) can occur in experimental systems, it is useful to consider the freezing and melting of a pure substance of spherical, non-polar molecules confined in non-connected pores of a single geometry (e.g. slit-shaped), and having homogeneous walls. Two intermolecular potentials are then involved, and if we neglect non-additivity we can write the pair potentials as  $u_{ff}(r) = \varepsilon_{ff}f(r/\sigma_{ff})$  and  $u_{fw}(r) = \varepsilon_{fw}f(r/\sigma_{fw})$ , where  $\varepsilon$  and  $\sigma$  are the usual energy (well depth) and molecular diameter parameters, respectively, and f and w denote fluid (adsorbate) and wall (adsorbent) molecules, respectively. By putting the configuration partition function for this system, and hence the free energy, in dimensionless form, it is easy to show that, at a given pressure, any phase transition temperature,  $T_{tr}^*$ , is a function of three dimensionless variables [10, 11]:

$$T_{tr}^* = f(H^*, \alpha, \sigma_{fw}/\sigma_{ff}), \quad (1)$$

where  $H^* = H/\sigma_{ff}$  and  $\alpha = C\varepsilon_{fw}/\varepsilon_{ff}$ , while  $T_{tr}^*$  is the reduced transition temperature, and can be written as  $T_{tr}^* = T_{tr}/T_{tr,bulk}$  or  $T_{tr}^* = kT/\varepsilon_{ff}$ , where  $T_{tr,bulk}$  is the corresponding transition temperature in the bulk fluid. The variable  $\alpha$  measures the ratio of the adsorbate–wall (fw)

to adsorbate–adsorbate (ff) attractive intermolecular potentials. The parameter  $C$  depends on the pore geometry and the nature of the wall material, and accounts for the arrangement and density of the wall atoms; for the Steele (10, 4, 3) potential for carbons, for example, it is [11]  $C = \rho_w \sigma_{fw}^2 \Delta$ , where  $\rho_w$  is the number density of the wall atoms (which is large for carbon) and  $\Delta$  is the spacing between layers of carbon atoms (the graphene layers). The parameter  $\alpha$  can be used to classify porous materials in studies on freezing and melting of confined fluids; adsorbents with  $\alpha > 1$  can be considered as ‘strongly attractive’ while those with  $\alpha < 1$  can be considered as ‘weakly attractive’. When the fluid/fluid and fluid/wall interactions are similar, the material can be referred to as exhibiting ‘intermediate attraction’. Although it depends on the adsorbate/adsorbent system that is being considered, such a classification is useful in qualitatively describing the freezing and melting behaviour of confined fluids. When the diameters  $\sigma_{fw}$  and  $\sigma_{ff}$  in equation (1) are not very different, and the pore width  $H$  comfortably exceeds the larger of these two values, then the partition function is only weakly dependent on the ratio  $\sigma_{fw}/\sigma_{ff}$  and one can approximate equation (1) as:

$$T_{tr}^* \approx f(H^*, \alpha). \quad (2)$$

Theoretical calculations and molecular simulations for such simple systems (Lennard-Jones molecules in slit-shaped pores) show that both of these variables are important in determining the behaviour of the confined fluid. The role of  $\alpha$  is to determine the qualitative change in the freezing temperature; for example, for small and moderate  $\alpha$  values, the freezing temperature is depressed relative to the bulk value, whereas for large  $\alpha$  it is raised, while the magnitude of shifts in transition temperatures depends on the pore width  $H^*$ . On the other hand, the appearance of new surface- or confinement-driven phases usually depends on a combination of effects from  $\alpha$  and  $H^*$ .

Both theoretical and experimental works in this field are beset with significant difficulties; the nature of the difficulties is different in the two cases, so that joint theoretical and experimental studies are advisable and can be rewarding. In theoretical or simulation work it is relatively straightforward to determine the structure of the confined phases, achievement of true equilibrium and the order of any transition; simulations offer the possibility of systematic studies of the effects of pore width, the nature of solid material, pore connectivity etc that are usually difficult to achieve in experiments. Difficulties in the simulation studies arise from: (a) limitations of the speed and memory of the computer, which in turn limit the size of the system that can be studied (to a million molecules or so, and around 30–50 nm box length in the case of atomistic simulations at present) and the real time that can be covered (up to about 100–1000 ns in molecular dynamics simulations); (b) uncertainty in the intermolecular forces; (c) uncertainty in the pore morphology and topology, and in the nature of the pore walls for most porous materials. Because of limitations of computer power it may be difficult to access the timescales needed to study some dynamical processes, e.g. shearing of and diffusion in thin confined films. This is also a severe limitation for the study of glassy transitions, which are characterized by a critical slowing down of the dynamical properties of the system.

On the experimental side, difficulties include: (a) determining the nature of the confined phase—it can be very difficult to distinguish between fluid, crystalline and glassy phases, for example; (b) distinguishing between long-lived metastable and true thermodynamic equilibrium states (determination of free energies is difficult and rarely attempted); (c) avoidance of spurious results due to surface contamination from impurities or nanoparticles; (d) smearing out of the transition range and determination of the order of the transition—when, if ever, is it first order?; (e) competition between the thermodynamics driving an order-disorder transition and the kinetics of the process, due to the slowing of the dynamics of the system when the temperature decreases.

A particular difficulty in the experiments, and to some degree in theoretical and simulation studies also, is the identification of a confined phase as solid, and the distinction between a crystalline phase and a glassy one. Bulk crystalline solids are characterized by long-range atomic positional and bond orientational order. Such long-range order can be detected experimentally through scattering experiments, and in atomistic simulations through determination of pair positional and bond order correlation functions. Thermal atomic motion is greatly reduced compared with fluid phases, the solid retains its shape and strongly resists shear, and diffusion is extremely slow or non-existent. Several theories and criteria for solid phases have been proposed. A commonly used criterion [12] for a solid phase is the magnitude of the structure factor at the first peak,  $S(k_0)$ . For an isotropic fluid the first peak occurs at  $k_0 = 2\pi/l$ , where  $l$  is the average intermolecular nearest neighbour distance. As the fluid is cooled  $S(k_0)$  increases, and molecular dynamics simulations show that for a three-dimensional (3D) fluid  $S(k_0)/S(k = \infty) \sim 2.7$  at the freezing point. For a two-dimensional (2D) fluid  $S(k_0)/S(k = \infty) \sim 5$  at the freezing point [13, 14]. Thus a value of  $S(k_0)$  greater than these values can be taken as indicative of a solid phase. This is known as the *Hansen–Verlet criterion*. Another commonly used condition for melting is the *Lindemann criterion* [15]: a crystal will melt when a temperature is reached at which the amplitude of vibration of the atoms is sufficiently large that the atoms invade the space of their nearest neighbours [16–18]. A third condition used to define the fluid-like or solid-like nature of the system is the *Born criterion*, according to which the shear strength characteristic of solids disappears on melting [19]. Other theories of melting include the dislocation theory of melting, according to which melting occurs due to a catastrophic proliferation of dislocations in the solid [20, 21, 17], and various nucleation theories of melting and freezing [22]. The dislocation theory of melting, which is most useful for 2D systems and is therefore useful for confinement in slit-shaped pores, is discussed in more detail in section 2.3.

Although these theories and criteria are useful for bulk systems, they are of limited use for freezing and melting in confined systems. For example, the geometry and very small volume of the confined film between the mica surfaces in the surface forces apparatus (SFA) have so far precluded using neutron or x-ray techniques to probe the film’s structure [23, 24]. Although bulk fluids do not appreciably resist shear, atomistic simulation and theoretical studies [25, 26] have shown that very thin fluid films confined between parallel walls do resist shear and can exhibit a limiting yield stress, similar to the behaviour of a solid film; however, the yield stress is smaller for fluid than for solid films. Both simulation and SFA experimental studies suggest that when solid phases form within a narrow pore they are considerably more defective than bulk crystals, again making it more difficult to identify solid phases within narrow pores and to distinguish between an amorphous glassy phase and a crystal.

In what follows we review the current state of knowledge from experiment and theory of freezing and melting in confined systems. Our emphasis is on fairly simple, neutral adsorbate molecules and well-characterized materials and surfaces; we do not explicitly consider complex adsorbates, such as ionic fluids [27, 28], polymers [29–31], liquid crystals [32–35], colloids [36–40] and amphiphilic molecules. Phase transitions in confined systems, including freezing and melting, were reviewed 6 years ago by Gelb *et al* [41]. Experimental studies of freezing and melting in confined systems have been reviewed by Christenson [42]; however, this review did not include coverage of theoretical or molecular simulation studies. The most useful atomistic simulation, theoretical and experimental methods are described in section 2; a brief description of the most widely used porous materials is also included. The effects of confinement on structure and freezing temperature, and the appearance of new surface-driven and confinement-driven phases are described in sections 3 and 4, respectively. Global phase behaviour is discussed in section 5, and conclusions in section 6.

**Table 1.** Various nanoporous materials.

Porous material	Surface chemistry	Pore shape	Pore width (nm)
<i>Ordered, regular:</i>			
Zeolite aluminosilicate	O, Si, Al	Cylinders, cages	0.3–1
Zeolite aluminophosphate	O, P, Al	Cylinders	0.8–1.3
Carbon nanotube	C	Cylinders	0.5–10
MCM-41	Si, O (H)	Cylinders	1–5
SBA-15	Si, O (H)	Cylinders (connected)	3–10
Porous silicon	SiH <sub>x</sub> ( $x = 1, 2, 3$ )	Polygonal cylinders	5–50
<i>Disordered:</i>			
Porous glass	Si, O (H)	Distorted cylinders	2.5–10 <sup>4</sup>
Silica xerogel, oxides	Si, O (H), . . .	Distorted cylinders	1–100
Silica aerogel	Si, O (H)	Pore voids	5–50
Carbon aerogel	C	Slits and pore voids	1.5–60
Activated carbon fibres	C	Slits	0.6–1.3
Pillared clay	O, Si, Al, . . .	Slits and pillars	0.5–2

## 2. Methods and materials

### 2.1. Porous materials

Nanoporous materials can be roughly classified into those with regular and ordered porous networks and those with disordered porous networks. Regular porous materials include solids with either crystalline (zeolites, porous silicon, carbon nanotubes) or amorphous (MCM-41, SBA-15) pore walls. For these porous solids, the structure can usually be determined using x-ray or neutron diffraction. However, some uncertainties remain regarding their surface roughness and chemistry (presence of cations, impurities and/or water species on the pore surface). In contrast to regular porous solids, there is no direct and simple way to determine the structural properties of disordered porous materials, due to the complexity of their pore network and their amorphous nature. Some commonly used nanoporous materials, with their pore shape and estimated size range, are shown in table 1.

*Ordered porous materials.* Among regular porous solids, zeolites are those with the best-defined structure. They are crystalline materials that can be prepared with various pore shapes, depending on the symmetry group of the crystal structure [43, 44]. They usually contain oxygen and aluminium atoms and either silicon (aluminosilicate) or phosphorus atoms (aluminophosphate). Some zeolite porous materials contain only oxygen and silicon atoms (silica). Zeolite porous networks are made of straight microporous (pore size less than 2 nm) channels and/or quasi-spherical cages. The pore size can vary from 0.3 to 1 nm for aluminosilicate zeolites and from 0.8 to 1.3 nm for aluminophosphate zeolites.

Carbon nanotubes are hollow carbon cylinders that can be obtained by depositing dense carbon vapour on catalyst surfaces using either an electric arc or laser ablation. Their structure can be modelled by rolling one (single-walled nanotube) or several (multi-walled nanotube) graphene sheets to form a cylinder [45, 46]. Transmission electronic microscopy (TEM) images of carbon nanotubes with different numbers of concentric layers are shown in figure 1(a) [47]. The inner diameter of carbon nanotubes can be varied from 0.5 to 2 nm for single-walled materials and from 2 to 10 nm for multiwalled nanotubes. A common property of carbon nanotubes and zeolites is their large aspect ratio (about 10<sup>4</sup>), defined as the characteristic length of the pores divided by their mean diameter. This feature has attracted great attention since it

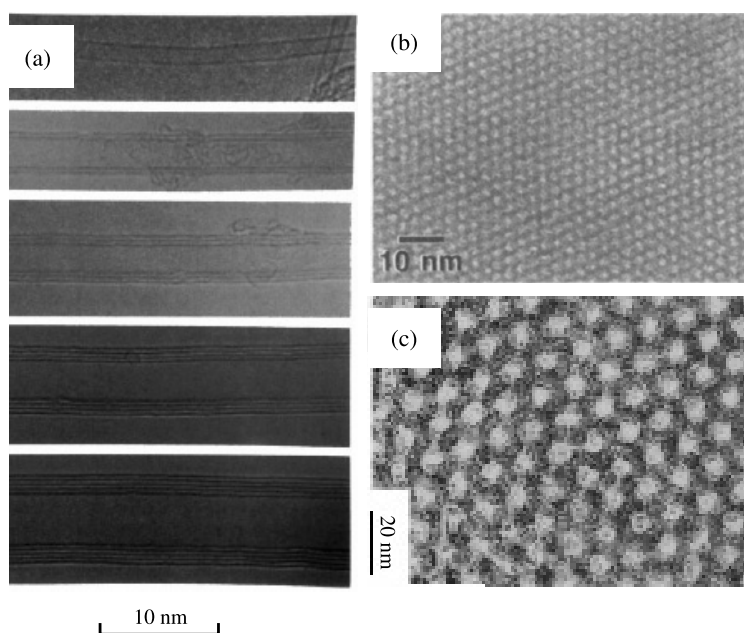


**Figure 1.** TEM images of regular nanoporous materials. (a) Transverse views of carbon nanotubes with increasing numbers of concentric tubes, one to five layers from top to bottom (from [47]). (b) MCM-41 materials having 2.0 nm cylindrical pores (from [48]). (c) SBA-15 materials having 6.0 nm cylindrical pores (from [51]).

allows one to study the behaviour of (quasi) one-dimensional systems. In contrast, porous oxide ceramics MCM-41 are characterized by smaller aspect ratios,  $10^2$ – $10^3$ ; the pore length is about  $1\ \mu\text{m}$  and the pore size between 1 and 10 nm [48]. These materials consist of cylindrical silica mesopores packed into a hexagonal array (figure 1(b)). MCM-41 is obtained by a template mechanism involving amphiphilic surfactant molecules [49, 50]. The structural properties of MCM-41 have been well characterized by combining TEM, x-ray diffraction and adsorption experiments. However, the exact surface chemistry (impurities, silica defects) and surface texture (microporosity or surface roughness) is not well understood. The pore size of MCM-41 depends on the chain length of the surfactant molecules, but the porous structure is unstable for pore sizes larger than 5 nm due to constraints on the 0.5–1 nm thick silica walls. Zhao *et al* [51] have obtained a new generation of mesoporous oxide ceramics with larger pores than 5.0 nm (up to 10 or 20 nm) by replacing the amphiphilic molecules by block copolymers in the template process. As shown in figure 1(c), these materials, named SBA-15, exhibit a similar structure to that of MCM-41 but with thicker pore walls ( $\sim 3$ – $4$  nm), improving the stability of the porous structure [51]. It has been shown that the main mesopores in SBA-15 materials are connected *via* transverse microporous channels, formed by the calcination of hydrophilic blocks enclosed in the silica substrate [52, 53].

Porous silicon is a nanoporous material that exhibits either an ordered or a disordered porous network, depending on the level and type of doping of the initial compact substrate [54]. This material is obtained by electrochemical dissolution of single-crystal silicon wafers in a hydrofluoric acid solution. For highly boron-doped substrates (type  $\text{P}^+$ ), the porous network is a honeycomb-like structure of straight parallel tubular pores. Pores have polygonal shapes and the size dispersion is large. The mean pore size can be varied from 5 to 50 nm and

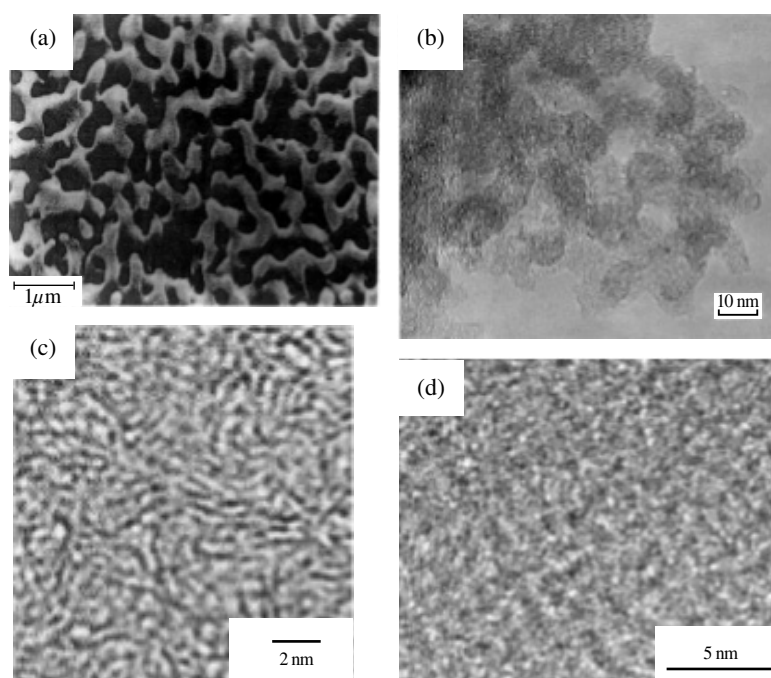


**Figure 2.** Electron microscopy images of disordered nanoporous materials. (a) Scanning electron micrograph of a controlled porous glass (from [55]). (b) TEM picture of a carbon aerogel (from [59]). (c) TEM image of an activated carbon obtained from coconut shell (from [62]). (d) TEM picture of an activated carbon fibre (from [65]).

the pore length from 1 to few hundred micrometres, depending on the synthesis conditions. It has been shown that, for very high doping levels, pores of this  $P^+$ -type material have no or little interconnection. Porous silicon solids obtained from P-type (lightly boron doped) and N-type (phosphate doped) silicon substrates exhibit a very different structure from that described above. For these doping types, the porous structure is a random network of spherical microporous cavities, which are strongly interconnected (sponge-like morphology) [54]. For these samples, the mean pore size is between 1 and 5 nm. Studies of the surface chemistry of porous silicon have shown that the inner surfaces of the pores are covered by hydride groups,  $\text{SiH}_x$  ( $x = 1, 2$  or  $3$ ), which are stable for a few days.

*Disordered porous materials.* Most of the early experiments on freezing/melting in confined geometry were performed with disordered porous materials. Controlled pore glasses (CPG), including Vycor glass, constitute a large family of disordered porous materials (figure 2(a)) [55]. They are prepared by heating a mixture of oxides ( $\text{SiO}_2$ ,  $\text{B}_2\text{O}_3$ ,  $\text{Na}_2\text{O}$  usually; in some cases  $\text{Al}_2\text{O}_3$  is also present) to about  $1200^\circ\text{C}$  to produce a miscible liquid mixture, followed by quenching into the spinodal region at about  $700^\circ\text{C}$ . Provided that the initial composition is not too far from the critical mixing value, the mixture starts to separate into two phases, one of which (the  $\text{B}_2\text{O}_3$ -rich phase) becomes a connected phase of roughly cylindrical geometry, while the other is nearly pure silica. If left at this temperature the diameter of the cylinders grows. When the desired diameter is reached, the mixture is quenched to room temperature to form a glass, the  $\text{B}_2\text{O}_3$ -rich phase is removed with an acid leaving the connected cylindrical pore structure, and the resulting silica structure is annealed. Controlled pore glasses

exhibit a disordered porous structure of interconnected pores (for a characterization study of Vycor, see [56]). The pore size distribution is narrow ( $\pm 20\%$ ), although pores have a distorted cylindrical shape. The mean pore size depends on the time the system is kept in the separation process, and varies from 2.5 up to  $10^4$  nm.

Porous oxides (particularly silica) are prepared using a sol–gel technique [57]. Starting with a gel formed by oxide solid particles in an aqueous solution, the solvent is removed by drying the system. This process leads to a disordered porous material, called *xerogel*, having both micropores and highly distorted cylindrical mesopores. These materials exhibit wide pore size distributions, with a mean pore size that can be from 1 to  $10^2$  nm. During the drying process there is a considerable shrinkage of the porous structure, which leads to an important reduction of the pore space. However, the liquid solvent can be replaced by a gas or a supercritical fluid during the drying stage in order to keep the highly porous structure of the wet gel. Using this modified sol–gel technique, porous solids (called *aerogel*) with very high porosity and larger pores than the *xerogel* materials can be obtained. In the case of *aerogels*, the mesoporosity consists of spherical solid particles separated by pore voids, rather than tubular pores. Silica *aerogels* can be obtained by replacing the water solvent by alcohol and heating the sample at a temperature above the alcohol critical temperature [57]. Carbon *aerogels* are prepared from the pyrolysis of an organic resorcinol/formaldehyde mixture using supercritical  $\text{CO}_2$  [58, 59]. Carbon materials obtained using this process have wide pore size distributions centred on a mean value that can vary from 1.5 to 60 nm [60] (see figure 2(b)). The main advantages of aerogels and xerogels are their easy preparation (pressure and temperature close to atmospheric conditions) and their wide range of pore sizes.

Activated carbons constitute another important family of porous carbons [60]. They are prepared by first pyrolysing organic compound precursors (saccharose, wood, coconut shells, coal, polymers, pitch etc). This leads to a dense carbon material in which the porosity consists of mostly closed pores [61, 62]. Then, pores are opened using either a physical (high-temperature treatment in the presence of  $\text{CO}_2/\text{H}_2\text{O}$  gas) or a chemical (involving reactions with acid compounds) activation process. Activated carbons are disordered porous materials with quasi-slit-shaped micropores of various widths [60] (see figure 2(c)). The degree of disorder of these nanoporous substrates depends on both the initial precursor and the heat treatment temperature. Pikunic *et al* [63] have developed a method to build realistic models of activated carbons. They modelled a series of cokes formed by pyrolysis of saccharose, showing that the porous structure is strongly disordered. By contrast, activated carbon fibres obtained from carbonization of polymers or isotropic pitch fibres consist of well-ordered though somewhat defective graphene microcrystals [64, 65] (see figure 2(d)).

Another class of nanoporous materials are pillared structures, which exhibit both micro- and mesoporosities [66]. These materials are obtained by transforming an inorganic layered compound (mineral clays, metal oxide phosphate, layered double hydroxides etc) into a chemically and thermally stable porous material that keeps the layer structure. This is done by introducing pillars between layers of the initial layered structure. This pillaring process involves several steps including swelling of the layered structure in a polar solvent, ion exchanges between the sample and the pillared agent and calcination of the sample [66]. Only materials with charged layers such as clays can be pillared (the solid must have cationic exchange capacity). The pillared clays (kaolinite, mica, smectite. . .) usually contain O, Si, H, Al and P atoms. The microporosity of these materials is due to spacing between clay layers, while mesoporosity consists of pore voids between clay particles. Pillared structures are usually modelled as a disordered assembly of slit pores having a width of about 0.5–2 nm and a length of  $10^2$ – $10^3$  nm, respectively [67–69]. However, the exact pore size and shape distributions are not well characterized and require further investigation.

## 2.2. Experimental methods

Experimental studies of the effects of confinement are aimed at determining the nature of freezing or melting, the temperature at which transitions occur, the enthalpy changes associated with the transitions and the structure and properties of the confined phases. We present here brief descriptions of some of the most commonly used methods, together with an analysis of their advantages and drawbacks. The range of application of some of these methods is schematically summarized in figure 3.

### 2.2.1. Phase transition temperatures and enthalpy of melting

*Differential scanning calorimetry* is one of the most convenient methods when dealing with phase transitions that involve thermal events such as melting, freezing, allotropic transformation or glass transition [70]. This method measures the temperatures and the heat flow associated with the transitions as a function of time and temperature. Using only a small amount of sample (a few mg) it provides the temperatures, breadths and enthalpies of transition for any endothermic or exothermic processes related to changes in the heat capacity. Variations of transition temperatures with respect to the bulk and occurrences of new metastable phases may appear on the DSC scan. However, the method has a poor sensitivity for confined fluids or solids; thermal events as well as some phase transitions, and especially glass transitions, may not be detected because of the very small amount of material inside the pores. Moreover it is not possible to determine the absolute value of the specific heat, in contrast to adiabatic calorimetry (see below). The main weakness of DSC lies in the calculation of phase transition enthalpies in confined materials. It is well known that in narrow pores (widths up to a few tens of molecular diameters) crystallization is usually partial [71, 72]. As the determination of the fraction of each phase in the sample is not possible by DSC, the transition enthalpies of confined materials are probably underestimated [73]. Nevertheless, DSC remains one of the most appropriate and accessible methods for the study of phase transition in confined materials [74]. Temperature modulated differential scanning calorimetry (TMDSC) can also be employed, in particular for the differentiation of overlapping transitions. TMDSC is a modification of DSC in which a sinusoidal modulation of the heating rate is superimposed on top of the constant heating ramp usually applied in conventional DSC experiments. This modulation is usually sinusoidal with frequencies ranging from  $10^{-3}$  to  $3 \times 10^{-2}$  Hz, and the heating rate is often around  $1 \text{ K min}^{-1}$  [75]. Depending on the underlying heating rate and the period and amplitude of the modulation, weak transitions can be detected. The resulting heat flow measured is separated into a reversible part attributed to thermodynamic processes and a non-reversible part due to time-dependent (kinetic) processes in the sample. One of the advantages of TMDSC compared with conventional DSC is its sensitivity and resolution, which allows the use of small samples, and the separation of signals which overlap in conventional DSC.

*Adiabatic calorimetry.* Unlike DSC, adiabatic calorimetry allows a precise and absolute determination of the heat capacity of a given sample [76]. Moreover, the size of cell used in adiabatic calorimetry experiments is important ( $1\text{--}10 \text{ cm}^3$ ) and the thermal events are easily detectable, even for confined systems. The absolute heat capacity of confined liquids is obtained with an accuracy of  $\sim 3\%$ , after subtraction of the empty cell and matrix heat capacities, and for a typical sample mass of only  $300\text{--}500 \text{ mg}$  [77]. Heat capacity measurements are performed following an intermittent heating after a quench to the lowest temperature at moderate cooling rates. As for DSC measurements, the transition appears very broad. However, the contribution of extra modes coming from the surface interaction between the wall and the fluid is not clear and not well evaluated. The limitation of this method lies essentially in the fact that very few laboratories have adiabatic calorimeters, and the experiments are quite tedious to perform [77].

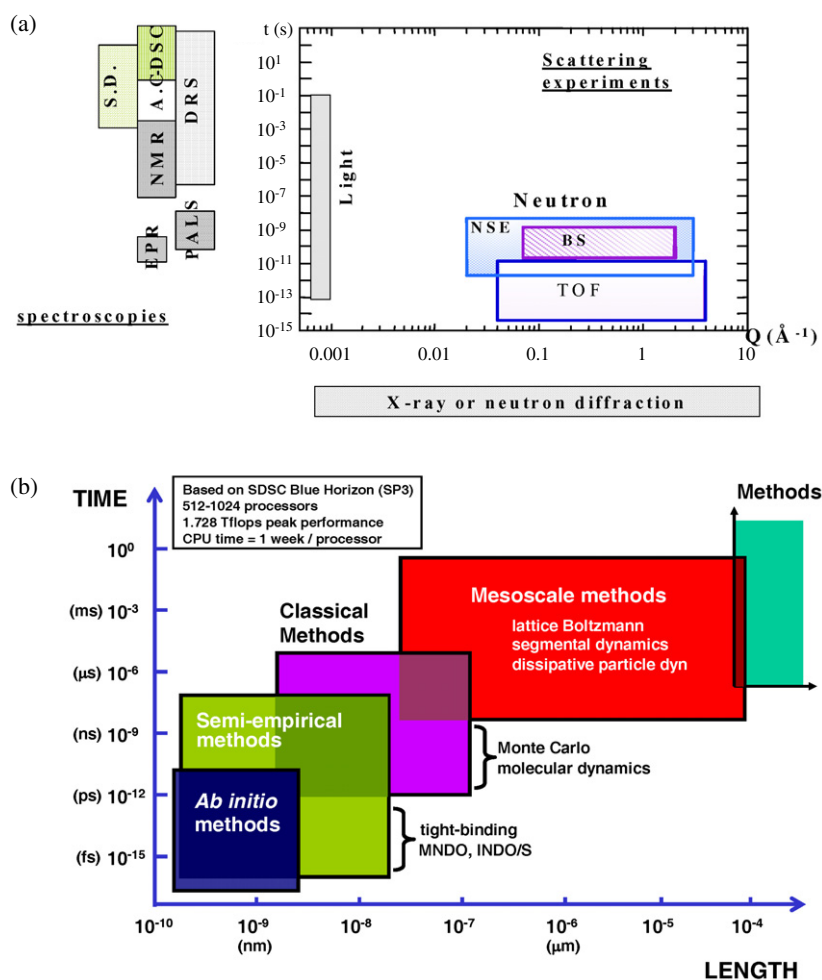


**Figure 3.** (a) Time and space scales of experiments discussed in the text for the study of thermodynamic, structural and dynamical properties of a confined fluid and its melting/freezing phase transition. Spectroscopies: adiabatic calorimetry (AC), differential scanning calorimetry (DSC), nuclear magnetic resonance (NMR), dielectric relaxation spectroscopy (DRS) and the nonlinear dielectric effect, solvation dynamics (SD), positronium annihilation lifetime spectroscopy (PALS), electron paramagnetic resonance (EPR). Scattering experiments: light, quasi-elastic neutron scattering including time of flight (TOF), backscattering (BS), neutron spin echo (NSE), elastic neutron and x-ray scattering. (b) Current range of applicability of various theoretical techniques in terms of the typical length and timescales that can be accessed at present. Based on the use of efficient, parallelized codes, and runs of 1 week using 512 processors on the IBM SP3 machine at the San Diego Supercomputer Center.

(This figure is in colour only in the electronic version)

*Nuclear magnetic resonance (NMR)* is widely used for investigations on confined materials [78–83]. NMR spectroscopy measures the absorption of electromagnetic radiation during the transitions between spin states of atomic nuclei. In NMR experiments, a strong constant field  $B_0$  and an oscillating field  $B_1$ , which causes absorption of energy, are applied to the sample. The energy absorbed by a given nucleus  $E = \gamma \hbar B_0 (1 - \sigma)$  depends on its

electronic environment, and consequently on the structural properties of the sample, through its chemical shielding constant,  $\sigma\gamma$ , is an isotope-dependent property called the gyromagnetic ratio. This technique is selective as one, two or even three different isotopes can be observed at once. NMR spectroscopy provides information on both the structure and dynamics of the system by chemical shift measurements and analysis of the relaxation properties, respectively. Solid state NMR is complementary to x-ray (XRD) or neutron diffraction, since crystalline, amorphous materials as well as powders can be investigated. While XRD provides information about the long- and short-range ordering and periodicities, NMR spectroscopy is a powerful technique to get information on the local environment of the nuclei. High-resolution solid state NMR of nuclei such as  $^{29}\text{Si}$ ,  $^{27}\text{Al}$ ,  $^{31}\text{P}$  or  $^{17}\text{O}$  NMR is currently used for the characterization of micro- or mesoporous materials [84–86]. Other nuclei, which can substitute for the usual framework elements in mesoporous materials, such as  $^{11}\text{B}$ ,  $^{73}\text{Ge}$  and  $^{69,71}\text{Ga}$  or other metals are observable by solid state NMR. Probe molecules like water and hydrocarbons have been used to study the pore architecture of mesoporous materials by monitoring the  $^1\text{H}$  NMR intensity of the liquid water signal when decreasing the temperature (thermoporosimetry) [87]. Finally, two-dimensional solid state heteronuclear NMR is used to investigate the connectivity of pore channels in porous materials such as zeolites. One group of NMR experiments embodies all the techniques based on chemical shift measurements, including liquid state NMR or solid state magic angle spinning NMR, multinuclear and sometimes multidimensional experiments such as chemical shift correlations. By detecting the environment of the nuclei, they help to locate them in the sample and relate these findings to the structure. Therefore, NMR is expected to detect events that lead to changes in the interactions between magnetic nuclei such as crystallization, melting or progressive thermal activation of molecular mobility, and provide a suitable method for the determination of phase transitions, when the DSC scans present phase changes over a very broad range of temperatures, as in the case of confined systems. Moreover, depending on the experimental conditions, NMR may be quantitative, and well-established methods such as line-shape analysis allow a precise determination of the amount of matter in each phase. Also, a combination of NMR line-shape analysis and DSC can give precise information on the thermal events in the samples [72]. As for other experimental techniques, one limitation in NMR studies of confined systems is the small amount of material in the pores. Combined with the inherent lack of sensitivity of some heteronuclei, NMR experiments can require prohibitive times when quantitative measurements have to be performed. The second limitation lies in a decrease of spectral resolution that is caused by the slowing down of molecular motions in the liquid phases, and the magnetic field inhomogeneities due to the porous material.

*Positron annihilation lifetime spectroscopy (PALS)* is based on a unique ability of the small *ortho*-positronium (*o*-Ps) probe to be localized in the regions of low electron density, such as vacancies in crystals or the so-called free volume holes in amorphous systems. The *o*-Ps probe works only in relatively rigid media with average relaxation times larger than its lifetime  $10^{-9}$  s. It provides a suitable local probe for phase transitions in confined geometry, as it is sensitive to open voids within the pore. Positron and positronium (Ps) annihilation techniques have been successfully applied to investigate the phase behaviour of adsorbed materials. However, the analysis of data for confined systems is likely to be complex and depend on the nature and density of the fluid [88–90].

*Surface forces apparatus (SFA)*. The SFA, originally developed by Tabor and co-workers [91–93], allows measurements in air or vacuum of the normal force between two solid surfaces. The apparatus was subsequently modified to study the forces between the two surfaces when separated by a vapour, liquid or solid [94–96]. While mica, because of its molecularly smooth and chemically inert surface and ease of handling, has been the primary material used

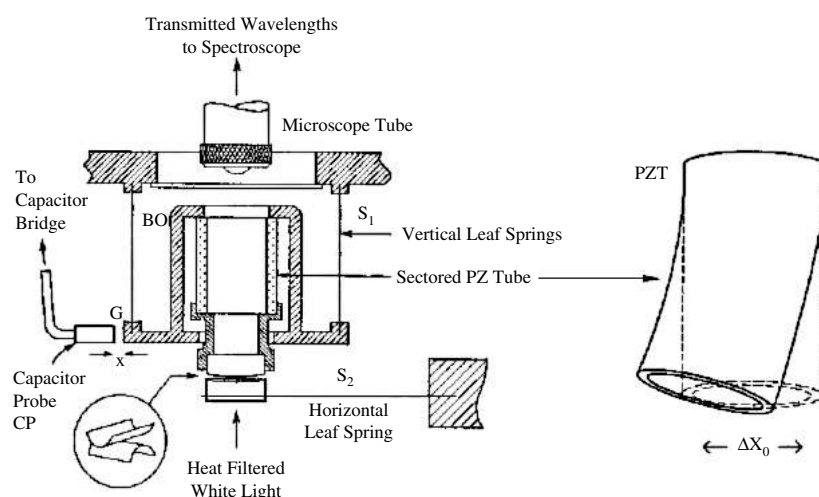


**Figure 4.** Schematic diagram (approximately to scale) of the shear force balance by Klein and Kumacheva [114]. The two mica sheets are mounted on cylindrical quartz lenses in a crossed-cylinder configuration (see inset). The top lens is mounted on a sectored piezoelectric tube (PZT), shown blown up on the right and illustrating the sideways motion induced when opposing sectors in the  $x$ -direction experience equal and opposite potentials. The PZT is mounted via a rigid stainless steel boat BO onto two vertical copper–beryllium leaf springs  $S_1$  (spring constant  $K = 15\,300\text{ N m}^{-1}$ ) which are rigidly mounted into the main body of the balance. Lateral forces between the mica surfaces are transmitted to the springs  $S_1$ , whose bending changes the thickness  $x$  of the air gap  $G$  between the boat BO and a capacitance probe CP. This is monitored by the change in capacitance of  $G$  (measured with a capacitor bridge). Normal forces are measured via the bending of the horizontal stainless steel leaf spring  $S_2$  (spring constant  $K = 25\,150\text{ N m}^{-1}$ ), whose motion is a perfect up–down one without tilt (the single cantilever representation of  $S_2$  is for simplicity). The distance  $D$  between the mica surfaces is measured as usual via the fringes of equal chromatic order originating from the white light after projection onto the slit of the spectroscopie. From Klein and Kumacheva [114].

in SFA measurements, other materials are possible, including sapphire and silica sheets [97, 98] and carbon and metal oxide [99]. In the usual method, the two transparent mica sheets (typically  $\sim 2\ \mu\text{m}$  thick) are coated with a semireflecting layer of silver and then attached to cylindrical quartz lenses ( $R \sim 1\text{ cm}$ ) which are arranged in a crossed-cylinder configuration. The closest separation,  $H$ , between the two mica surfaces as well as the refractive index of the confined phase can be measured by an optical technique using multiple beam interference fringes called fringes of equal chromatic order (FECO).  $H$  can be varied from zero up to micrometres with an accuracy of  $0.1\text{ nm}$ , using a piezoelectric crystal. The normal force  $F(H)$  is measured using sensitive springs. It is also possible to study the lateral force,  $F_{\text{shear}}(H)$ , when the confined film is sheared. Forces and adhesion/interfacial energies are determined accurately to within  $10^{-8}\text{ N}$  and  $10^{-3}\text{ mJ m}^{-2}$ , respectively. A SFA developed by Klein and co-workers [100, 101], which provides for measurement of both normal and lateral forces, is shown in figure 4. The SFA is unique in providing a means to study confinement in a single pore of simple (essentially slit-shape) geometry, without complications due to wall roughness, variations in pore shape, pore connectivity and disorder. However, a limitation with current apparatus is that while  $H$  can be varied over a wide range, the range of temperatures that is accessible is quite limited. Also, care is needed in preparing the mica surfaces to ensure that they are clean and molecularly smooth. Mica readily attracts water, organics and other pollutants or impurities, due to the high concentration of potassium ions near the surface. The mica sheets

are usually prepared by cutting them with a heated platinum wire, and care must be used to follow well-established procedures to avoid surface contamination by platinum nanoparticles. These procedures, together with means of detecting impurities on the surface, have been the subject of several recent studies [102–105].

### 2.2.2. Structure and density of the confined phase

*Elastic neutron and x-ray diffraction* are the methods of choice for the study of structure within the pore. Moreover, the density of the confined system can be determined by neutron diffraction. In order to examine both the matrix and the confined phase, elastic neutron scattering experiments must cover an extended momentum transfer range, 0.001–10 Å<sup>-1</sup>; the contribution from the matrix–matrix correlations can be removed by subtraction of a properly weighted spectrum of the empty sample.

*Wide angle neutron scattering* ( $Q > 0.5 \text{ \AA}^{-1}$ ) is a major experimental tool to analyse the local structure of condensed matter. In the case of a confined material it provides information about the nature of the phase—liquid, amorphous or crystalline—so that phase transitions are directly established [106–109]. The Bragg peaks of the confined system are broadened by excluded volume effects, and one may estimate the size of crystallites within the pore from the peak width. However, a quantitative description of the changes in the local structure of the confined fluid requires a more refined analysis, taking excluded volume effects and cross-correlation terms into account. Excluded volume effects specific to the pore geometry may significantly distort their shapes and must be considered before a quantitative structural description can be made [110–112].

*With small angle neutron scattering* ( $Q < 0.3 \text{ \AA}^{-1}$ ), the scattered neutron intensity of the porous material exhibits either Bragg peaks arising from the arrangement of the cylindrical pores in materials such as MCM-41 or SBA-15, or interaction peaks between pores in disordered materials such as CPG, Vycor or microemulsions. Such peaks provide a unique way to estimate the density of confined liquids, because their intensity  $I$  is related to the square of the contrast, defined as the difference of the scattering length density  $\rho\bar{b}$  between the porous matrix and the pore content:

$$I = A(\rho_{\text{wall}}\bar{b}_{\text{wall}} - \rho_{\text{fill}}\bar{b}_{\text{fill}})^2, \quad (3)$$

where  $A$  is a constant term,  $\bar{b}$  is the average coherent scattering length and  $\rho$  is the number density of atoms of the wall or the filler. A possible error of less than a few per cent due to either the wall density (estimated as the bulk density), the amount of material (that could be as large as 2 cm<sup>3</sup>) or the loading of the fluid cannot be excluded. On the other hand, this systematic error does not have any effect on its relative temperature dependence; the change in the slope of the thermal expansivity of the confined system provides an accurate location of any glass transition, while an abrupt variation indicates a freezing process, that may be confirmed by the presence of Bragg peaks at larger angle (see results for benzene confined in SBA-15 in figure 5 [113]).

*2.2.3. Fluid–solid characterization via dynamical properties.* NMR based on relaxation properties provides the time and length scales of molecular motions and, therefore, is suitable for collecting information on the dynamics of confined phases. Spin relaxation properties depend on the molecular motions in the confined system and consequently on the nature of the phase, and the line widths depend on the relaxation times. Transport properties can be investigated on different length scales from nanometres (by field cycling relaxometry [115, 116]) to micrometres (by field gradient diffusometry) and even centimetres

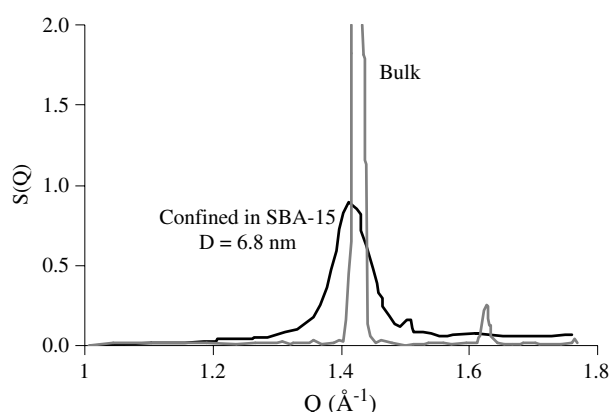


**Figure 5.** Bragg peaks of crystalline benzene as measured by elastic neutron scattering: in bulk (well resolved) and in confined geometry with a pore diameter of roughly  $14\sigma$ . The symmetry is orthorhombic with lattice parameters  $a = 7.460 \text{ \AA}$ ,  $b = 9.666 \text{ \AA}$  and  $c = 7.034 \text{ \AA}$ , which is not altered by confinement. However, a strong broadening of the peak is observed (adapted from Xia *et al* [113]).

(by NMR microimaging). Eventually, multidimensional solid state deuterium or carbon NMR can cover a wider range of timescales (up to seconds, not illustrated in figure 3). Because of its sensitivity  $^1\text{H}$  is the most commonly used nucleus where organic compounds are concerned. However, as proton spin–lattice relaxation depends on both the translational and rotational properties, the interpretation of results is complicated. As deuterium spin–lattice relaxation depends only on rotational properties, isotopic substitution of  $^1\text{H}$  by  $^2\text{H}$  is often used for the investigation of dynamical properties of organic adsorbates.

*Neutron quasi-elastic or inelastic scattering* experiments are suitable for studying the dynamics of confined phases. Motions in the time range from  $10^{-14}$  to  $10^{-9}$  s can be investigated by time of flight (TOF), backscattering (BS) and neutron spin echo (NSE) experiments in a  $Q$  range from  $0.01$  to  $5 \text{ \AA}^{-1}$ . On this timescale, the spectra depend on various types of motion from atomic and molecular vibrations (vibrational density of state) to reorientational motions and diffusion, and thus help in distinguishing between liquid and solid states. Because of the large incoherent scattering length of hydrogen, incoherent scattering functions provide information on the dynamics of individual hydrogen atoms in hydrogenated compounds (the self part of the dynamical structure factor  $S(Q, \omega)$ , where  $\omega$  is the frequency), whereas deuterated compounds are used to monitor collective molecular motions (pair correlation functions). However, due to the matrix Bragg peaks, only data at  $Q > 0.8 \text{ \AA}^{-1}$  can be reasonably taken for the analysis. The residual contribution of the empty matrix is always measured and can be subtracted, but in most cases 80% of the signal comes from the confined fluid. Corrections are delicate, because of cross-correlation matrix/fluid terms, possible adsorption of water by the empty matrices and rotational dynamics of the functional groups grafted at the surface (even deuterated). From the temperature dependence of the incoherent scattering function  $S(Q, \omega)$ , the elastic part of the scattering,  $S_{\text{el}}(Q, T)$  is operationally defined by the integral of  $S(Q, \omega)$  over  $\omega$  within the resolution in frequency width of the spectrometer. After its normalization at very low temperature, where no relaxation processes are expected, one obtains a Debye–Waller factor,  $W(Q, T)$ , and a mean square displacement  $u^2(T)$  from its dependence on  $Q$ .  $u^2(T)$  provides a measure of the amplitude of the motions at the timescale specific for the instrument (usually a nanosecond or a few

picoseconds); it discriminates between a glass or a crystal, and its departure from harmonic behaviour establishes a glass transition or a melting process very accurately [117, 118]. Also, the quasi-elastic spectra obtained by neutron scattering are unique in being able to estimate the amount of fluid participating in the relaxation process, as distinct from the amount of material trapped at the surface with a much longer timescale.

*Solvation dynamics* experiments probe the dynamics of a confined liquid as a function of pore size, temperature and surface chemistry. These experiments monitor the time-dependent emission spectra following electronic excitation of a chromophore in liquid solution. Electronic excitation of the solute molecules alters their charge distribution and thereby induces a solvent response whose predominant signature is a time-dependent Stokes shift of the mean emission energy, provided that the solvent reorganizes within the excited state lifetime of the probe. The Stokes-shift correlation function  $C(t)$  reflects the shear modulus  $G(t)$  of the solvent surrounding the probe. A laser pulse is used to populate the excited state and the subsequent emission is recorded as a function of time for various temperatures. The probe molecules can be attached to the silica surface; thus the dynamics in the immediate vicinity of the wall can be examined on the timescale from a millisecond up to few hundred seconds, and can be compared with the averaged dynamics within the pore when the probe is freely added in the fluid. This is a unique way to discriminate between interfacial and averaged dynamics. Recently, it was found that a simple non-polar liquid, 3-methylpentane, experiences an increase in its viscosity by over three orders of magnitude in the immediate vicinity of a silica interface, equivalent to a surface-induced glass transition [119]. However, only fluids confined in transparent media can be studied using the solvation dynamics technique.

*Dielectric relaxation spectroscopy.* In DRS the complex relative permittivity of the system,  $\kappa^* = \kappa' - i\kappa''$  (sometimes written as  $\varepsilon''$ ), is measured by applying an alternating electrical potential to the system, whose frequency can be varied over a wide range. Measurements of the dielectric constant  $\kappa'$  can be used to locate the phase transition of confined systems, since it exhibits large and sharp changes on freezing.  $\kappa''$  yields to the dielectric relaxation time  $\tau$ , since it is related to the energy dissipation in the system, including that due to viscous damping of the rotational molecular motion in the alternating field. For example, the order of magnitude of  $\tau$  is  $10^{-9}$  s for liquids around the melting temperature and  $10^{-3}$  s for crystalline phases. Intermediate values of  $\tau$  are characteristic of supercooled liquids,  $\tau \sim 10^{-9}$ – $10^2$  s, and hexatic phases,  $\tau \sim 10^{-5}$  s; for glasses,  $\tau$  is larger than  $10^2$  s and not measured [120–122]. However, here again the presence of the matrix may introduce distortion in the spectra obtained, and effective medium corrections specific to the porous geometry should be considered [123].

*Nonlinear dielectric effect (NDE).* Phase transitions in confined geometry can be studied using NDE experiments [124], that measure a change in the electric susceptibility induced by a strong electric field  $E$ :

$$\Delta\kappa'/E^2 = \kappa'_E - \kappa'_0/E^2, \quad (4)$$

where  $\kappa'_E$  and  $\kappa'_0$  are the electric susceptibility of the system under a strong electric field  $E$  and in its absence, respectively. The sign and magnitude of the nonlinear dielectric response for a liquid depends on the kind of inter- and intramolecular interactions and their energies [125]. The NDE versus temperature plot shows a divergence for continuous phase transitions, and its finite value is characteristic of NDE in confined systems [41, 126]. For a first-order transition, the NDE versus temperature curve breaks down at the transition temperature, as the orientational polarization ceases to exist and the value of the NDE signal in the liquid phase is close to zero. The temperature dependence of the NDE near a phase transition can be described by a scaling law, with a critical exponent that gives information about the character of the phase transition.

*Electron paramagnetic resonance (EPR)* can be of value in characterizing the nature of the liquid–wall interaction, and also in estimating the pore size of activated carbon fibres [127]. EPR is a phenomenon in which particles with a non-zero magnetic moment (paramagnetic centres, i.e. unpaired electrons) are subjected to a constant and high-frequency alternating magnetic field adjusted to cause resonance absorption of energy. The transitions between the neighbouring energy levels of a particle (in a given energy state and in a given surroundings) are the sources of EPR signals. The resonance condition is  $h\nu = g\beta H$ , where  $\nu$  is the frequency of the alternating field (most often microwave),  $g$  is the spectroscopic splitting factor,  $\beta$  the Bohr magneton and  $H$  is the intensity of the external magnetic field used to tune the system to resonance conditions. The surroundings of a paramagnetic centre can be the source of an additional local field, which permits characterization of the energy state of the particle and its environment. The spectroscopic splitting factor  $g$  is the proportionality factor between the spin energy state and the magnetic field (for a free electron  $g = 2.0023$ ). This parameter depends on the value of the magnetic field, and therefore can take different values even for a given substance. It can be treated as a parameter characterizing the close environment of the particle studied. Additional information on the interaction of the paramagnetic centres and their interactions with the environment can be inferred from the fine or hyperfine structure of the spectrum.

*Light scattering* (i.e. Raman, Brillouin and photon correlation) can provide information on the dynamics of confined fluids over a wide timescale from  $\tau \sim 10^{-9}$  s to at least 1 s [128]. In the case of confined liquid crystals, phase transitions can be monitored by measuring the frequency of some specific vibrational bands [129]. At present, this method requires transparent materials, but new nano-Raman spectroscopy will soon be available [130], and will provide vibrational bands of fluids confined in powders or dark samples.

### 2.3. Molecular simulation and theoretical methods

This section is devoted to a brief presentation of the most widely used simulation and theoretical methods to study freezing/melting in nanopores (for a detailed presentation see references [131–133]). These methods, as well as the typical time and length scales that they can access, are illustrated in figure 3(b). In practice, limitations of computer power require a compromise between the system size (length) and the time that can be covered in the simulation. Most theoretical studies are based on the density functional theory in statistical mechanics (DFT), while simulations are usually performed using the grand canonical Monte Carlo algorithm (GCMC). However, molecular dynamics (MD) and other Monte Carlo (MC) simulation methods (canonical, isobaric–isothermal or Gibbs ensemble) have also been employed to investigate freezing of confined systems. In addition to those methods, other simulation techniques (free energy calculation, reweighting histogram method, parallel tempering) can be used to improve or complete the study of freezing by numerical simulation.

**2.3.1. Molecular simulation.** Molecular dynamics simulations consists of integrating, using a time step  $\delta t$ , the classical equations of motion for all the particles  $i$  (mass  $m_i$ ) of the system:

$$m_i \frac{d^2 \mathbf{r}_i(t)}{dt^2} = \mathbf{f}_i(t) = -\frac{\partial \mathcal{U}}{\partial \mathbf{r}_i(t)}, \quad (5)$$

where  $\mathbf{r}_i(t)$  and  $\mathbf{f}_i(t)$  are, respectively, the position of particle  $i$  and the force applied on that particle at instant  $t$ .  $\mathbf{f}_i(t)$  is minus the derivative of the interaction potential  $\mathcal{U}$  with respect to  $\mathbf{r}_i$  and corresponds to the force due to all the other particles  $j \neq i$  and the pore substrate. The integration of equation (5) is made over a large number of time steps using

finite difference methods such as the Verlet algorithm [134] or the Gear predictor–corrector technique [135]. MD can be used to obtain dynamic properties of a system that cannot be measured with MC simulations. For example, transport properties and time correlation functions can be extracted and compared with experiments. In addition, static properties can also be determined from atomic configurations. The most convenient ensemble for a MD simulation is the microcanonical ensemble in which the temperature is not fixed. However, the algorithm can be modified to allow simulations at constant temperature (canonical ensemble). This is done either by rescaling the particle velocity distribution [136] or by coupling the system with a thermostat (Andersen [137] or Nosé–Hoover methods [138, 139]). The course of a MD simulation is similar to that of real experiments; starting with an initial configuration, the system evolves toward the equilibrium state. Once equilibration has been reached, dynamic and static properties are measured. MD simulations are usually performed for systems containing from  $10^2$  to  $10^5$  molecules, over  $10^5$  to  $10^7$  integration steps corresponding to ‘real’ times of the order of tens or hundreds of nanoseconds. For numerous situations, this characteristic time is larger than the relaxation time of the system (gas, liquid...). In contrast, characteristic relaxation times in the case of liquids close to the glassy transition can reach much longer times than 1 s. For these systems, the classical MD technique cannot be used but modified versions exist in which a macroscopic time step is used for the integration of equation (5).

*Grand canonical Monte Carlo (GCMC)* simulation consists of determining the properties of a system at a constant volume  $V$  in equilibrium with an infinite fictitious reservoir of particles that imposes its temperature  $T$  and its chemical potential  $\mu_i$  for each component of the system [131]. In what follows we consider the case of a pure fluid for simplicity; however, the GCMC technique is easily extended to mixtures. The freezing (melting) process is simulated by decreasing (increasing) the temperature; the final configuration of a simulation is the initial state for the next point. The GCMC technique is well adapted for the study of phase transitions since the system is allowed to exchange energy and particles with the bulk reservoir (corresponding to the usual experimental conditions). In the grand canonical ensemble,  $\mu$ ,  $V$ ,  $T$  are fixed and the grand free energy that must be minimum at equilibrium:

$$\Omega = U - TS - \mu N = F - \mu N, \quad (6)$$

where  $U$ ,  $S$  and  $F$  are respectively the internal energy, entropy and Helmholtz energy of the system. The probability of a microscopic state  $l$  in this ensemble is defined by its number of particles  $N_l$  and its energy  $\mathcal{U}_l$ :

$$P(N_l, \mathcal{U}_l) = \frac{V^{N_l}}{N_l! \Lambda^{3N_l} \Xi} \exp[-\beta(\mathcal{U}_l - \mu N_l)], \quad (7)$$

where  $\Lambda$  is the de Broglie wavelength,  $\beta = 1/kT$  and  $\Xi$  is the configurational part of the grand canonical partition function. MC algorithms consist of generating a Markov chain of states (each state depends only on the previous state of the series). In the grand canonical ensemble, the state  $l + 1$  is generated by changing the state  $l$  using one of the following moves: creation, deletion or displacement of a particle. According to the Metropolis algorithm (the most widely used MC algorithm) [140], the acceptance probability  $\rho_{\text{acc}}$  for this move (i.e. the probability to accept the state  $l + 1$  as the new state) is given by:

$$\rho_{\text{acc}} = \min\left(1, \frac{P(N_{l+1}, \mathcal{U}_{l+1})}{P(N_l, \mathcal{U}_l)}\right). \quad (8)$$

The probability acceptance given by equation (8) is a normalized distribution that verifies the condition of microscopic reversibility [132]. This probability distribution can be used since it does not require knowledge of the partition function  $\Xi$ . A GCMC simulation proceeds as follows: starting with an initial configuration, the system evolves until  $N$  and  $\mathcal{U}$  fluctuate

about their equilibrium values. Then the average values  $\langle U \rangle$  and  $\langle N \rangle$  are reset and calculated over a large number of configurations ( $\sim 10^5$ – $10^6$  MC steps per particle). Thermodynamic quantities can be estimated from  $\langle U \rangle$  and  $\langle N \rangle$ , such as the density, isosteric heat and isothermal compressibility [131]. Also, atomic configurations generated in the course of the GCMC run yield important information regarding the structure of the confined phase (e.g. density profile, pair correlation function  $g(r)$ ).

*Other Monte Carlo methods.* Other MC methods have been used to study freezing/melting in nanopores. Some authors have used the canonical  $(N, V, T)$  Monte Carlo technique [141, 142]. However, this ensemble does not correspond to the usual experimental situation in which the confined phase is in equilibrium with a bulk reservoir. The Gibbs ensemble Monte Carlo technique (GEMC) has been developed to study phase coexistence [143, 144]: the two phases are simulated in different simulation boxes. The Markov chain in a GEMC simulation is generated either by (i) displacing a particle inside a simulation cell, (ii) transferring a particle from one phase to the other or (iii) exchanging volume between the two cells. This method has been used to study both bulk [145] and confined [146–149] systems and can be extended to mixtures [150, 151]. The main limitation of this technique is that volume exchange moves require the system to be of an ideal geometry: the pore must have a simple shape (slit or cylinder) and smooth walls (no atomistic description). A third MC method that has been used to study freezing in nanopores is the isobaric–isothermal ensemble  $(N, P, T)$  Monte Carlo simulation [152]. The different MC moves to generate the Markov chain are particle displacement and volume change. As in the case of the GEMC technique, the volume change move requires the use of a structureless pore of a simple geometry. The isobaric–isothermal Monte Carlo method has been widely used since it corresponds to frequent experimental conditions. On the other hand, the difficulty with this technique is that one needs in the case of a confined system to estimate the pressure tensor, since the pressure component perpendicular to the pore surface is required [152].

*Parallel tempering.* MC moves in a simulation of freezing/melting are often characterized by very low acceptance probabilities (less than a few per cent) as it is very difficult to insert, delete or displace a particle in dense phases. This inefficiency is a serious obstacle to the investigation of freezing and melting since the system may remain ‘trapped’ in metastable states. To circumvent this poor sampling of the phase space, it is possible to combine the MC algorithm with a parallel tempering procedure [153, 154]. This technique has been developed to improve the sampling of systems with a complex energy landscape (many local energy minima) such as glass [155] or polymer [156] systems. It consists of considering several replicas of the system corresponding to different temperatures. For each replica, conventional Monte Carlo moves are attempted. In addition, swap moves between two replicas are attempted according to a probability acceptance similar to that given by equation (8) [133]: if the trial is accepted, replica temperatures are exchanged. More recently, several new strategies to overcome the limitations of configurational sampling in complex systems have been proposed. These methods include density of states Monte Carlo [157, 158] for enhanced sampling, transition path sampling [159] for studying rare events such as first-order phase transitions, and quench molecular dynamics to explore hidden phase diagrams in the metastable regions of state space [160–163].

*Free energy calculations and reweighting histogram methods.* In the study of first-order transitions (such as freezing/melting) it is of particular importance to calculate the free energy of the different phases. Indeed, the exact location of the transition is given by the equality of the free energy between the two phases. There is no direct method to determine free energies from a simulation study. Some authors have used thermodynamic integration [152], which consists of integrating for each phase the Gibbs free energy from a reference state

(ideal gas, Einstein crystal. . .), to the state of interest  $(P, T)$ . This method requires finding a reversible thermodynamic path between the two states. As will be seen later, this method cannot be applied for moderate or strong substrate/fluid potentials since it is not possible to find a reversible path from the gas phase to the liquid phase for those systems. Another method for estimating free energies is to combine the Landau–Ginzburg theory for non-homogeneous systems [164] with a histogram method [133]. In the Landau–Ginzburg method, the free energy  $\Lambda$  is written as a functional of an order parameter  $\Phi$  that depends on the position  $\mathbf{r}$ :

$$\Lambda[\Phi] = -kT \ln P[\Phi] + \text{Constant}, \quad (9)$$

where  $P[\Phi]$  is the probability density to find the system with an order parameter  $\Phi$ . The distribution  $P[\Phi]$  is estimated by collecting statistics in the form of a histogram during a MC run. The grand free energy  $\Omega$  is then calculated from the Landau free energy:

$$\exp(-\beta\Omega) = \int \exp(-\beta\Lambda[\Phi]) d\Phi. \quad (10)$$

It is difficult to obtain reliable statistics for systems with high free energy barriers because the probability of sampling the highest values  $\Lambda[\Phi]$  is very small. This leads to an important error in the estimation of the grand free energy from equation (10). To circumvent this difficulty, one can use a reweighting histogram method such as the umbrella sampling method [165]. This technique consists of increasing the sampling frequency of states with high free energy by using a biased Markov chain. It is achieved by replacing the Boltzmann factor of the system by a weighting function  $w[\Phi]$  (obviously, the probability distribution histogram must be corrected at the end of the simulation by dividing out the weighting function). The weighting function is usually defined, after a first non-biased simulation run, as the inverse of the probability histogram,  $w[\Phi] = P^{-1}[\Phi]$ . This method has been successfully applied to the study of free energy barriers in bulk crystal nucleation [166]. The Landau–Ginzburg method requires the use of an appropriate order parameter that takes different values in the different phases of the system. Suitable parameters for freezing include those that take into account the orientation of the vectors joining particles that are nearest neighbours [11, 166, 167].

### 2.3.2. Theoretical methods

*Liquid state theory.* Applications of density functional theory (DFT) in statistical mechanics have been motivated by the work of Hohenberg and Kohn for the ground state of quantum-mechanical systems [168], and its generalization to finite temperatures by Mermin [169]. For a given Hamiltonian and external potential  $V(r)$ , the free energy of the system is uniquely defined as a functional  $F[\rho(r)]$  of the inhomogeneous density  $\rho(r)$ ; moreover the free energy functional  $F[\rho(r)]$  is minimized when the density profile is the equilibrium density distribution  $\rho_{\text{eq}}(r)$ . The free energy functional is minimized with respect to the parameters characterizing  $\rho(r)$  to yield an approximation to the equilibrium density profile, which is solved in a self-consistent fashion. Correlation functions can then be obtained via functional differentiation of  $F[\rho(r)]$ . DFT calculations are readily made for systems of spherical or nearly spherical molecules; their application to more complex fluids is difficult, however. Several notable reviews on the application of DFT to freezing and melting of classical liquids are available [170–174], and here we only review the essential elements that are necessary to understand their scope.

Applications of DFT to freezing were initiated by the work of Ramakrishnan and Yussouff (RY) [175] and Haymet and Oxtoby [176]. In this perturbative approach, a functional expansion of the solid phase free energy  $F[\rho_s(r)]$  is made around a uniform liquid of density  $\rho_l$ , which is maintained at the same chemical potential  $\mu$  and temperature  $T$  as the solid. On the assumption

of rapid convergence, this expansion is truncated at second order to yield the approximate functional form for the free energy:

$$\begin{aligned} \beta F_{\text{ex}}[\rho_s] &= \beta F_{\text{ex}}[\rho_l] - c^{(1)}(\rho_l) \int d\mathbf{r} [\rho_s(r) - \rho_l] \\ &\quad - \frac{1}{2} \int \int d\mathbf{r} d\mathbf{r}' c^{(2)}(r - r'; \rho_l) [\rho_s(r) - \rho_l] [\rho_s(r') - \rho_l]. \end{aligned} \quad (11)$$

Here,  $F_{\text{ex}} = F - F_{\text{id}}$  is the excess free energy over the ideal gas term  $F_{\text{id}}$ ,  $\beta = 1/k_{\text{B}}T$ ,  $c^{(1)}$  and  $c^{(2)}$  are the first- and second-order direct correlation functions, which are equal to the first and second functional derivatives of the free energy with respect to density [170]. The neglect of higher terms in equation (11) is mainly compelled by practical limitations; the higher-order direct correlation functions of the liquid are, in general, poorly known. Thus, such a truncation is not justified *a priori*; nevertheless, it has been applied in many freezing applications involving simple fluids [175], crystal–melt interfaces [173], liquid crystals and quasi-crystals (see [171, 172] for reviews), which have been the main *ex-post facto* justification for its use.

A drawback of the above approach is that there is no small parameter guiding the expansion in equation (11) [177]. In a solid, the one-particle density  $\rho(\mathbf{r})$  is vastly inhomogeneous; thus the quantity  $\rho_s - \rho_l$  is not itself small, and the inclusion of the third-order term in the problem of hard-sphere freezing considerably worsens the results [178] obtained from the RY theory, an observation that raises questions regarding the convergence of the functional expansion of  $F[\rho]$ . This has given rise to non-perturbative density functional theories, called weighted density approximations (WDA) [177, 179–181] (see [170] for a review), which attempt to include the higher-order correlations in an approximate manner. In WDA, the free energy functional takes the form:

$$\beta F_{\text{ex}}[\rho] = \int d\mathbf{r} \rho(r) f_{\text{ex}}(\bar{\rho}(r)), \quad (12)$$

where  $f_{\text{ex}}(\bar{\rho}(r))$  is the free energy density (free energy per atom) evaluated using a smoothed density given by:

$$\bar{\rho}(r) + \int d\mathbf{r}' w_0(|r - r'|) \rho(r'). \quad (13)$$

The different versions of WDA correspond to different recipes for specifying the weighting function  $w_0$  [170, 177, 179–181]. The form of the free energy functional in equation (11) reduces to the local density approximation (LDA) when  $w_0$  is the Dirac delta function  $\delta(\mathbf{r} - \mathbf{r}')$ . LDA and associated gradient methods [170] (which normally include the gradient of the density as a first-order correction) generally fail to predict a freezing transition even when applied to simple fluids. However, WDA-based DFT methods using non-local approximations have enjoyed significant success (and improvements over the RY approach) in describing inhomogeneous situations such as fluid in pores [170, 179], freezing of hard-spheres and one-component plasmas [177, 180, 181].

Despite the widespread applications to freezing of bulk fluids [175, 181] and weakly inhomogeneous situations such as surface melting and crystal–melt interfaces [171, 173], DFT has not been the method of choice to describe freezing in highly inhomogeneous fluids such as in the presence of a strong external potential or in porous media [41]. This is mainly due to the complexity in searching for a stable state among numerous non-trivial forms for the inhomogeneous density profiles  $\rho(\mathbf{r})$  that are possible for a given form of the external potential  $V(\mathbf{r})$ . However, in the case of systems having a spherical, cylindrical or planar symmetry, the external potential  $V(r)$  depends only on the distance to the pore wall and DFT has been applied to describe freezing of inhomogeneous fluids in such pores [182–184].

*Crystal state theory.* Dislocation-mediated melting. For transitions involving breaking of the continuous translation symmetry in two dimensions (such as freezing), the Mermin–Wagner theorem states that true long-range order ceases to exist [185]. In such a situation, the mean-field approximation common to all forms of DFT is too strong ( $d = 2$  is the lower critical dimension [185]) to accurately describe even qualitatively the freezing transition. Halperin and Nelson proposed the ‘KTHNY’ (Kosterlitz–Thouless–Halperin–Nelson–Young) mechanism for melting of a crystal in two dimensions [186–188], which involves two transitions [189]. The crystal to hexatic transition occurs through the unbinding of dislocation pairs, and the hexatic to liquid transition involves the unbinding of disclination pairs. Each transition is accompanied by a non-universal peak in the specific heat above the transition temperature, associated with the entropy liberated by the unbinding of the vortex (dislocation or disclination) pairs, and by the disappearance of the stiffness coefficient associated with the presence of quasi-long-range order in the system [186–188]. The KTHNY theory employs a renormalization group treatment and predicts that the correlation function associated with the translational order parameter in the crystal decays algebraically with exponent  $\eta < 1/3$ , while long-range orientational order is maintained, and the correlation function associated with the orientational order parameter in the hexatic phase decays algebraically with exponent  $0 < \eta_6 < 1/4$ , while there is no translational order [186–188]. The KTHNY theory is an analysis of the limit of stability of a 2D solid since it neglects the existence of the liquid phase; equality of the chemical potentials of the solid and liquid is not imposed. Therefore, other 2D melting mechanisms cannot be ruled out. For example, it is possible for the dislocation unbinding transition to be pre-empted by grain-boundary-induced melting [190]. Excellent reviews are available on the subject of 2D melting [191, 192].

2.3.3. *Intermolecular potential functions.* Properties of the confined fluids in theoretical studies depend on potential functions used to model the fluid/fluid,  $u_{ff}$ , and fluid/wall,  $u_{fw}$  interactions. In order to simplify calculations, it is convenient to assume pair additive potentials for both interactions. The total intermolecular interaction,  $\mathcal{U}_i$ , for an adsorbed molecule  $i$  is then given by the sum of the pair interactions with the other adsorbed molecules  $j \neq i$  and each wall atom  $k$ :

$$\mathcal{U}_i = \sum_{j \neq i} \mathcal{U}_{ff}(ij) + \sum_k \mathcal{U}_{fw}(ik), \quad (14)$$

where  $(ij)$  and  $(ik)$  represent the position and orientation coordinates for these molecules.

The fluid/fluid interaction is usually described using potentials (often Lennard-Jones) with parameters adjusted to reproduce bulk properties of the fluid [193, 194]. Hence, these pair additive interaction potentials are ‘effective’ potentials, which account for effects of three-body forces in the homogeneous fluid. In contrast, fluids in nanopores are inhomogeneous and other three-body interactions, involving wall atoms, exist [195]. The correction due to these three-body forces can be important for microporous materials such as zeolites (up to 15% in some cases) [196]. However, three-body interactions involving wall atoms may be less important for mesopores since the confined phase is less inhomogeneous than in the case of micropores.

The fluid/wall interaction can be calculated using either atomistic or structureless walls. In the latter case, the sum of all adsorbate molecule/wall atom interactions is replaced by an integral over the solid substrate (using the atomic density of the solid). The use of structureless walls is a good approximation at high temperatures and/or when the adsorbed molecule is large compared with the wall atoms, so that the adsorbed molecule is not sensitive to the surface corrugation. For example, graphitic carbon materials are often modelled with structureless walls, since the distance between carbon atoms (1.41 Å) is small compared with the size of

many adsorbed molecules. Using a Lennard-Jones potential for the interaction between an adsorbate molecule and a carbon atom, the integration over each carbon atom in each graphene plane, followed by summation over these planes, gives the (10, 4, 3) potential proposed by Steele [197, 198]:

$$\mathcal{U}_{\text{fw}}(z) = 2\pi\rho_w\varepsilon_{\text{fw}}\sigma_{\text{fw}}^2\Delta\left[\frac{2}{5}\left(\frac{\sigma_{\text{fw}}}{z}\right)^{10} - \left(\frac{\sigma_{\text{fw}}}{z}\right)^4 - \left(\frac{\sigma_{\text{fw}}^4}{3\Delta(z+0.61\Delta)^3}\right)\right], \quad (15)$$

where  $z$  is the distance between the adsorbed molecule and the graphite surface. Here,  $\Delta$  is the separation between graphene layers (0.335 nm),  $\rho_w$  is the atomic density of carbon atoms in graphite ( $114 \text{ nm}^{-3}$ ) and  $\varepsilon_{\text{fw}}$  and  $\sigma_{\text{fw}}$  are the fluid/wall Lennard-Jones parameters, and are usually calculated by combining the wall/wall and fluid/fluid Lennard-Jones parameters using the Lorentz–Berthelot rules with the values  $\varepsilon_{\text{ww}}/k = 28 \text{ K}$  and  $\sigma_{\text{ww}} = 0.34 \text{ nm}$  [197, 198]. The first and second terms in equation (15) are respectively the repulsive and attractive parts of the interaction between the adsorbed molecule and the graphene surface, while the third term represents the summation over the other graphene layers. In the case of a slit pore having a width  $H$ , the fluid interacts with both graphite surfaces and the total fluid/wall interaction is  $\mathcal{U}_{\text{fw}}(z) + \mathcal{U}_{\text{fw}}(H - z)$ .

In addition to the integration over each graphene plane individually, it is possible to integrate the interactions over all the graphene planes in the direction perpendicular to the wall surface. The resulting fluid/wall interaction, called the 9-3 potential, is given by [198]:

$$\mathcal{U}_{\text{fw}}(z) = \frac{2}{3}\pi\rho_w\varepsilon_{\text{fw}}\sigma_{\text{fw}}^3\left[\frac{2}{15}\left(\frac{\sigma_{\text{fw}}}{z}\right)^9 - \left(\frac{\sigma_{\text{fw}}}{z}\right)^3\right]. \quad (16)$$

The 10-4-3 potential gives a better estimation of the true fluid/wall interaction than the 9-3 potential. In particular, it has been shown that the 9-3 potential underestimates the well depth of the interaction potential [198]. Similar expressions to equations (15) and (16) can be derived for pores with a cylindrical geometry [199, 200].

For low temperatures or when the adsorbed molecule is not large enough compared with the distance between wall atoms, the approximation of structureless walls becomes inappropriate, and a summation over all atom/atom interactions is required. In order to accelerate simulations, it is possible to use a 3D energy grid, which is extrapolated in the course of the simulation run to estimate the wall/fluid interaction potential [201]. Many simulation studies have used Lennard-Jones potentials to describe the interactions between the fluid molecule and each species of the solid surface. However, it has been shown that higher-order dispersion and three-body forces can be significant [196, 201–203]. Also, in the Lennard-Jones potential function, it is assumed that the polarizabilities of the interacting species are isotropic. Although this is correct for atomic species, it fails to describe interactions involving either polyatomic adsorbates [193] or surfaces with anisotropic polarizability [204] (such as graphite). Finally, induction and Coulombic interactions cannot usually be neglected in the case of polar adsorbates or wall atoms with a partial charge (zeolites, silica surfaces. . .) [195, 196, 201, 202].

Fluid/wall interaction functions can be derived from *ab initio* calculations [205], or written classically in the case of electrostatic and induction forces in terms of the fundamental properties (polarizabilities, multipole moments, etc) of the adsorbate molecules and wall atoms. However, it is often necessary to adjust these potentials in order to reproduce experimental data that depend only on the fluid/wall interaction, such as the isosteric heat of adsorption at very low coverage and the Henry’s law constant. More recently, *ab initio* approaches for describing the molecular interactions of microporous materials have been attempted using semi-empirical methods, as well as electronic density functional theory [206]. Methods for treating anisotropic polarizability using time-dependent density functional theory and an *ab initio* many-body formalism, have recently been reported [207–209].

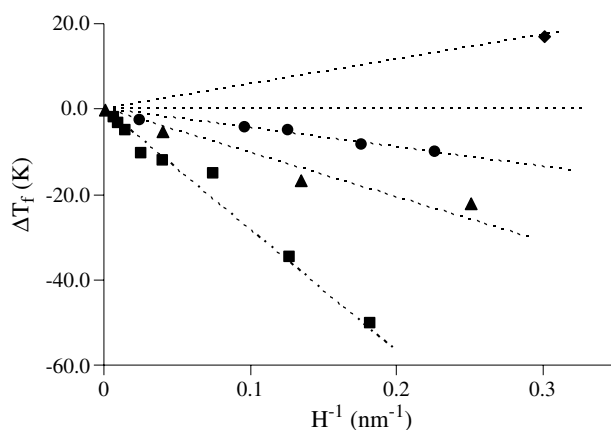


**Figure 6.** Shift in freezing temperature observed in experiments as a function of pore size: (●) O<sub>2</sub> in sol/gel glass (from Warnock *et al* [211]), (■) indium in CPG (from Unruh *et al* [216]), (◆) cyclohexane between mica plates (from Klein and Kumacheva [114]), and (▲) CCl<sub>4</sub> in controlled porous glasses (from Sliwinska-Bartkowiak *et al* [220]). The dashed lines are a guide to the eye. Adapted from Gelb *et al* [41].

### 3. Effect of confinement on structure and freezing temperature

In this section we review experimental, theoretical and molecular simulation studies on the structure and freezing temperature of confined fluids. We first consider simple systems, i.e. non-polar, near-spherical molecules confined in nanopores having a regular geometry (cylindrical or slit pore). Then we consider more complex systems, which consist of non-spherical and polar molecules confined in nanoporous materials having a more complex porous structure.

#### 3.1. Simple systems

**3.1.1. Experiment.** Most of the early experiments on freezing in confined geometry were carried out for silica nanoporous materials [41, 71, 84–87, 210–220]. Using different techniques, all these experiments showed (i) that the freezing temperature inside the pore  $T_f$  is lower than the bulk value  $T_{f,\text{bulk}}$  and (ii) that the lowering becomes greater as the pore size decreases (see figure 6). In most studies, the freezing and melting were accompanied by a significant hysteresis; the melting temperature being higher than the freezing temperature (for a review of experiments on freezing in porous media, see [42]).

Although these experiments for silica materials (which possess weakly attractive surfaces) suggested that a lowering of the freezing temperature always occurs on confinement, there is now abundant experimental and theoretical evidence that an increase in freezing temperature can occur for some systems, particularly those with solid surfaces that are strongly attractive, such as carbon and mica. The first experimental studies to suggest such an increase in  $T_f$  were carried out using the surface force apparatus (SFA) with mica surfaces [221, 222]; the pore geometry in this case is that of a single slit pore of variable width  $H$  (see section 2.2). In 1995 [114], and in more detailed experiments reported in 1998 [24, 100, 101], Klein and Kumacheva used a SFA equipped to measure both normal and shear forces (see figure 4) to study confined films of non-polar fluids of the globular molecules cyclohexane ( $\sigma \sim 0.55$  nm;  $T_{f,\text{bulk}} = 6$  °C) and octamethylcyclotetrasiloxane (OMCTS) ( $\sigma \sim 0.9$  nm;  $T_{f,\text{bulk}} = 17$  °C) at room temperature. The normal force profile,  $F(H)$ , showed strong oscillations with periodicity

of approximately one molecular diameter, indicating strong layering of the confined molecules. In the case of OMCTS, as the pore width was decreased down to a width of  $n = 7$  molecular layers ( $H = 62 \pm 2 \text{ \AA}$ ) the confined film remained fluid, that is the film did not sustain a shear stress. On a slight further reduction in  $H$  the separation of the mica surfaces decreased discontinuously to  $H = 54 \pm 2 \text{ \AA}$ , corresponding to  $n = 6$  molecular layers. At this smaller pore width the confined film strongly resisted lateral shearing, suggesting a fluid to solid transition had occurred. Measurements of the yield stress (the maximal stress that the confined phase can sustain) [24, 100, 101] showed that this was negligible (i.e. below the sensitivity of the springs used) when  $H \geq 62 \text{ \AA}$ , but was large (of the order 0.1 MPa) for  $H \leq 54 \pm 2 \text{ \AA}$ . The stress results were used to estimate an effective viscosity for the film,  $\eta_{\text{eff}}$ , and this was found to increase from less than 3 P at  $n = 7$  to more than  $4 \times 10^7$  P at  $n = 6$  and below. These results suggest a freezing transition that occurs for separations between  $n = 6$  and 7. Moreover, the transition was reversible; increasing  $H$ , starting with  $n \leq 6$ , yielded an apparent melting transition to recover the fluid-like properties observed at larger pore widths. It should be noted that the yield stress observed for the ‘solid’ film is lower than that observed for bulk crystals by several orders of magnitude, suggesting a plastic solid or a highly defective crystal.

Very similar results were obtained for cyclohexane [24, 100, 101], the transition in behaviour of the confined film occurring at a somewhat larger relative pore width (between  $n = 7$  and 8). Again, the transition is reversible and is accompanied by a sudden and large increase in the yield stress and effective viscosity, suggesting a fluid to solid transition. Similar transitions on reduction in the separation  $H$  have been observed for  $n$ -alkanes [222]. Christenson has studied capillary condensation of cyclohexane from the vapour into the pore using a simplified SFA in which the normal force  $F(H)$  is measured as a function of separation of the mica surfaces down to about  $n \sim 13$ –14 [223]. The lateral force  $F_{\text{shear}}(H)$  is not measured. As capillary condensation occurs the surfaces are pulled together by the strong capillary force until they achieve an equilibrium separation, usually of  $n \sim 1$ –3. The fact that adsorbed layers are squeezed out during condensation, and the condensate film narrows or widens in response to changes in  $H$ , is taken by Christenson as evidence that the confined film always remains fluid and does not freeze. However, the experimental observations are not in disagreement with those of Klein and Kumacheva, and in the absence of shear force measurements they do not seem sufficient to determine whether the film is fluid or solid. Moreover, Klein and Kumacheva were also able to squeeze out a layer of cyclohexane by compression in the normal direction, even after it became solid-like (in the sense of being capable of sustaining a shear stress).

Kaneko and co-workers [224–226] carried out DSC measurements on benzene and carbon tetrachloride in activated carbon fibres with pore sizes in the range 1.1–1.74 nm, and found large increases in the freezing temperature in both cases; for  $\text{CCl}_4$  the increase in  $T_f$  was 57 K, in good agreement with molecular simulation results of 59 K [225]. The increase in  $T_f$  for benzene was also about 60 K [224]. Sliwinska-Bartkowiak and co-workers, in a series of DSC and dielectric spectroscopy studies of freezing and melting in activated carbon fibres of pore width 1.4 nm, confirmed the results of Kaneko and co-workers for benzene and carbon tetrachloride [11, 124], and also observed increases in  $T_f$  of 31 K for aniline [11, 124, 227] and 42.5 K for methanol [11, 228]. This elevation of the freezing temperature in the case of graphitic walls is expected, since Castro *et al* [229] showed using neutron scattering experiments that monolayers of methane and other liquid alkanes adsorbed on a graphite layer have a solid-like structure at temperatures 10% higher than the bulk freezing point.

Sliwinska-Bartkowiak *et al* [240] have reported both experiments and simulations (involving free energy calculations) of fluids confined in cylindrical silica pores. Both the experiments and the simulations suggest that for pore diameters smaller than  $20\sigma$  the confined

phase does not crystallize into a homogeneous solid phase, while for diameters smaller than  $12\sigma$  the confined solid phase was amorphous throughout the pore. These results were found to be consistent with those obtained in a successive experimental study of nitrobenzene confined in porous glasses and MCM-41 [230]. Recently, Hung *et al* [231] have reported experimental results for nitrobenzene and  $\text{CCl}_4$  in multiwalled carbon nanotubes of internal diameter 5 nm, obtained by differential scanning calorimetry and dielectric relaxation time measurements; GCMC simulations were also carried out for  $\text{CCl}_4$ . Hung *et al* found that the frozen confined phase forms concentric layers rather than a 3D crystal, in agreement with previous results for freezing in cylindrical geometry [231]. In addition, the low-temperature phase was highly inhomogeneous, i.e. made of crystalline regions with many defects and liquids regions. Simulations show that the contact and inner layers have a freezing temperature respectively above and below the bulk freezing temperature, in agreement with the experiment.

*Thermodynamic treatment and simple models.* For sufficiently large pores, the shift in freezing temperature  $\Delta T_f$  can be related to the pore width  $H$  on the basis of the Gibbs–Thomson thermodynamic equation that is obtained either by equating the free energies of the confined liquid and solid [211] or by determining the temperature at which the chemical potential of the confined solid equals that of the bulk reservoir [232]:

$$\Delta T_f = T_{f,\text{pore}} - T_{f,\text{bulk}} = -2 \frac{(\gamma_{\text{ws}} - \gamma_{\text{wf}})\nu}{H\lambda_{f,\text{bulk}}}, \quad (17)$$

where  $\gamma_{\text{ws}}$  and  $\gamma_{\text{wf}}$  are the wall–solid and wall–fluid surface tensions,  $\nu$  is the molar volume of the liquid phase and  $\lambda_{f,\text{bulk}}$  is the bulk latent heat of melting. In equation (17), the sign of the shift in freezing temperature is given by the difference of the surface tensions  $\gamma_{\text{ws}} - \gamma_{\text{wf}}$ . Thus, equation (17) predicts that the freezing temperature will be decreased (increased) compared with the bulk value if the pore wall prefers the liquid phase to the solid phase (prefers the solid phase to the liquid phase).

In agreement with equation (17), early experiments which were performed for pores larger than 6–7 nm showed a linear relation between the in-pore freezing temperature and the inverse pore width. However, the equation fails for smaller pores. Differential scanning calorimetry and dielectric relaxation spectrometry for  $\text{CCl}_4$  confined in controlled pore glasses showed that equation (17) fails to describe the shift in freezing temperature for pores smaller than  $\sim 15\sigma$  (i.e.  $\sim 7.5$  nm) [220]. Similarly, the equation fails for  $\text{CCl}_4$  in activated carbon fibres (pore width 1.1–1.7 nm) [225]. This breakdown is due to the use in the derivation of equation (17) of macroscopic concepts, such as surface tensions (implying an interface separating two bulk-like phases), and the failure to account for the strong inhomogeneity of the confined phase. Even for cases where equation (18) is expected to apply, its use is usually limited by the unavailability of the surface tensions involved.

A qualitative understanding of the gross effects of confinement on freezing temperature can be obtained from the following reasoning, which does not rest on macroscopic arguments concerning surface tension. If we assume that the fluid molecules can be treated as Lennard–Jones particles, the bulk fluid will freeze at a temperature that is proportional to the parameter  $\varepsilon$ . Similarly, we can expect that the freezing temperature for the confined phase will be proportional to  $\varepsilon_{\text{eff}}$ , which is an effective energy parameter that accounts for both the fluid–fluid and fluid–wall interactions in some average way. For strongly attractive walls an increase in the freezing temperature with respect to the bulk is expected as  $\varepsilon_{\text{eff}}$  is larger than  $\varepsilon$ . In contrast, a decrease in the freezing temperature is expected for weakly attractive pores as  $\varepsilon_{\text{eff}}$  is smaller than  $\varepsilon$ . When  $\varepsilon_{\text{eff}} \sim \varepsilon$ , the in-pore freezing temperature should be similar to the bulk. As will be seen below, these predictions are supported by molecular simulations that Miyahara and Gubbins performed for methane in slit pores [233]. The effective well depth  $\varepsilon_{\text{eff}}$  must take

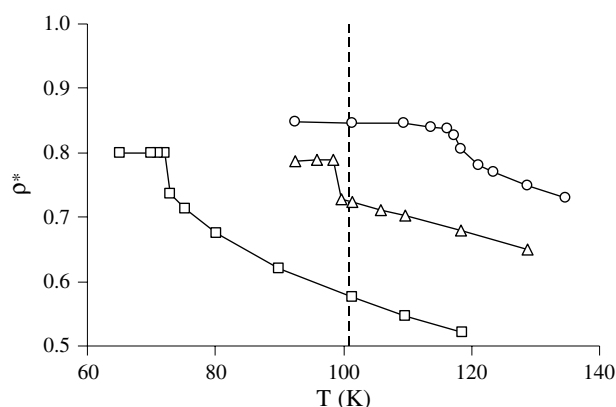


**Figure 7.** Effect of the wall/fluid interaction on the density of Lennard-Jones methane confined in a smooth slit-like pore with  $H = 7.5\sigma$  ( $\sigma$  being the diameter of methane). (O) ‘Graphite wall’ corresponds to a strongly attractive wall, and (□) ‘hard wall’ corresponds to a purely repulsive wall. (Δ) ‘Methane wall’ corresponds to a system with wall/fluid interaction similar to the fluid/fluid interaction. The straight vertical line indicates the bulk freezing temperature. Adapted from Miyahara and Gubbins [233].

into account the two well depths  $\varepsilon_{ff}$  and  $\varepsilon_{fw}$ , and also the density of the wall atoms and their arrangement in the solid wall (see equation (16), also equations (1) and (2)). Since carbon and mica surfaces are strongly attractive, we expect that a rise in freezing temperature is likely for many adsorbates that do not have strongly attractive (e.g. hydrogen bonding) fluid–fluid interactions. Such systems exhibit large  $\alpha$  values, i.e. ratio of the wall–fluid to the fluid–fluid interactions larger than 1. On the other hand, we would not expect such an increase in  $T_f$  for water in these materials, since  $\alpha$  is smaller than 1 [10, 11, 233]. Recent SFA experiments have confirmed this prediction by showing that water [234, 235] and some alcohols (octanol, undecanol) [236] remain fluid-like, even for confined film thicknesses below 1 nm.

**3.1.2. Molecular simulation.** The first detailed simulation studies of the effect of the pore size and wall/fluid interaction were performed for slit pores by Miyahara and Gubbins [233] and for cylindrical pores by Maddox and Gubbins [237]. Using GCMC simulations, Miyahara and Gubbins investigated the behaviour of Lennard-Jones methane in pores of various sizes and different wall/fluid interactions. For hard repulsive walls the freezing temperature is significantly lower than the bulk value, whereas there is a substantial increase in the freezing temperature for strongly attractive walls (graphite). In the case of neutral pores (fluid/wall interaction similar to the fluid/fluid interaction), it was found that the in-pore freezing temperature is very similar to the bulk freezing temperature [233]. These results are illustrated in figure 7 where, for different wall/fluid interactions, the overall density of methane confined in a slit-like pore is plotted as a function of temperature. In their simulation study, Miyahara and Gubbins showed that the freezing temperature for the contact layers is often different from that of the inner layers. In the case of the strongly attractive slit pore, the contact layers were found to freeze at a higher temperature than the inner layers. In contrast, the inner layers in a slit pore with purely repulsive walls were found to freeze before the contact layers. Finally, all the layers seem to freeze at the same temperature when the ratio of the wall/fluid to the fluid/fluid interaction is close to 1. Using GCMC combined with MD simulations, Maddox and Gubbins [237] reached the same qualitative conclusions for Lennard-Jones methane confined in cylindrical nanopores having various wall/fluid interactions. However, due to the geometrical

constraint of the cylinder, the freezing temperature in the cylindrical pore is lower than that in the slit pore. Thus, in a strongly attractive cylindrical pore, it was found that the inner layers could freeze below the bulk freezing temperature while the contact layers still freeze above the bulk temperature. In a GCMC study of methane confined in a cylindrical pore, Kanda *et al* [238] have clarified the effect of the pore shape on freezing/melting. These authors have shown that the freezing temperature of the confined substance is a non-monotonic function of the pore diameter, which results from the competition between a geometrical hindrance effect due to the pore shape and a compression effect due to the attraction of the pore wall [238].

In these simulations the freezing and melting processes were observed by following changes in the adsorption and structure of the confined phase as temperature was changed. Since hysteresis occurs, the freezing temperature could only be estimated approximately, and the nature of the transition (first order, continuous etc) could not be determined. A clearer picture requires a study of the free energy. In 1999, Dominguez *et al* [152] performed NPT Monte Carlo simulations of freezing of a Lennard-Jones fluid in slit pores with weakly attractive or repulsive walls. Thermodynamic integration was used to determine the free energy, and so locate the phase transition accurately. Their results were found to be consistent with previous simulation studies. These authors found strong indications that the freezing process is a first-order transition, and calculated a complete phase diagram for a weakly attractive pore (see section 5 below).

The thermodynamic integration method can only be used to determine the free energy for repulsive or weakly attractive walls, because for more strongly attractive walls a reversible thermodynamic path cannot be found due to contact layer transitions (see section 4). Radhakrishnan and Gubbins [225, 239] overcame this obstacle by using the Ginzburg–Landau approach in which the free energy is expressed as a function of an effective bond orientational order (see section 2.3). In their studies [225, 230, 239], they explored the freezing behaviour of each layer inside the pore for different slit pore widths  $H$  and ratios of the wall/fluid to the fluid/fluid interactions. Using these two parameters, they determined with the help of the corresponding states theory the global phase diagram and freezing temperature of different fluids confined in various porous media [10, 11] (see section 5). Radhakrishnan *et al* showed that for strongly attractive pores there are three phases for the confined substance (three minima in the free energy curve as a function of the order parameter): (i) the high-temperature phase corresponds to all the layers having a liquid-like structure, (ii) an intermediate-temperature phase in which the contact layers are frozen but the inner layers have a liquid-like structure, and (iii) the low-temperature phase is characterized by all the layers exhibiting a solid-like structure. All the transitions between these phases were found to be of first order. In the case of very weak attractive walls, Radhakrishnan and co-workers found that only two phases exist, the system being either completely liquid or solid. Finally, for intermediate weak attractive pores, there are also three phases as in the case of strong attractive pores but the intermediate phase (between the solid and liquid phases) is characterized by liquid-like contact layers and frozen inner layers [10, 11]. In-plane pair correlation functions corresponding to the different phases (liquid-like, solid-like, liquid contact layer and solid contact layer) are illustrated in figure 8. As will be seen in section 4, Radhakrishnan *et al* also found evidence that the contact layer undergoes a transition to a hexatic phase in the case of strong attractive pores [124, 240].

Early molecular simulations on SFA systems were aimed at understanding the large increase in viscosity that is observed in experiments. Several authors have studied in detail the layering of various systems confined between solid surfaces. These systems include spherical molecules [241, 242], polymer melts [243] and alkane chains [244–247]. Using non-equilibrium molecular dynamics (NEMD), Thompson and Robbins [248] have showed that the viscosity of confined Lennard-Jones atoms is related to the in-plane order of the system

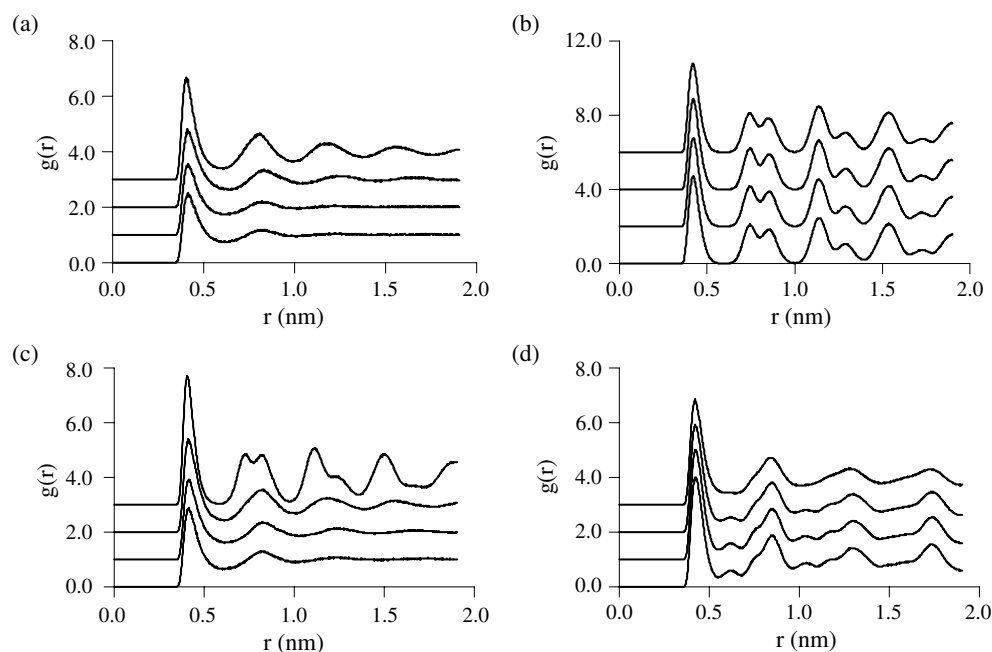


**Figure 8.** (a)–(c) The 2D, in-plane pair correlation function for each of the layers in a graphite (strongly attractive) slit pore of  $H = 7.5\sigma$  at three different temperatures: (a)  $T = 130$  K, corresponding to a liquid-like structure, (b)  $T = 101$  K, corresponding to a solid-like structure, (c)  $T = 123$  K, corresponding to a solid contact layer. Curves from top to bottom are for the contact, second, third and middle layers, respectively (from Radhakrishnan and Gubbins [239]). (d) The 2D in-plane pair correlation function for each of the layers in a weakly attractive pore of  $H = 7.5\sigma$  at  $T = 86$  K. Curves from top to bottom are for the contact, second, third and middle layers, respectively (from Radhakrishnan *et al* [10]).

rather than on the interplane order (layering). This result was demonstrated by showing that the slippage of the two confining walls decreases on increasing the value of the first peak of the in-plane structure factor  $S(Q)$  corresponding to the layer in direct contact with the pore wall. These authors [249] have also obtained results suggesting that the ‘stick–slip’ motion observed in the experiments (see for instance [250]) is due to a periodic shear melting transition followed by a recrystallization process: the sheared crystalline film melts (provided the shear is sufficiently large) enabling the wall to slip. When the stress is released and lowered below a critical value, the confined film then recrystallizes. This melting process involves a decrease of the film thickness by one monolayer [249]. These results were confirmed by Lupowski and van Swol [251] using grand canonical molecular dynamics (GCMD), that mimics in a more realistic way the change of film thickness observed in the experiments, since the number of particles is allowed to vary. Those findings are consistent with previous GCMC and MD simulations by Schoen *et al* [252] showing that sliding occurs for shear stresses above the yield stress, through the expulsion of a solid layer leading to a remaining film having liquid-like properties. Cummings and co-workers [253] observed using NEMD simulations that dodecane confined in between mica walls (modelled as strongly attractive surfaces) undergoes an abrupt liquid-like to solid-like transition when the film thickness is reduced from seven to six molecular diameters. In contrast, these authors found that dodecane films having a similar thickness remain liquid-like when confined in between weakly attractive walls [254]. In the case of

strongly adsorbing walls, the solid-like structure for confined dodecane was found to exhibit both in-plane orientational order and interplane packing correlations. The increase of viscosity determined from these simulations [255] is of the same order of magnitude as that measured by Granick and co-worker in SFA experiments [222].

Despite the apparently good qualitative agreement between the experimental SFA studies on OMCTS, cyclohexane and *n*-alkanes and the molecular simulation studies, there remains some uncertainty over the interpretation of these results. Recent simulations have suggested that the surface texture and/or elastic properties of the wall surfaces may strongly influence the confined phase. Molecular simulations performed by Persson *et al* [256] suggest that elastic deformations of the substrate are involved in the freezing process of the confined fluid. Several simulation studies have shown that both the thermodynamics [247, 256] and dynamics under shear [257] of the lubricant can be greatly affected by the surface roughness of the materials. The nature of the transition is likely to depend on the molecular geometry involved. Thompson *et al* [258, 259] have compared NEMD simulations for spherical molecules and flexible chains confined between two solid walls. For a film thickness of a few monolayers, the spherical particles were found to crystallize in agreement with previous simulation studies, while the chain molecules undergo a glass transition. MD simulations performed by Bitsanis *et al* [260–262] also suggest that flexible chains (oligomers) under confinement are trapped in a glass state; the relaxation time for the chains adsorbed on strongly attractive surfaces was found to be 1500 times larger than the bulk value. Also, several simulation studies suggest that structural interlayer and in-plane orders are less pronounced for branched alkanes than for linear alkanes [245, 246, 263, 264]. This result is due to more complex relaxation processes for the segments of branched molecules than those for linear molecules. Finally, Bock and Schoen [25, 26, 265] have pointed out that even a confined fluid-like film may exhibit a non-vanishing stress under shear that could be misleadingly interpreted as the signature of a solid structure. Using MC simulations in a grand mixed stress–strain ensemble (load, stress, temperature and chemical potential constant) and lattice-gas calculations, these authors have shown that a Lennard-Jones fluid confined between walls with alternating strips of weakly adsorbing or strongly adsorbing solids is able to sustain a shear stress [26, 265]. In this study, it is shown that the liquid bridges formed between strongly attractive strips are able to sustain a strain that is only one order of magnitude lower than that obtained for confined solid [266]. Further study is needed to fully clarify these issues and determine the nature of the confined phase (solid-like, glass or liquid-like).

**3.1.3. Solid/solid transitions.** While experimental studies are very limited, there have been several molecular simulation investigations of solid/solid transitions in confinement that occur due to a change in temperature or in pore width. For Lennard-Jones fluids confined in slit graphitic pores Ghatak and Ayappa [267–269] have shown that, for the same number of layers inside the pore, the structure of the solid phase undergoes a transition from a square lattice to a triangular lattice symmetry as the pore width increases, and this has been confirmed by studies carried out by Vishnyakov and Neimark [270]. Similar changes in the symmetry of the crystal phase are observed when the number of adsorbed layers changes from  $n$  to  $n + 1$ . Bock *et al* [271] used density functional theory to study Lennard-Jones adsorbates confined within structureless slit pores. They determined the solid–solid phase diagram as a function of pore width, and observed zig-zag buckling and a stable asymmetric buckled phase.

Most of these simulations were for smooth (structureless) walls. This may be a good approximation provided that the temperature is not too low, and the size of the fluid molecule is much larger than the spacing between the wall atoms (0.147 nm for graphite). For more general cases surface corrugation must be included, and many studies (e.g. [272–278]) of

monolayers adsorbed on a single wall have been reported showing that surface corrugation can lead to commensurate/incommensurate and other phase transitions (for a review see [279]). In an early study of phase behaviour in an atomistic slit pore, Schoen and co-workers showed that the nature of the confined phase (solid or liquid) depends also on whether parallel walls were in or out of registry [280, 281]. As previously mentioned, simulation studies and SFA experiments obtained similar results by showing that the solid phase can undergo a melting transition induced by the shear stress [249–251]. In their study, Curry *et al* [281] simulated the freezing of simple fluids confined between atomistic walls with rectangular grooves carved out of one of the walls. The phase behaviour of the fluid was found to depend on the pore width, groove width and groove depth.

Sokolowski and co-workers [282, 283], using canonical and grand canonical MC simulations, have studied the behaviour of a Lennard-Jones fluid confined in slit-like pores having (100) fcc walls, with various wall/fluid interactions [283] and widths from  $3.0$  to  $6.0\sigma$  that can accommodate from two to four layers of the confined phase. For each number of layers, there is a limited range of pore widths for which the freezing transition leads to a commensurate solid phase, i.e. crystal layers having a square symmetry compatible with the lattice of the pore wall. It was shown that the melting transition between this commensurate phase and the non-commensurate hexagonal phase is accompanied by a decrease of one in the number of layers confined in the pore [282]. The hexagonally incommensurate ordered phase is favoured when the wall/fluid interaction becomes weaker than the fluid/fluid interaction. This result is due to the higher density of the hexagonal structure, which increases the fluid/fluid interactions compared with the square structure. On the other hand, systems with strongly adsorbing walls and high-density adsorbates exhibit a ‘domain wall’ structure [283]. This 2D phase is composed of commensurate and incommensurate domains that are separated by crossing walls [277]. Using MD simulations, Dominguez *et al* [284] have also studied solid phases formed by Lennard-Jones particles confined in a slit pore made of (100) fcc walls. They have shown that strong fluid/wall interactions lead to the formation of a (100) solid phase having a layered structure, while compact (111) solid structures are obtained in the case of weak interactions. Camara and Bresme [285] have used MD to study the crystallization of Lennard-Jones argon near the triple point confined in slit-like pores with crystalline fcc argon walls (100). They estimated the crystallization force (the force that a growing solid exerts on its environment) as a function of the pore width. They found that the freezing transition is characterized by an important peak in the disjoining pressure versus pore width curve; the corresponding force of crystallization was estimated to be 100 MPa. In addition, for systems with similar fluid/fluid and fluid/wall interactions, the confined solid phase can be stabilized at temperatures up to 45% above the bulk freezing temperatures, if the lattice spacing of the wall substrate allows the formation of a commensurate phase [285]. Another property of the pore wall that can play an important role in freezing phenomena is the presence of surface impurities. Vishnyakov *et al* [286] have studied the freezing of methane in graphitic slit pores of varying widths and different densities of surface chemical groups such as  $\text{NH}_2$  and  $\text{CH}_3\text{OH}$ . They showed that the presence of active sites on the pore surface leads to a lowering of the freezing temperature (when compared with the case of an ideal graphite pore) and can change its dependence on the pore width.

### 3.2. Complex systems

**3.2.1. Freezing temperature of the confined phase.** In complex systems the pore structure is no longer of simple geometry, and the intermolecular forces may be significantly non-spherical. The interpretation of experimental results is often difficult for such cases, due to

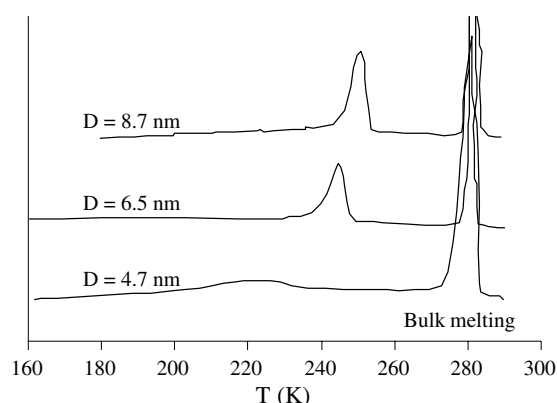


**Figure 9.** DSC scans of benzene confined in SBA-15 on heating at  $10 \text{ K min}^{-1}$ , with a quantity which melts at the bulk melting point (from Dosseh *et al* [72]).

broad transitions and uncertainty in distinguishing between different solid phases, very viscous liquids and glasses. As Bragg peaks are characteristic of crystal phases, neutron or x-ray diffraction experiments are convenient for the study of freezing and melting experiments. By following the evolution of the peaks, phase change temperatures and even phase compositions can be monitored. However, the Bragg peaks are broadened by excluded volume effects and a lack of isotropic periodicity (see figure 9). The depression and broadening of the freezing transition as measured by DSC experiments are illustrated for the case of benzene confined in SBA-15 in figure 9, where the two peaks are attributed to the melting of the confined and bulk liquid, respectively. The breadth of the transition is found to increase as the pore size decreases. The results suggest that the broadening is due to a progressive layer-by-layer melting of the confined phase [73, 287].

As for simple systems, the relative strength of the fluid/wall and fluid/fluid attractive interactions plays an important role. As pointed out in the introduction, the concept of strongly or weakly attractive walls depends on the adsorbate/adsorbent system that is considered. Other factors, such as the softness of the wall, may also be important for describing freezing of complex systems. For strongly attractive walls, such as carbons and mica, an increase in freezing temperature over the bulk value may be observed, particularly for adsorbates with weak or moderately attractive fluid/fluid interactions. In such cases, the crystal is expected to nucleate at the pore surface, and then grow within the pore. On the other hand, the freezing temperature is reduced from the bulk value for fluids confined in weakly attractive materials. In such cases, the crystal nucleates at the centre of the pore while the layers in contact with the pore surface remain liquid-like. Some confined liquids may have contact layers that never crystallize (see section 4). The packing constraints of the crystalline lattice cannot be satisfied for molecules in the vicinity of the surface because of its local topology (roughness and curvature), its softness or its chemical nature. As a result, the molecules at the surface do not crystallize and instead a less ordered or amorphous region (viscous liquid or glass) occurs there. Such a decrease of the melting point has been observed for cyclohexane and benzene confined in weakly adsorbing silica porous materials [72–74, 106, 299]. While these two adsorbate molecules are of similar size, the melting point depression was found to be larger for cyclohexane than for benzene, suggesting that the interaction of benzene with the wall (between benzene's  $\pi$  electrons and the hydroxyl groups on the walls) was stronger than that of cyclohexane. The decrease of the melting temperature becomes greater as the pore

size decreases, in qualitative agreement with the Gibbs–Thomson equation (see section 3.1.1). However, the  $1/r$  relation assumed by this equation often fails for small pores, for reasons discussed in section 3.1.1, and because the reduced density of the confined fluid differs from the bulk value [77, 118, 288].

The special case of confined fluids with hydrogen bonds, such as methanol [106, 288] or water [110, 289, 290], is of particular interest. Water has a strong fluid/fluid interaction due to hydrogen bonding so that one expects water confined in weakly attractive pores to experience a larger decrease in its freezing temperature than that for hydrocarbons. However, experimental evidence has been reported that the freezing point depression is much larger for hydrocarbons molecules, such as cyclohexane or benzene, than for water in some silicas. This result suggests that there is significant hydrogen bonding between the water molecules and the hydroxyl groups at the silica surface, and this compensates for the strong water/water interaction. Other experimental studies have shown the significant effect of the wall/fluid interaction on freezing. For instance, it has been shown that the decrease of the melting temperature is smaller when the walls of the porous material are treated (silanized or dehydroxylated) in order to increase the wettability of organic compounds, i.e. reducing the wall/fluid interaction [72–74, 106, 291]. The validity of the Gibbs–Thomson equation was found to depend on the interaction between the pore surface and the confined liquid, even for large pore diameters. For instance, the freezing behaviour of water confined in SBA-15 pores can be reasonably described using the Gibbs–Thomson equation, while it fails to describe experimental results for cyclohexane and benzene.

*3.2.2. Nature of the wall/fluid interaction.* One of the first experimental investigations of the nature of the wall/fluid interaction was undertaken by Sliwinska-Bartkowiak and co-workers [292, 293]. Using EPR measurements (see section 2.2), the authors studied whether the interactions between the confined liquid and the porous material involved chemical bonding or only van der Waals forces. The experiments were performed for  $\text{CCl}_4$ ,  $\text{C}_6\text{H}_6$  and  $\text{C}_6\text{H}_5\text{NO}_2$  confined in activated carbon fibres (ACF). In each case, a broader component in the EPR signal is observed when guest molecules are adsorbed in ACF voids. On the other hand, no direct EPR signal from the guest molecules was observed, so that the broadened, modified EPR signal is due to the adsorbate–graphite interactions only. This result shows that there is no charge transfer between the ACF and the confined molecules. Moreover, no hyperfine splitting arising from the interaction with nuclear spins of H or N was observed [292]. The strongest modification of the EPR spectrum was observed for ACF filled with nitrobenzene  $\text{C}_6\text{H}_5\text{NO}_2$  (see figure 10). The EPR signal consists of three lines: line (1) is characteristic of pristine ACF; its  $g$  value equals that of graphite ( $g = 2.0031$ ) [294]. Both the line width and the  $g$  factor are temperature independent. The broader components of the EPR signal, lines (2) and (3), are also related to the graphite structure of ACF. The temperature-independent line (2) originates from graphite particles (host) surrounded by guest molecules captured in the nanopores. The broadening of the line (2) is caused by the shorter relaxation time of the denser system (ACF/confined liquids) compared with that of empty ACF. The line width and  $g$  factor of the component (3) of the EPR spectrum strongly depend on the temperature. Such a behaviour can be explained as a surface effect in ACF; stronger instabilities of paramagnetic centres at the surface of the ACF or in its larger pores appear as a temperature effect. When the temperature is lowered below 20 K, both the line width and  $g$  factor reach values characteristic of graphite nanoparticles surrounded by confined molecules. No Dysonian shape of the EPR line is observed for each component, showing that the ACF crystallite typical size is lower than the penetration depth of the microwave field in graphite,  $3.2 \mu\text{m}$  [291]. As expected for pristine ACF, the three lines obey the Curie law that is characteristic of Langevin paramagnetism. The

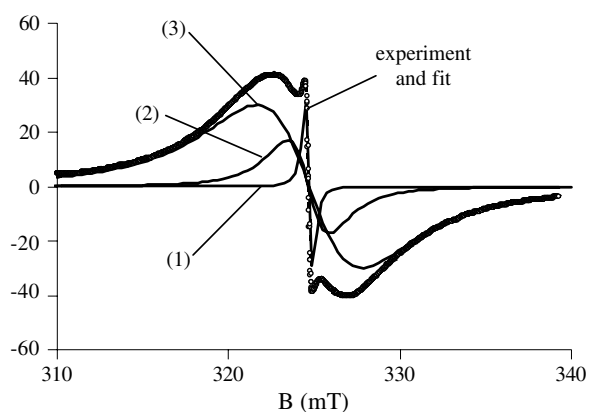


**Figure 10.** EPR spectrum for ACF filled with nitrobenzene. Experimental and fitted points are the sum of lines: (1) EPR signal from empty ACF, (2) EPR signal originating from graphite particles (host) surrounded by guest molecules captured in the nanopores (temperature independent), and (3) EPR signal strongly dependent on the temperature. Such behaviour can be explained as a surface effect in ACF (from Kempinski *et al* [293]).

lack of hyperfine splitting and the observation of the Curie law for the three EPR components confirm that the paramagnetic centres are localized within the ACF crystallites. Using the theory of EPR for small particles [295, 296], the average pore size of the ACF was estimated to be 1.34 nm.

**3.2.3. Partial or complete crystallization.** Numerous NMR and DSC experiments on materials with weakly attractive or repulsive pore surfaces show partial crystallization. This can be easily observed in NMR experiments since the line widths for liquid and solid phases usually differ by at least one order of magnitude. The differences in the NMR line width are due to a difference in dynamical properties between the liquid layer at the surface of the pore and the crystal in the centre of the pore. Pulse gradient NMR (PG-NMR) experiments on organic compounds show that the diffusion coefficient of the liquid-like molecules is at least one order of magnitude larger than the diffusion coefficient of the crystal in the centre of the pore [297]. The NMR signals show that the number of liquid-like molecules within the pore increases as the temperature increases up to the melting point (see figure 11). This property of melting in porous media is analogous to the pre-melting effects for bulk systems [298], but extends over a wider temperature range.

Only partial crystallization occurs for organic molecules, such as cyclohexane or benzene, confined in cylindrical silica pores having a pore diameter smaller than 10 or  $20\sigma$  [72, 73, 106, 299]. From recent  $^2\text{H}$  solid state spectra of benzene- $\text{D}_6$  confined in SBA-15, Findenegg and co-workers [74] have found at all temperatures below the freezing point two states with  $T$ -dependent intensity ratios, and they have estimated a thickness of four molecular layers for a contact surface region at the liquid to solid transition. Below the freezing temperature, the confined phase is a mixture of defective crystal and amorphous regions. Complete crystallization should occur in the case of larger pores. For instance, Booth and Strange [71] have shown that crystallization of cyclohexane confined in CPG is complete below 250 K in pores of 20 nm, and below 268 K in pores of a size 50 nm. In the case of  $\text{CCl}_4$  confined in CPG, a similar pore size dependence on the degree of crystallization has been predicted by Monte Carlo simulations, and confirmed by DSC experiment [240], as discussed

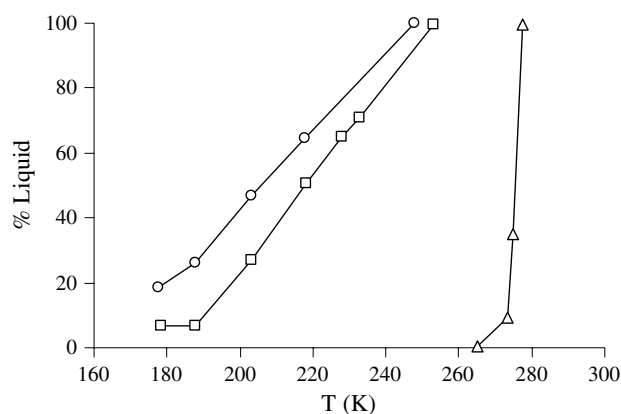


**Figure 11.** On heating as measured by NMR, the number of liquid-like molecules within SBA-15 pores increases with temperature up to the melting points: (O)  $D = 6.5$  nm, (□)  $D = 4.7$  nm, (△) bulk. The same qualitative behaviour was observed in bulk samples in a much narrower temperature range.

in section 3.1.1. Crystallization of more complex molecules, such as polar or non-spherical ones, is more complicated. Aromatic liquids, such as toluene or *o*-terphenyl, do not crystallize in silica SBA-15 pores having a diameter smaller than  $20\sigma$  [77, 118, 128, 300].

**3.2.4. Water in pores.** There have been many experimental reports on the structure of water confined in porous media investigated through NMR [84–86, 217, 301], x-ray/neutron diffraction [219, 302–305], SFA [234, 235], DSC [228, 287, 306–308] and DRS [228] techniques. The great majority of these studies are for porous silica materials, including sol-gel disordered silica, MCM-41 and SBA-15. The freezing of water in the inner region of the pores was found to occur at temperatures below the bulk freezing point, the temperature depending on the pore size. Several authors [303, 306, 295, 296, 301] have shown, using DSC or NMR experiments, that the decrease in the freezing temperature for water in the inner region of the pore is consistent with the Gibbs-Thompson equation (17), provided the pore radius  $R$  is replaced by  $R - t$ , where  $t$  is the thickness of the bound water. For water confined in activated carbon fibres having a pore width of 1.8 nm, Sliwiska-Bartkowiak *et al* [228] also observed a depression of the freezing point,  $T_{f,pore}/T_{f,bulk} \sim 0.87$ , in agreement with GCMC simulations. Such a decrease in freezing temperature is expected for water, since  $\alpha$  (see equations (1) and (2)) for water in both silicas and carbons is small [10, 11], due to hydrogen bonding between the water molecules.

Many authors (e.g. [217]) report the presence of a layer of ‘bound water’ near the pore walls that retains a liquid-like structure at temperatures at which the inner confined fluid freezes. Such layers have been observed for water in sol-gel disordered porous silica [295, 296] and in cylindrical silica pores MCM-41 and SBA-15 [219, 303, 304, 306]. Morishige and co-workers [219, 303, 304], in XRD measurements for water confined in MCM-41 and SBA-15 silica pores, found that the freezing of water close to the pore wall was a continuous process that occurs over a range of temperatures, the temperature being independent of the pore size; i.e. a surface rather than a confinement effect. Sklari *et al* [301] have shown that the freezing temperature of the contact layers depends on the density of OH groups at the surface of MCM-41 pores. Overloop and Van Gerven [217], using NMR, found that the translation and rotation correlation times in the bound water phase fell in a range between that for the liquid and

the crystal phases. Using GCMC simulations for a  $7.5\sigma$  slit pore having weakly attractive walls, and  $\alpha$  values similar to those for the confined water systems studied experimentally, Radhakrishnan *et al* [11] have also observed the existence of a new surface-driven phase ‘contact liquid’, with a solid inner region and boundary liquid layers (see sections 4 and 5, particularly figure 15(a)).

Based on NMR [217], XRD [219, 303, 304] and DSC [306] studies, several authors have concluded that the water in the interior of silica pores (sol–gel silicas, MCM-41 and SBA-15) crystallizes into the  $I_c$  cubic phase. However, Morishige and Kawano [303], in studies of water in Vycor glass, and Dore and co-workers [302, 305] in the case of sol–gel porous silica and MCM-41, found evidence for both the cubic  $I_c$  and hexagonal  $I_h$  phases.

Few simulation studies of freezing of confined water have been reported, and as far as we are aware there are no detailed studies that include free energy calculations. Koga *et al* [309, 310] studied the freezing of water in hydrophobic nanopores by molecular dynamics simulation, using the TIP4P model for water and a weakly interacting, structureless wall. They observed a monolayer ice phase [310] and also a bilayer ice formation [309, 310] by controlling the pressure normal to the pore walls. The bilayer ice crystal is characterized by a hydrogen bonding network of water molecules, each layer forming a distorted hexagonal lattice. In a subsequent MD study, Koga *et al* [311] studied the freezing of water confined in carbon nanotubes having diameters from 1.1 to 1.4 nm and obtained new ice phases that are not observed for bulk water. The authors observed a first-order transition between hexagonal ice  $I_h$  and heptagonal ice and a continuous phase transition between square ice and pentagonal ice.

#### 4. New surface-driven and confinement-driven phases

##### 4.1. Contact layer phases

As mentioned in section 3.2, many authors (e.g. [71, 217, 219, 240, 303, 312, 313]) have reported experimental evidence that the adsorbed molecular layers adjacent to the pore wall have a different structure from that of the inner adsorbed layers. These experimental works were for silica materials, and suggest that the adsorbed layer near the pore surface is liquid-like, while the internal adsorbed layers are either amorphous solid or crystalline. For example, Booth and Strange [71] examined the melting of cyclohexane in porous silica using the NMR technique. The melting temperature was below the bulk melting point, and in the confined solid phase there were two distinct components of the transverse relaxation time. The short component (15–30  $\mu$ s, comparable to the crystal phase in the bulk) was attributed to the crystal phase in the interior of the pore, and the long component was attributed to a liquid-like contact layer (the layer adjacent to the pore walls). Further lowering of the temperature led to the freezing of the surface (contact) layer as well.

Using differential scanning calorimetry and dielectric relaxation spectroscopy, Sliwinska-Bartkowiak and co-workers [240] studied the melting and freezing transition for nitrobenzene confined in controlled pore glass and MCM-41 of different pore sizes. Depending on the temperature, they observed relaxation times characteristic of liquid and solid phases. In addition, a third relaxation component was observed that supported the existence of a contact layer with dynamic properties that were liquid-like but different from that of the liquid-like inner layers; in particular, the rotational relaxation times of molecules in the contact layer were about four orders of magnitude slower than molecules in the liquid-like region [240]. Slower dynamics of molecules in the contact layer were also reported by Takahara *et al* [312], in a neutron scattering study of liquid-like water confined in MCM-41.

Contact layer behaviour that is different from that of the inner layers has also been observed in molecular simulations. Miyahara and Gubbins [233] found that for methane

adsorbed in strongly attractive graphite slit pores accommodating more than three molecular layers, the contact layer formed a 2D crystal at a higher temperature than the inner layers. Later calculations have been reported [10, 11, 124, 230, 239] for slit pores in which the Landau–Ginzburg approach was used to determine free energies, and hence the stability of the various phases and the order of transitions among them. Some of this work was discussed in section 3.1.2 (see also figure 8). For purely repulsive walls (e.g. hard walls,  $\alpha = 0$ ) only two phases are observed, liquid-like and crystalline [10]. For weakly attractive walls ( $\alpha < \sim 0.48$  in these calculations) a local minimum in the free energy corresponding to a contact layer phase in which the contact layer was fluid while the inner layers were crystalline was observed for the higher  $\alpha$  values, but this phase remained metastable with respect to one of the other phases (liquid-like or crystalline). At somewhat higher  $\alpha$  values (attractive wall of intermediate strength,  $0.48 < \alpha < \sim 1$ ), as the temperature is raised the confined phase passes from a crystalline structure to a phase in which the contact layer remains fluid while the inner layers are crystalline; at some higher temperature the inner layers melt and the confined phase becomes entirely fluid. Systems involving silica pores generally fall in this class. For strongly attractive walls ( $\alpha > 1$ ), e.g. systems in which the fluid–fluid interaction is relatively weak compared with the fluid–wall interaction, a similar intermediate phase is observed in which the contact layer is crystalline although the inner layer is liquid-like; systems involving a non-polar fluid adsorbed in carbons usually fall in this class. Radhakrishnan and co-workers [11] have termed these intermediate phases, in which the contact layer has a different structure from the inner layers, ‘contact layer phases’, distinguishing between ‘contact liquid’, in which the contact layer is liquid-like while inner layers are crystalline, and ‘contact crystal’ phases in which the contact layer is crystalline while the inner layers are liquid. In the simulations the transitions among these three phases are weakly first order. The freezing of the contact layers at an elevated temperature compared with that of the inner layers causes a significant deviation from the linear behaviour predicted by the Gibbs–Thomson equation (17) in the case of smaller pores ( $H < 5\sigma_{\text{ff}}$ ) [225].

#### 4.2. Hexatic phase and two-dimensional melting

According to the Kosterlitz–Thouless–Halperin–Nelson–Young (KTHNY) mechanism, the melting of a crystal in two dimensions [186] involves two transitions of the Kosterlitz–Thouless (KT) kind [189]. The first, the crystal to hexatic transition, occurs through the unbinding of dislocation pairs of the solid phase, and the second, hexatic to liquid, transition involves the unbinding of disclination pairs. In principle, it is possible for the dislocation unbinding transition to be pre-empted by grain-boundary-induced melting. For instance, Chui [189] has developed a model in which the melting cross-over from grain-boundary-induced melting to two-stage KTHNY melting occurs for defect core energy above  $2.84 k_{\text{B}} T_0$  (where  $T_0$  is the temperature at which the dislocations unbind) [191].

Experimental and computer simulation studies on the subject of 2D melting (see below for a summary) often have the underlying objective of establishing whether or not the pathway of melting conforms to KTHNY behaviour: (1) Does melting occur in two stages mediated by a hexatic phase? (2) Do the order parameter correlation functions associated with the crystal and hexatic phases have the appropriate scaling behaviour? (3) Are the observed phase transitions first order or second order in the thermodynamic limit? Excellent reviews are available on the subject of 2D melting and discussion of its vast literature (see for instance [191]).

In experimental systems, the 2D limit is achieved either by means of confinement (porous material, SFA) or by deposition of a thin film on a planar substrate. The presence of the external material often plays a significant role in determining the phase behaviour of the 2D

system. The hexatic phase was first directly observed in a free-standing liquid crystalline film, using electron diffraction [314–320]. There have also been numerous experimental studies of the melting of adsorbed films on planar substrates, particularly graphite [229, 321–329], but conclusive evidence for an intrinsic hexatic phase in these adsorbed systems only exists for xenon adsorbed on graphite [321, 322]. Molecular simulations for both free-standing 2D films and adsorbed films on planar substrates have been reported, but in most cases the small system sizes used are likely to lead to inconclusive results. An exception is a study by Bagchi *et al* ([330]; see also [331]), who studied a 2D film of 64 000 atoms with repulsive interactions. A systematic scaling analysis showed that the equilibrium properties are indeed consistent with the KTHNY theory of melting.

Two-step melting consistent with the KTHNY behaviour seems to be more easily observed in confined systems. Early work on confined colloidal suspensions by Murray and Van Winkle [332] found such behaviour in a system of submicrometre monodisperse charged polystyrene spheres suspended in water and confined between glass plates. The defect structures were analysed by photographic imaging of the spheres and constructing Voronoi polygons [191]. The defect core energy near the melting transition was estimated to be  $E_c \approx 6 k_B T$ , which lies in the KTHNY regime according to the work by Chui [190]. Similar experiments were performed by Rice and co-workers using different screened (effective) potentials with which the colloidal spheres interact [333, 334]. A system of sterically stabilized uncharged polymethylmethacrylate (PMMA) particles undergoes first-order crystal–hexatic and hexatic–liquid transitions with order parameter correlations differing from KTHNY predictions [333]; on the other hand a system of uncharged sterically stabilized silica particles (effectively interacting as hard spheres) undergoes a one-step first-order melting transition from crystal to liquid [334]. The strong dependence of the melting scenario on the interparticle interaction found in the experiments [333, 334] is consistent with a computer simulation study by Bladon and Frenkel [335] that reported a strong dependence (and qualitatively different phase diagrams) of melting behaviour on the parameters of the intermolecular interaction of a two-dimensional square-well fluid. A consensus regarding the differing scenarios has not yet emerged due to: (a) the experimental studies on colloidal systems are faced with the question of attainment of thermodynamic equilibrium [333, 334] while the simulation results are for a small system size [335], and therefore subject to finite-size effects; (b) the calculated value for the defect core energy  $E_c$  for hard discs lies in the KTHNY regime [331]; (c) the qualitative behaviour of these studies in the limit of a hard sphere potential differs from that of a recent simulation study by Jaster [331] on a large 2D system of hard discs. The latter study involves a system size scaling analysis that ruled out a first-order transition with a small correlation length, and rather supported a two-step melting behaviour consistent with KTHNY scaling. More recently, Zahn *et al* [336] studied two-dimensional melting of colloidal spherical particles interacting with repulsive (effectively dipolar) potential and reported a two-stage melting scenario with scaling behaviour conforming to KTHNY theory. The researchers ensured the attainment of thermodynamic equilibrium by checking for reproducibility of the scaling behaviour [336].

There have been a limited number of studies of quasi-two-dimensional melting for simple fluids confined within slit-shaped pores. Radhakrishnan *et al* [10, 11, 124, 228, 239, 337] reported grand canonical Monte Carlo simulation and experimental results for simple fluids adsorbed in slit carbon pores, a model of ACF. Such an adsorbed phase consists of one or two molecular layers. In the simulation studies, a systematic size scaling analysis was performed, and the Ginzburg–Landau parameter was used to monitor the self-consistency of the finite size results [11, 124, 337]. The scaling of the order-parameter correlation functions in the simulations [11, 337] was consistent with the KTHNY behaviour, implying that it is the vortex

excitations that govern the equilibrium behaviour in the quasi-2D systems and that the melting transition is defect-mediated. The authors also presented a scaling analysis and free energy calculation for a system size of 180 molecular diameters [124, 337]. Based on the Lee–Kosterlitz scaling [338] of the free energy surface, they established the nature (first-order versus continuous) of the transitions: for the quasi-2D monolayer, the Kosterlitz–Thouless transitions are continuous, while for quasi-2D bilayers, the Kosterlitz–Thouless transitions become first order (the order of the phase transition was determined by examining the dependence of the free energy barrier separating two phases as a function of system size) [124]. The free energy barrier separating hexatic and crystal phases was found to be independent of system size for a single confined layer and a linear function of system size when two confined layers were present. On the other hand, the Lee–Kosterlitz scaling implies that the transition is continuous when the free energy barrier is size independent (one-layer case) and first order involving nucleation when there is a linear dependence (two-layer case). Based on heuristic arguments gleaned from the analysis of the 2D  $x$ – $y$  model, the authors [124, 337] ascribed this deviation from 2D behaviour to the interactions between the defect configurations in different layers.

While the simulations face the difficulty of finite-size effects and computational intensity, experimental studies of 2D melting in pores suffer from the difficulties of small samples of the confined phase (making scattering studies difficult) and poorly characterized porous materials. Sliwiska-Bartkowiak and co-workers have reported experimental measurements based on DSC, DRS and NDE for  $\text{CCl}_4$  and aniline adsorbed in ACF accommodating two confined layers,  $H = 1.4$  nm [228, 124, 337]. Starting from a low temperature, where the confined phase was a solid, the melting showed two transitions whose temperatures were in quite good agreement with those from the simulations for both  $\text{CCl}_4$  and aniline. In the case of aniline, the transition temperatures were also confirmed by DRS experiments. The authors reported measurements of the nonlinear dielectric response, which diverged at each of the two transitions. The temperature dependence of the NDE signal was analysed on the basis of a phenomenological scaling law proposed by De Gennes and Prost [339], which has its underpinnings in the Ornstein–Zernike formalism [340] of the two-point correlation function of the order parameter. The temperature scaling of the NDE signal was found to be consistent with the KTHNY theory for liquid–hexatic and hexatic–crystal transitions, and the authors concluded that the transitions observed in the experiments were remnants of KTHNY melting. This interpretation, if correct, shows that the hexatic phase is stable over a wide temperature range, 55 K for  $\text{CCl}_4$  and 26 K for aniline. This large range of state conditions over which the hexatic phase is stable, also observed in the simulations, may be unique to confined fluids in porous media.

#### 4.3. Glass transition in nanoporous materials

A liquid becomes a glass when, following a small perturbation, the relaxation time of any measurable property becomes longer than the experimental time of observation. The liquid to glass transition point,  $T_g$ , is defined in an operational way as the temperature at which a relaxation time of  $10^2$ – $10^3$  s or a viscosity of  $10^{11}$ – $10^{13}$  P is attained. The glass transition is observed in a wide variety of materials, such as network glasses ( $\text{SiO}_2$ ,  $\text{GeO}_2$ ), linear or branched polymers, hydrogen-bonded liquids, ionic salts, electrolytic solutions and even for metals or simple van der Waals systems. Typical transition temperatures  $T_g$  range from about 1600 K for  $\text{SiO}_2$  to about 70 K for low-molecular-weight hydrocarbons. The mechanism of glass formation is usually viewed in terms of physical vitrification that may happen when a liquid, being in a metastable state, is cooled below its melting temperature or compressed above its melting pressure. On the other hand, glasses may also be formed by chemical vitrification, which involves progressive polymerization of the molecules via the formation of irreversible

chemical bonds; examples of such glasses are materials used in engineering plastics, natural and synthetic resins. Despite the different molecular processes involved in chemical and physical vitrification, the slowing down of the dynamical and thermodynamic properties of the resulting glasses are similar.

Viscosity and structural ( $\alpha$ ) relaxation times in glass-forming liquids can vary over 14 orders of magnitude when changing the temperature by a mere factor of two at atmospheric pressure, a feature that calls compellingly for a logarithmic representation [22, 341–346]. Such dramatic variations of the dynamical properties are usually represented in Arrhenius plots of  $\log(\eta$  or  $\tau)$  versus  $1/T$ , and conventionally interpreted in terms of thermally activated dynamics, i.e. in terms of a collective passage over potential energy barriers in a multidimensional configuration space; in such a picture, molecular motions of deeply supercooled molecular glass-formers at atmospheric pressure, as well as the dynamics of network-forming systems where bond breaking energies are quite sizeable, are impeded by insufficient thermal energy to hop across barriers that are large compared with  $kT$ .

The dramatic increase of the relaxation times and the manifestation of heterogeneous dynamics close to the calorimetric glass transition temperature  $T_g$  are naturally interpreted as a result of collective behaviour of the molecules. The possible existence of a mesoscopic length scale in deeply supercooled liquids has been postulated for many years, and the notions of cooperativity, correlation length and heterogeneous domains have been introduced in many theoretical models of the glass transition [347–351]. Glass-forming liquids are usually characterized by the temporal behaviour of the relaxation function describing the response to a small perturbation. The  $\alpha$ -relaxation in supercooled liquids can be described at long times by a stretched exponential function, called the Kohlrausch–Williams–Watt function [352–354]:

$$\Phi(t) \propto \exp \left[ - \left( \frac{t}{\tau} \right)^\beta \right] \quad \text{where } 0 < \beta \leq 1. \quad (18)$$

Starting from a value of 0.3–0.6 for molecular liquids and polymer melts at  $T_g$ , the stretching exponent  $\beta$  tends to 1 at high temperature. However, the absolute value of  $\beta$  remains controversial because its estimation depends on the experimental technique employed and on the theoretical model used to analyse the data. The non-exponential time dependence of the relaxation function at temperatures close to  $T_g$  is related to heterogeneous rather than homogeneous properties of the system. Several experiments probing the existence of such dynamical heterogeneities have been reported during the last decade [351, 355–359]. These studies have shown the existence of a supermolecular length scale of several molecular diameters characteristic of the inhomogeneous structure of the glass. The observation of heterogeneous domains within the glass phase has led to the understanding that much of the phenomenology of the glass transition is directly connected to space and time heterogeneities of the response functions of the system. While the glass phase is stable over several orders of magnitude of time (from  $10^{-12}$  s to centuries), the space heterogeneities seem to be characterized by the scale of a few nanometres only. However, it is worth mentioning that no structural evidence of these heterogeneous nanoscopic clusters has been found so far. Despite an important effort to understand the physics of glass transitions, the origin of the viscous slowing down of supercooled liquids is not clearly understood yet and possible theoretical explanations are still hotly debated.

Investigation of the relaxation properties of confined supercooled liquids provides important information on the nature of the dynamical processes involved in the phenomenon of glass transition [6]. On the other hand, the analysis of results for confined glasses is not straightforward since important surface effects arise from the wall/fluid interaction (see sections 4.1 and 4.2). Both static and dynamical properties of the confined liquid are affected

by the interaction with the wall, and therefore depend on the previous surface treatment of the porous material. A current approach in the literature is to combine several complementary techniques and various systems to disentangle the effects and overcome the particularities of each experimental probe or porous geometry. Significant advances in recent computer simulations (model or realistic) [309, 360–367] also provide some insight into the microscopic properties of confined fluids. In MD simulations of toluene confined in cylindrical pores of immobile molecules of toluene at the same density [366], it is shown that the slowing down of the dynamics depends on the distance of the molecules from the walls inside the pore, making the averaged quantities (comparably to the experimental situation) apparently more stretched with a slower characteristic time. The length scale on which the influence of the wall on the liquid dynamics vanishes is of the order of  $\sigma$  (close to the size of a contact layer) for a pore of 15 Å radius at  $T = 200$  K, the dynamics of the inner molecules remaining isotropic but still slower by one order magnitude than that of the bulk at the same temperature. One should mention here a rather new extension of the mode coupling theory (MCT) for the study of the dynamics in confinement [368].

As in the case of the melting transition, the differences between the confined and bulk phases arise from both the nanoscopic confinement and the introduction of fluid/wall interactions. Despite the large number of experimental and theoretical results that report increasing, decreasing or constant glass transition temperature as a function of the pore size (see the recent review by Alcoutlabi and McKenna [6]), no clear picture of the behaviour of confined glasses has been obtained so far [30, 369–371]. This lack of general understanding is related to the diversity of features that these systems exhibit, some of these properties being specific to the technique or the material used. Among the different effects induced by nanoscopic confinement, some specific features result from: size restriction or ‘cut-off effect’, surface adsorption, topology (1-, 2- or 3D) of the porous geometry, and density of the confined fluid. The ‘cut-off effect’ describes the fact that any putative characteristic length in a supercooled liquid cannot extend beyond the typical pore size. Consequently, the cut-off effect should lead to a less pronounced increase of the relaxation time on approaching  $T_g$  once the characteristic length reached the pore size. Pure geometric confinement, i.e. finite-size effect, would prevent the growth of any cooperativity length and thus moderate the slowing down of the structural relaxation. This would lead to a lower glass transition temperature, as is indeed observed. This effect competes with the surface-induced increased slowing down of the dynamics. By cooling methylpentane in silica pores, Richert and Yang observed that solidification starts at the pore surface (which indicates that the silica surface is strongly attractive for this adsorbate), whereas lower temperatures are required to observe the glass transition of the inner pore liquid (see figure 12) [119]. This leads to a broadening of the region of the glass transition with decreasing pore size as observed by calorimetric measurements on confined toluene in MCM-41 and SBA-15 (see figure 13) [77]; the molecules near the interface appear immobile on the timescale of viscous flow near the centre of the pore, thereby confining the liquid further; for small pores this leads to a higher value of  $T_g$  than that of the bulk (see figure 14). The topology of the pores may also play a role in the resulting phenomenon, since if pores are interconnected, such immobile layers may eventually prohibit liquid flow among pores and create a crossover from an isobaric (constant pressure) to an isochoric (constant volume) path [372].

An increase of the glass transition temperature of liquids confined in small pores has also been observed for *o*-terphenyl in non-silanized CPG and SBA-15 [128, 373], for polypropylene glycol confined in CPG [121] and for methanol [288]. Nevertheless some of the results obtained by DSC or dielectric relaxation studies are apparently controversial showing, for *o*-terphenyl or salol confined in silanized CPG, a strong decrease of  $T_g$  [128, 374, 375] of about 25 K for the smallest pore with a diameter of 2.5 nm. However, all these results can be rationalized when,

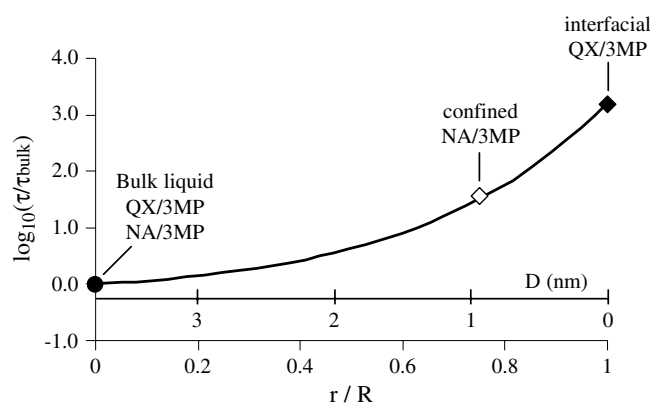


**Figure 12.** The spatial distribution of the dynamics of a simple glass-forming liquid, 3-methylpentane (3MP) in its viscous regime, geometrically confined to the 7.5 nm diameter pores of sol-gel processed silica. The results are obtained from triplet state solvation dynamics measurements. Note that the timescale of molecular motion changes by over three orders of magnitude within several nanometres (adapted from Richert and Yang [119]).

on the one hand, the density of the confined liquid, and, on the other hand, the chemical nature of the surface, i.e. fluid–wall interactions, are taken into account, at least for pore diameters of about  $10\sigma$  or smaller.

Hence, it has been shown recently that confinement of a weakly interacting fluid (benzene, toluene) [77, 118] in porous silica may notably affect its static properties, leading to glassy phases with significantly lower density at low temperature; similarly for confined methanol, the density seems to be systematically smaller than the bulk by a few per cent [288]. Thus, comparison with the bulk glass behaviour at ambient pressure is questionable for the glasses obtained in the smallest pores. Accordingly, the strong decrease of  $T_g$  of an archetypical glass-forming liquid, *o*-terphenyl, confined in CPG [128] can be explained by the lower value of the density in the confined phase relative to the bulk, together with the inability to equilibrate the confined liquid in the timescale of experiment. The authors proposed that the density change could be proportional to the liquid-pore surface tension and inversely proportional to the pore size.

The glass transition signature is, as for bulk materials, a jump of the heat capacity and of the thermal expansion at  $T_g$  as measured by adiabatic calorimetry and by the density of the confined fluids, or by the temperature at which the system reaches an averaged relaxation time of, say, 100 s by using spectroscopic techniques. An important feature observed by calorimetric measurements is the quite large broadening of the region of the glass transition with decreasing pore size, from a few degrees to several tens of degrees. This temperature broadening is consistent with the weaker increase of the mean square displacement observed in the smallest pores [118, 376]. In this picture an extended temperature range for the calorimetric glass transition means a highly stretched relaxation function and a broad distribution of relaxation times; the dynamics of a confined fluid is then highly heterogeneous and this character is induced by the wall boundary conditions, an amount of fluid remaining trapped at the surface. The observed broadening of the glass transition region continuously increases with decreasing pore size, which agrees well with this picture. For timescales of less than a few seconds, it is also expected that the stretching of the structural relaxation function increases (i.e.  $\beta$  in equation (18) decreases) and requires several decades in time to decay entirely, as recently stressed in quasi-elastic neutron and light scattering studies of salol and *o*-terphenyl confined

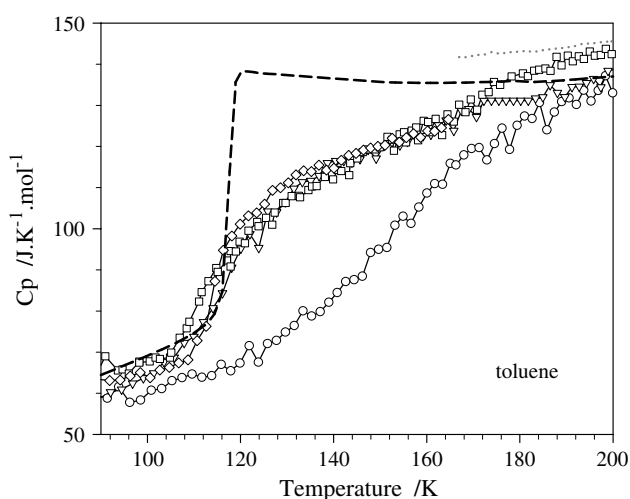


**Figure 13.** The heat capacity of bulk and confined toluene as measured by adiabatic calorimetry in the temperature range of the glass transition. Pore diameters of MCM-41 and SBA-15:  $\circ$  2.4 nm,  $\nabla$  3.5 nm,  $\square$  4.7 nm,  $\diamond$  8.7 nm; dotted line, bulk  $C_7D_8$ ; dashed line, bulk  $C_7H_8$  (adapted from Morineau *et al* [77]).

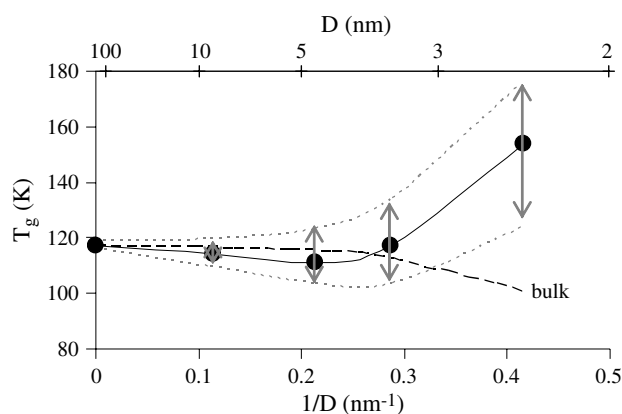


**Figure 14.** Pore size dependence of the glass transition temperature of toluene, where confined  $T_g$ 's are defined at the maximum of the heat capacity derivative; the arrows represent the widths of the transition region. The dashed line shows the bulk value,  $T_{g,bulk}$  ( $d = \infty$ ;  $\rho$ ) after a density correction, corresponding to the density  $\rho$  in the pore (adapted from Morineau *et al* [77]).

in CPG [128, 377] or in the regular SBA-15 [118]. The similarity between these results suggests that the regular or irregular shape of the pores is not the prevailing input for the glass formation, as for melting phase transitions, but that the chemical nature and the shape of the interface play the dominant role in the dynamical process.

However, the decrease in the glass transition temperature observed for pore sizes larger than  $10\sigma$  suggests that finite-size effects may dominate the dynamics of supercooled liquids in so far as no changes in the inner density are observed (the most pronounced being observed for a pore size of the order of 10 molecular diameters); for very large pore sizes (e.g. larger than  $100\sigma$ ) no difference between bulk and confined liquids is observed, as found for microemulsion droplets [378, 379]. However, these latter matrices are soft compared with the rigid silica wall,

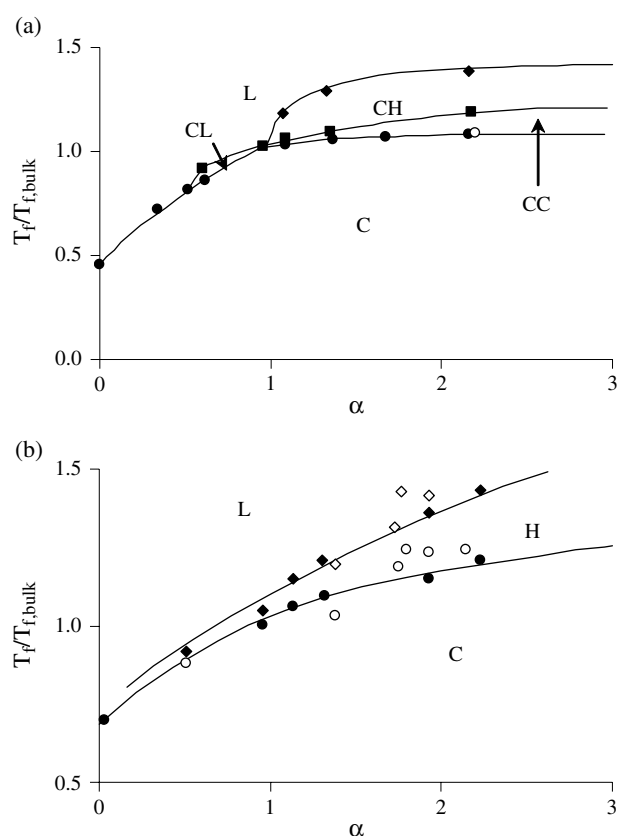


**Figure 15.** (a) Global phase diagram for a pore width of  $H^* = 7.5$  from simulation (filled symbols). Five different phases are observed: liquid (L), contact-hexatic (CH), contact-crystal (CC), contact-liquid (CL) and crystalline (C). The point marked by the open circle is the experimental result by Klein and Kumacheva for cyclohexane in a mica slit pore (SFA) [114]. (b) Global phase diagram for a pore width of  $H^* = 3$  from simulation (filled symbols) and experiment (open symbols). Three different phases are observed: liquid (L), hexatic (H) and crystalline (C). Experimental results are for (reading from left to right) water, nitrobenzene, aniline, methanol, carbon tetrachloride and benzene (from Radhakrishnan *et al* [11]).

which may induce novel features in the overall dynamics [380]. Unfortunately, the originally expected estimation of a supermolecular length or spatial information on the dynamical heterogeneities in the bulk supercooled liquid close to the glass transition is not fulfilled and remains only speculative until we understand the mechanism involved at the interface between the confined fluid and the wall. Moreover, there is no obvious indication that the dramatic effect of confinement on the dynamics of confined liquids is related to an increase of the correlation length of cooperative dynamics as the temperature approaches the glass transition.

## 5. Global phase diagrams

For simple adsorbates and pore geometries (slit or cylinder) it is possible to present global freezing phase diagrams in terms of a few variables, based on a corresponding state analysis [381]. Such an analysis [10, 11] shows that the phase transition temperature (in

dimensionless form) depends on three dimensionless variables,  $H^* = H/\sigma_{\text{ff}}$ ,  $\sigma_{\text{fw}}/\sigma_{\text{ff}}$  and  $\alpha = C\varepsilon_{\text{fw}}/\varepsilon_{\text{ff}}$ , where  $C$  depends on the pore geometry and solid wall structure (see equations (1) and (2) and associated discussion). When the diameters  $\sigma_{\text{fw}}$  and  $\sigma_{\text{ff}}$  are not very different, and the pore width exceeds the larger of the pore sieving regimes, the reduced transition temperature can be written in terms of only two variables as in equation (2),  $T_{\text{tr}}^* \approx f(H^*, \alpha)$ . For a strictly 2D square well fluid, Bladon and Frenkel [335] reported a strong dependence of the melting behaviour on the parameters of the intermolecular interaction. The authors reported two phase diagrams in the  $T$ - $\rho$  plane for different values of the range of the attractive interaction. Although qualitatively similar, the range of stability of the hexatic phase was found to be sensitive to the range of intermolecular interaction. A similar dependence of the melting scenario on the interparticle interaction was observed in experiments for colloidal particles interacting through different screened (effective) potentials [333, 334].

Schmidt and Lowen [141], using Monte Carlo simulations, studied the freezing of hard spheres confined between two parallel hard plates of various separations, interpolating between two and three dimensions. The coexistence conditions were obtained by identifying van der Waals loops in pressure versus density curves, and then applying a Maxwell construction. The full phase diagram for this model was mapped out for arbitrary density and plate separations lying between one and two sphere diameters. The phase diagram is found to exhibit a rich structure with a fluid phase and many different solid phases of buckled, layered and rhombic crystalline structure. For the finite system sizes studied in this work, the freezing transition was found to be first order. Solid–solid transitions were also observed upon further increase of the density. Some of these crystal transformations were found to be weakly first order.

The corresponding states principle in equation (2) states that the phase behaviour for two different adsorbates in two different materials will be the same at a given reduced pressure if they have the same values of  $H^*$  and  $\alpha$ . Thus, the construction of phase diagrams from a minimum of simulation or experimental data, provided they cover a suitably wide range of  $H^*$  and  $\alpha$  values, can be used to predict the phase behaviour of other systems that have not been studied. Global freezing phase diagrams for Lennard-Jones fluids in slit-shaped pores of widths  $H^* = 7.5$  and  $3.0$  and a bulk pressure of 1 atm have been reported [11]. The coexistence conditions of the two phases were obtained using Landau free energy calculations. In the larger pore, five different phases are observed: liquid, contact-hexatic, contact-crystal, contact-liquid and crystalline (see section 4.1 and figure 15(a)). The different phases were identified by their characteristic positional and orientational correlation functions. The freezing temperature shifts upward on confinement for values of  $\alpha$  greater than 0.95 (strongly attractive pores), and shifts downward for values of  $\alpha$  less than 0.95 (repulsive and weakly attractive pores). For strongly attractive pores, the contact layers freeze at a temperature higher than the inner layers, while for weakly attractive walls the contact layers freeze at a temperature lower than the inner layers; this leads to the formation of the contact-crystal (CC) and contact-liquid (CL) phases, respectively that were described in section 4.1. The contact-crystal phase is found to be thermodynamically stable in the region  $\alpha > 0.95$ , while the contact-liquid phase is stable in the region  $0.5 < \alpha < 0.95$ . For strongly attractive pores,  $\alpha > 0.95$ , the contact layers undergo a second liquid–hexatic phase transition that leads to the contact-hexatic phase (CH) (see solid diamonds in figure 15). For this pore width, comparison with experimental SFA data of Klein and Kumacheva [114] for the freezing of cyclohexane in a mica slit pore is in good agreement (within 5%) with the global phase diagram.

Figure 15 shows the global phase diagram for a slit pore of width  $H^* = 3$ , using molecular simulations as well as experimental measurements. For this width, the pore accommodates only two confined molecular layers. The phase boundaries from simulation and experiment are similar (the largest deviation was found to be 15%). As  $\alpha$  becomes smaller the temperature

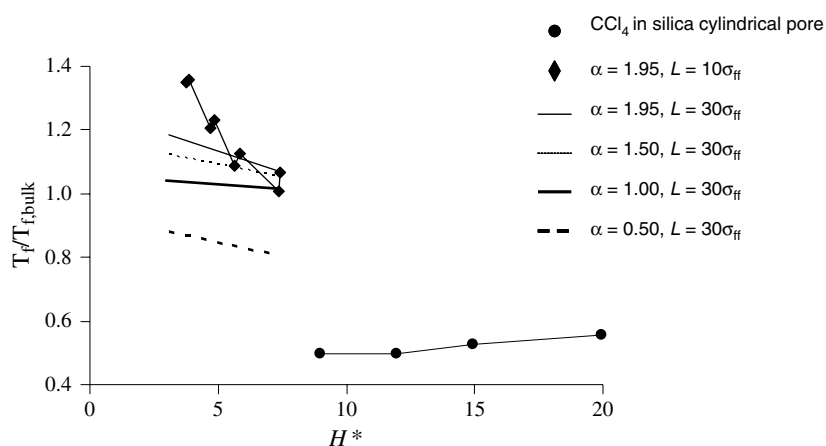


**Figure 16.** Global freezing diagram as a function of pore width for different  $\alpha$  values in slit and cylindrical confinements constructed using data from [11, 225, 239, 240]. The different values of  $L$  correspond to the system sizes used in the simulations. The difference between the curves corresponding to  $\alpha = 1.95, L = 30\sigma_{ff}$  and  $\alpha = 1.95, L = 10\sigma_{ff}$  is due to system size effects that are pronounced for these quasi-2D systems, as discussed in [124].

range where the hexatic phase is stable decreases. This is expected, since as  $\alpha$  becomes small the fluid–wall interactions are relatively weaker, and the adsorbate no longer arranges itself into well-defined quasi-2D layers. Similar global freezing diagrams as a function of pore width are shown in figure 16 for different values of  $\alpha$  and different system sizes (box length  $L$ ). The effect of a cylindrical confinement relative to a slit-like confinement is apparent by comparing the data for these two geometries of the same adsorbent material ( $\text{CCl}_4$  in a silica cylindrical pore is to be compared with the slit pore, with  $\alpha = 0.5$ ). The freezing temperature for the cylindrical pore is lower than that for the slit pore, a trend that was first understood by comparing the simulation results of Miyahara and Gubbins [233] and Maddox and Gubbins [237].

Experimentally, one can alternatively fix a given value of  $\alpha$  and explore the pore size dependence of the phase transitions such as melting and glass formation for different geometries. This leads to a new phase diagram of the condensed phases, supercooled liquid, glass and crystal (see figure 17).

## 6. Conclusion

There has been significant progress in our understanding of melting and freezing in simple systems (simple one-component adsorbate molecules in well-characterized pores of simple geometry) over the past decade. Corresponding state relations, such as equations (1) and (2), and the global phase diagrams (section 5) provide a useful framework for the discussion of the behaviour of real systems. Most of the systems studied experimentally have relatively weakly attractive pore walls (small  $\alpha$ , e.g. many silica systems) and exhibit a lowering of the freezing temperature, and may exhibit a contact layer near the wall that is fluid even though the inner adsorbed phase is crystalline. Such behaviour is seen in both the simulations and experiments for many such systems. For strongly attractive walls (large  $\alpha$ , e.g. carbons or mica) an increase in the freezing temperature over the bulk value may occur, and a contact layer that is crystalline while inner layers remain fluid may be observed. Again, such behaviour has been observed in both the simulations and experiment. In general it is easier to understand

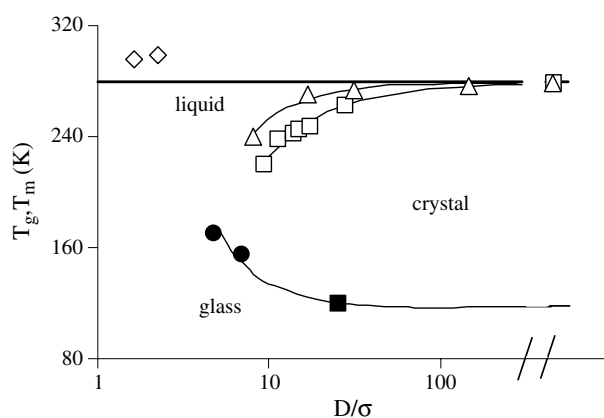


**Figure 17.** Phase diagram of confined benzene showing both the melting and vitrification temperatures as a function of the reduced pore diameter  $D/\sigma$ , where  $\sigma \sim 5 \text{ \AA}$  is the van der Waals diameter of the molecule: ( $\square$ ) melting point of benzene confined in hydroxylated SBA-15 [72]; ( $\triangle$ ) melting point of benzene confined in silanized CPG [73]; ( $\diamond$ ) melting point of benzene confined in ACF [224]; ( $\bullet$ ) glass transition temperature of benzene confined in MCM-41; ( $\blacksquare$ ) glass transition temperature of benzene confined in microemulsion [378].

freezing behaviour in pores of slit rather than cylindrical geometry; the additional geometrical hindrance effect in the latter case tends to inhibit freezing in small pores, leading to glassy phases or microscopic domains that are defective crystals surrounded by amorphous regions. Unfortunately, porous materials with slit-shaped pores are relatively few, the principal examples being the mica surfaces of the SFA and certain carbons.

Even for simple systems, some difficulties remain. In the simulations the principal difficulties are finite-size effects, and the degree of realism of the models used. It is important to study system size effects, to calculate free energies and to carry out a finite-size scaling analysis to ensure that the observed results are not an artefact of a small system size or metastability. Many of the models used for the intermolecular forces and the atomic structure of the pore material have been simplified, making it difficult to make effective comparisons with experiment. In the experiments difficulties include poorly characterized materials and possible surface contamination. Scattering studies, needed to determine the structure of the confined phase, are difficult because of the small amount of adsorbed material. Often, the interpretation of the experimental results is difficult and can lead to controversy.

For more complex adsorbates and pore structures the difficulties of interpreting experimental results is increased, as is that of bringing experiment and theory together in a fruitful way. The great majority of the studies reported so far are for pure confined phases; very little is known of the freezing behaviour of confined mixtures [382–384].

## Acknowledgments

We wish to thank Henry Bock (North Carolina State University), Gerhard H Findenegg (Technical University of Berlin), Francisco R Hung (North Carolina State University), Jacob Klein (University of Oxford) and Eugenia Kumacheva (University of Toronto) for helpful discussions. We are grateful for support of our work by the National Science Foundation (grant CTS-0211792), the US Department of Energy (grant DE-FG02-98ER14847), the Polish Science Research Committee (KBN grant 2PO3B01424) and the Petroleum Research Fund of

the American Chemical Society. International cooperation was made possible through a NATO Collaborative Linkage Grant (no PST.CLG.978802).

## References

- [1] Masuda H and Fukuda K 1995 *Science* **268** 1466
- [2] Ajayan P M, Stephan O, Redlich Ph and Colliex C 1999 *Nature* **375** 564
- [3] Harris P J F 1999 *Carbon Nanotubes and Related Structures. New Materials for the Twenty-First Century* (Cambridge: Cambridge University Press)
- [4] Sloan J, Novotny M C, Bailey S R, Brown G, Xu C, Williams V C, Friedrichs S, Flahaut E, Callender R L, York A P E, Coleman K S, Green M L H, Dunin-Borkowski R E and Hutchison J L 2000 *Chem. Phys. Lett.* **239** 61
- [5] Zhakidov A A, Baughman R H, Iqbal Z and Cui C X 1998 *Science* **282** 897
- [6] Zhang Z B, Gekhtman D, Dresselhaus M S and Ying J Y 1999 *Chem. Mater.* **11** 1659
- [7] Alcoutlabi M and McKenna G B 2005 *J. Phys.: Condens. Matter* **17** R461
- [8] Heremans J, Thrush C M, Lin Y M and Cronin S 2000 *Phys. Rev. B* **61** 2921
- [9] Liu K, Chien C L, Searson P C and Kui Y Z 1998 *Appl. Phys. Lett.* **73** 1436
- [10] Eyraud C, Quinson J F and Brun M 1988 *Characterization of Porous Solids* ed K Unger, J Rouquerol, K S W Sing and H Kral (Amsterdam: Elsevier) p 307
- [11] Radhakrishnan R, Gubbins K E and Sliwinska-Bartkowiak M 2000 *J. Chem. Phys.* **112** 11048
- [12] Radhakrishnan R, Gubbins K E and Sliwinska-Bartkowiak M 2002 *J. Chem. Phys.* **116** 1147
- [13] Chaikin P M and Lubensky T C 1995 *Principles of Condensed Matter Physics* (Cambridge: Cambridge University Press) p 192
- [14] Grier D G and Murray C A 1995 *Ordering and Phase Transitions in Colloidal Systems* ed A K Arora (New York: VCH)
- [15] Frenkel D and McTague J 1980 *Annu. Rev. Phys. Chem.* **31** 491
- [16] Lindemann F 1910 *Z. Phys.* **11** 609
- [17] Girafalco L A 2000 *Statistical Mechanics of Solids* (New York: Oxford University Press) p 280
- [18] Nelson D R 2002 *Defects and Geometry in Condensed Matter Physics* (Cambridge: Cambridge University Press) p 276
- [19] Grimvall G and Sjodin S 1974 *Phys. Scr.* **10** 340
- [20] Born M 1939 *J. Chem. Phys.* **7** 591
- [21] See also Tallon J L 1979 *Phil. Mag. A* **39** 151
- [22] Mott N F and Gurney R W 1939 *Trans. Faraday Soc.* **35** 364
- [23] Joós B 1996 *Dislocations in Solids* ed F R N Nabarro and M S Duesbery (Amsterdam: Elsevier) chapter 55, p 505
- [24] Debenedetti P G 1996 *Metastable Liquids: Concepts and Principles* (Princeton, NJ: Princeton University Press) chapter 3
- [25] Idziak S H J, Safinya C R, Hill R S, Kraiser K E, Ruths M, Warriner H E, Steinberg S, Liang K S and Israelachvili J N 1994 *Science* **264** 1915
- [26] Kumacheva E and Klein J 1998 *J. Chem. Phys.* **108** 7010
- [27] Bock H and Schoen M 2000 *J. Phys.: Condens. Matter* **12** 1545
- [28] Bock H, Diestler D J and Schoen M 2001 *Phys. Rev. E* **64** 046124
- [29] Meyer R R, Sloan J, Dunin-Borkowski R E, Kirkland A I, Novotny M C, Bailey S R, Hutchison J L and Green M L H 2000 *Science* **289** 1324
- [30] Wilson M 2002 *J. Chem. Phys.* **116** 3027
- [31] Rault J 2003 *J. Macromol. Sci. Phys. B* **42** 1235
- [32] Frick B, Zorn R and Buttner H (ed) 2000 International workshop on dynamics in confinement *J. Physique IV* **10** 3 and references therein
- [33] Frick B, Koza M and Zorn R (ed) 2003 Dynamics in confinement *Eur. J. Phys. E* **12** (1) and references therein
- [34] Iannacchione G S, Crawford G P, Zumer S, Doane J W and Finotello D 1993 *Phys. Rev. Lett.* **71** 2595
- [35] Bellini T, Radzihovsky L, Toner J and Clark N A 2001 *Science* **294** 1074
- [36] Martinez-Miranda L J 2002 *J. Appl. Phys.* **91** 6452
- [37] Kutnjak Z, Kralj S, Lahajnar G and Zumer S 2003 *Phys. Rev. E* **68** 021705
- [38] Murray C A and Grier D G 1996 *Annu. Rev. Phys. Chem.* **47** 421
- [39] Dickman R, Attard P and Simonian V 1997 *J. Chem. Phys.* **107** 205
- [40] Cui B, Lin B and Rice S A 2001 *J. Chem. Phys.* **114** 9142

- [39] Cui B, Lin B, Sharma S and Rice S A 2002 *J. Chem. Phys.* **116** 3119
- [40] Cui B, Lin B and Rice S A 2003 *J. Chem. Phys.* **119** 2386
- [41] Gelb L D, Gubbins K E, Radhakrishnan R and Sliwinski-Bartkowiak M 1999 *Rep. Prog. Phys.* **62** 1573
- [42] Christenson H K 2001 *J. Phys.: Condens. Matter* **13** R95
- [43] Baerlocher Ch, Meier W M and Olson D H 2001 *Atlas of Zeolite Framework Types* 5th edn (Amsterdam: Elsevier)  
See also the database of zeolite structures of the International Zeolite Association  
<http://www.iza-structure.org/databases/>
- [44] Auerbach S M, Carrado K A and Dutta P K 2003 *Handbook of Zeolite Science and Technology* (New York: Dekker)
- [45] Iijima S 1991 *Nature* **354** 56
- [46] Ajayan P M 1999 *Chem. Rev.* **99** 1787
- [47] Ajayan P M 1996 *Carbon Nanotubes: Preparation and Properties* ed T W Ebbesen (Boca Raton, FL: Chemical Rubber Company)
- [48] Beck J S, Vartuli J C, Roth W J, Leonowicz M E, Kresge C T, Schmitt K D, Chu C T-W, Olson D H, Sheppard E W, McCullen S B, Higgins J B and Schlenker J L 1992 *J. Am. Chem. Soc.* **114** 10834
- [49] Zhao X S, Lu G Q and Millar G J 1996 *Ind. Eng. Chem. Res.* **35** 2075
- [50] Soler-Illia G J de A A, Sanchez C, Lebeau B and Patarin J 2002 *Chem. Rev.* **102** 4093
- [51] Zhao D, Feng J, Huo Q, Melosh N, Fredrickson G H, Chmelka B F and Stucky G D 1998 *Science* **279** 548
- [52] Imperor-Clerc M, Davidson P and Davidson A 2000 *J. Am. Chem. Soc.* **122** 11925
- [53] Ryoo R, Ko C H, Kruk M, Antochshuk V and Jaroniec M 2000 *J. Phys. Chem. B* **104** 11465
- [54] Bisi O, Ossicini S and Pavesi L 2000 *Surf. Sci. Rep.* **38** 1
- [55] Haller W 1983 *Solid Phase Biochemistry* ed W H Scouten (New York: Wiley) chapter 11, p 535
- [56] Levitz P, Ehret G, Sinha S K and Drake J M 1991 *J. Chem. Phys.* **95** 6151
- [57] Iler R K 1979 *The Chemistry of Silica* (New York: Wiley)
- [58] Pekala R W, Alviso C T, Kong F M and Hulsey S S 1992 *J. Non-Cryst. Solids* **145** 90
- [59] Hanzawa Y, Kaneko K, Yoshizawa N, Pekala R W and Dresselhaus M S 1998 *Adsorption* **4** 187
- [60] Bandoz T J, Biggs M J, Gubbins K E, Hattori Y, Iiyama T, Kaneko K, Pikunic J and Thomson K T 2003 *Chemistry and Physics of Carbon* vol 28, ed L R Radovic (New York: Dekker) p 41
- [61] Bansal R C, Donnet J B and Stoeckli F 1988 *Active Carbon* (New York: Dekker)
- [62] Yoshizawa N, Maruyama K, Yamada Y and Zielinska-Blajet M 2000 *Fuel* **79** 1461
- [63] Pikunic J, Clinard C, Cohaut N, Gubbins K E, Guet J M, Pellenq R J M, Rannou I and Rouzaud J-N 2003 *Langmuir* **19** 8565
- [64] Mays T J 1999 *Carbon Materials for Advanced Technologies* ed T D Burchell (Amsterdam: Pergamon) chapter 3
- [65] Huang Z H, Kang F, Huang W, Yang J B, Liang K M, Cui M L and Cheng Z 2002 *J. Colloid Interface Sci.* **249** 453
- [66] Cool P, Vansant E F, Poncelet G and Schoonheydt R A 2002 *Handbook of Porous Solids* vol 2, ed F Schuth, K S W Sing and J Weitkamp (New York: Wiley-VCH) chapter 4.4
- [67] Cracknell R F, Koh C A, Thompson S M and Gubbins K E 1993 *Mater. Res. Soc. Symp. Proc.* **290** 135
- [68] Skipper N T 1998 *Mineral. Mag.* **62** 657
- [69] De Siqueira A V C, Lobban C, Skipper N T, Williams G D, Soper A K, Done R, Dreyer J W, Humphreys R J and Bones J A R 1999 *J. Phys.: Condens. Matter* **11** 9179
- [70] Hill J O 1992 *Thermochim. Acta* **200** 187  
Mathot V B F 2000 *Thermochim. Acta* **355** 1
- [71] Booth H F and Strange J H 1998 *Mol. Phys.* **93** 263
- [72] Dosseh G, Xia Y and Alba-Simionesco C 2003 *J. Phys. Chem. B* **107** 6445
- [73] Jackson C L and McKenna G B 1990 *J. Chem. Phys.* **93** 9002
- [74] Gedat E, Schreiber A, Albrecht J, Emmler T, Shenderovich I, Findenegg G H, Limbach H H and Buntkowsky G 2002 *J. Phys. Chem. B* **106** 1977
- [75] Schönhals A *et al* 2004 *Preprint*
- [76] Suga H 2000 *Thermochim. Acta* **355** 69  
Matsuo T and Yamamuro O 1999 *Thermochim. Acta* **330** 155  
Van Miltenburg J C, Van Genderen A C G and Van den Berg G J K 1998 *Thermochim. Acta* **319** 151
- [77] Morineau D, Xia Y and Alba-Simionesco C 2002 *J. Chem. Phys.* **117** 8966
- [78] Geil B, Fujara F and Silescu H 1998 *J. Magn. Reson.* **130** 18
- [79] Kimmich R 1997 *NMR Tomography, Diffusometry, Relaxometry* (Berlin: Springer)  
Schmidt-Rohr K and Spiess H W 1994 *Multidimensional Solid State NMR and Polymers* (London: Academic)

- [80] Packer K J 2003 *Magn. Reson. Imaging* **21** 163
- [81] Kimmich R 2002 *Chem. Phys.* **284** 253
- [82] Watson A T, Hollenshead J T, Uh J and Chang C T P 2002 *Annu. Rep. NMR Spectrosc.* **48** 113
- [83] Barrie P J 2000 *Annu. Rep. NMR Spectrosc.* **41** 265
- [84] Hansen E W, Schmidt R, Stocker M and Akporiaye D 1995 *J. Phys. Chem.* **99** 4148
- [85] Hansen E W, Stocker M and Schmidt R 1996 *J. Phys. Chem.* **100** 2195
- [86] Hansen E W, Simon C, Haugrud R, Raeder H and Bredesen R 2002 *J. Phys. Chem. B* **106** 12396
- [87] Strange J H, Rahman M and Smith E G 1993 *Phys. Rev. Lett.* **71** 3589
- [88] Duffy J A and Alam M A 2000 *Langmuir* **16** 9513
- [89] Bartos J, Sausa O, Kristiak J, Blochowicz T and Rossler E 2001 *J. Phys.: Condens. Matter* **13** 11473
- [90] Wilkinson N J, Alam M A, Clayton J M, Evans R, Fretwell H M and Usmar S G 1992 *Phys. Rev. Lett.* **69** 3535
- [91] Tabor D and Winterton R H S 1969 *Proc. R. Soc.* **312** 435
- [92] Israelachvili J N and Tabor D 1972 *Proc. R. Soc.* **331** 19
- [93] Israelachvili J N and Tabor D 1973 *Prog. Surf. Membr. Sci.* **7** 1
- [94] Israelachvili J N and Adams G E 1978 *J. Chem. Soc. Faraday Trans. I* **74** 975
- [95] Israelachvili J N 1987 *Acc. Chem. Res.* **20** 415
- [96] Israelachvili J N 1992 *Intermolecular and Surface Forces* 2nd edn (London: Academic) p 169
- [97] Horn R G, Clark D R and Clarkson M T 1988 *J. Mater. Res.* **3** 413
- [98] Horn R G, Smith D T and Haller W 1989 *Chem. Phys. Lett.* **162** 404
- [99] Hirz S J, Homola A M, Hadziioannou G and Frank C W 1991 *Langmuir* **8** 328
- [100] Klein J, Perahia D and Warburg S 1991 *Nature* **352** 143
- [101] Klein J and Kumacheva E 1998 *J. Chem. Phys.* **108** 6996
- [102] Heuberger M and Zäch M 2003 *Langmuir* **19** 1943
- [103] Lin Z and Granick S 2003 *Langmuir* **19** 7061
- [104] Kohonen M M, Meldrum F C and Christenson H K 2003 *Langmuir* **19** 975
- [105] Israelachvili J N, Alcantar N A, Maeda N, Mates T and Ruths M 2004 *Langmuir* **20** 3616
- [106] Morishige K and Kawano K 2000 *J. Chem. Phys.* **112** 11023
- [107] Silva D E, Sokol P E and Ehrlich S N 2002 *Phys. Rev. Lett.* **88** 155701
- [108] Bellissent-Funel M C, Chen H S and Zanotti J M 1995 *Phys. Rev. E* **51** 4558
- [109] Dore J 2000 *Chem. Phys.* **258** 327
- [110] Bruni F, Ricci M A and Soper A K 1998 *J. Chem. Phys.* **109** 1478
- [111] Soper A K, Bruni F and Ricci M A 1998 *J. Chem. Phys.* **109** 1486
- [112] Morineau D and Alba-Simionesco C 2003 *J. Chem. Phys.* **118** 9389
- [113] Xia Y, Dosseh G, Morineau D and Alba-Simionesco D 2005 *J. Chem. Phys.* submitted
- [114] Klein J and Kumacheva E 1995 *Science* **269** 816
- [115] Korb J P 2001 *Magn. Reson. Imaging* **19** 363
- [116] Levitz P E 2001 *Magn. Reson. Imaging* **19** 177
- [117] Schönhals A, Goering H, Schick C, Frick B and Zorn R 2003 *Eur. J. Phys. E* **12** 173
- [118] Alba-Simionesco C, Dosseh G, Dumont E, Geil B, Morineau D, Frick B, Teboul V and Xia Y 2003 *Eur. Phys. J. E* **12** 19
- [119] Richert R 2002 *J. Non-Cryst. Solids* **307–310** 50 and refs therein  
Richert R and Yang M 2003 *J. Phys. Chem. B* **107** 895
- [120] Schönhals A and Stauga R 1998 *J. Non-Cryst. Solids* **235–237** 450
- [121] Schönhals A, Goering H, Brzezinka K-W and Schinck Ch 2000 *J. Physique IV* **10** Pr 7-271
- [122] Arndt M, Stannarius R, Groothues H, Hempel E and Kremer F 1997 *Phys. Rev. Lett.* **79** 2077
- [123] Pelster R 1996 *Phys. Rev. B* **59** 9214
- [124] Radhakrishnan R, Gubbins K E and Sliwiska-Bartkowiak M 2002 *Phys. Rev. Lett.* **89** 076101
- [125] Chelkowski A 1993 *Physics of Dielectrics* 3rd edn (Warsaw: PWN)
- [126] Sliwiska-Bartkowiak M, Sowers S L and Gubbins K E 1997 *Langmuir* **13** 1182
- [127] Fung A W P, Wang Z H, Dresselhaus M S, Dresselhaus G, Penkala R W and Endo M 1994 *Phys. Rev. B* **49** 17325
- [128] Patkowski A, Ruths T and Fischer E W 2003 *Phys. Rev. E* **67** 021501
- [129] Fehr C, Dieudonne P, Sauvajol J L and Anglaret E 2003 *Phys. Rev. E* **67** 061706
- [130] Sokolov A 2003 private communication
- [131] Nicholson D and Parsonage N G 1982 *Computer Simulation and the Statistical Mechanics of Adsorption* (London: Academic)
- [132] Allen M P and Tildesley D J 1987 *Computer Simulation of Liquids* (Oxford: Clarendon)
- [133] Frenkel D and Smit B 2002 *Understanding Molecular Simulation* 2nd edn (New York: Academic)

- [134] Verlet L 1967 *Phys. Rev.* **159** 98
- [135] Gear C W 1971 *Numerical Initial Value Problems in Ordinary Differential Equations* (Englewood Cliffs, NJ: Prentice-Hall)
- [136] Evans D J and Morriss G P 1990 *Statistical Mechanics of Non-Equilibrium Liquids* (London: Academic)
- [137] Andersen H C 1980 *J. Chem. Phys.* **72** 2384
- [138] Nosé S 1984 *Mol. Phys.* **52** 255
- [139] Hoover W G 1985 *Phys. Rev. A* **31** 1695
- [140] Metropolis N, Rosenbluth A W, Rosenbluth M N, Teller A N and Teller E 1953 *J. Chem. Phys.* **21** 1087
- [141] Schmidt M and Löwen H 1996 *Phys. Rev. Lett.* **76** 4552
- [142] Schmidt M and Löwen H 1997 *Phys. Rev. E* **55** 7228
- [143] Panagiotopoulos A Z 1987 *Mol. Phys.* **61** 813
- [144] Chen B, Siepmann J I and Klein M L 2001 *J. Phys. Chem. B* **105** 9840
- [145] Panagiotopoulos A Z 1992 *Mol. Simul.* **9** 1
- [146] Jiang S and Gubbins K E 1995 *Mol. Phys.* **86** 599
- [147] Panagiotopoulos A Z 1987 *Mol. Phys.* **62** 701
- [148] Brennan J K and Dong W 2002 *J. Chem. Phys.* **116** 8948
- [149] McGrother S C and Gubbins K E 1999 *Mol. Phys.* **97** 955
- [150] Panagiotopoulos A Z, Quirke N, Stapleton M and Tildesley D J 1988 *Mol. Phys.* **63** 527
- [151] Smit B and Frenkel D 1989 *Mol. Phys.* **68** 951
- [152] Dominguez H, Allen M P and Evans R 1999 *Mol. Phys.* **96** 209
- [153] Yan Q L and de Pablo J J 1999 *J. Chem. Phys.* **111** 9509
- [154] Faller R, Yan Q and de Pablo J J 2002 *J. Chem. Phys.* **116** 5419
- [155] Marinari E and Parisi G 1992 *Europhys. Lett.* **19** 451
- [156] Yan Q L and de Pablo J J 2000 *J. Chem. Phys.* **113** 1276
- [157] Yan Q L and de Pablo J J 2003 *Phys. Rev. Lett.* **90** 035701
- [158] Wang F G and Landau D P 2001 *Phys. Rev. Lett.* **86** 2053
- [159] Bolhuis P G, Dellago C, Geissler P L and Chandler D 2000 *J. Phys.: Condens. Matter* **12** A147
- [160] Franzese G, Malescio G, Skibinsky A, Buldyrev S V and Stanley H E 2001 *Nature* **409** 692
- [161] Gelb L D and Gubbins K E 1997 *Phys. Rev. E* **55** R1290
- [162] Gelb L D and Gubbins K E 1997 *Phys. Rev. E* **56** 3185
- [163] Gelb L D and Muller E A 2002 *Fluid Phase Equilib.* **203** 1
- [164] Landau L D and Lifshitz E M 1980 *Statistical Physics* 3rd edn (London: Pergamon)
- [165] Torrie G M and Valleau J P 1974 *Chem. Phys. Lett.* **28** 578
- [166] Van Duijneveldt J S and Frenkel D 1992 *J. Chem. Phys.* **96** 4655
- [167] Lynden-Bell R M, Van Duijneveldt J S and Frenkel D 1993 *Mol. Phys.* **80** 801
- [168] Hohenberg P and Kohn W 1964 *Phys. Rev.* **136** B864
- [169] Mermin N D 1965 *Phys. Rev.* **137** A1441
- [170] Evans R 1979 *Adv. Phys.* **28** 143  
Evans R 1992 *Fundamentals of Inhomogeneous Fluids* ed D Henderson (New York: Dekker) chapter 3
- [171] Lowen H 1994 *Phys. Rep.* **237** 249
- [172] Singh Y 1991 *Phys. Rep.* **207** 351
- [173] Haymet A D J 1987 *Annu. Rev. Phys. Chem.* **38** 89
- [174] Baus M 1987 *J. Stat. Phys.* **48** 1129
- [175] Ramakrishnan T V and Yussouff M 1979 *Phys. Rev. B* **19** 2775
- [176] Haymet A D J and Oxtoby D W 1981 *J. Chem. Phys.* **74** 2559
- [177] Likos C N and Ashcroft N W 1993 *J. Chem. Phys.* **99** 9090
- [178] Curtin W A 1988 *J. Chem. Phys.* **88** 7050
- [179] Tarazona P 1984 *Mol. Phys.* **52** 81  
Tarazona P 1985 *Phys. Rev. A* **31** 2672
- [180] Curtin W A and Ashcroft N W 1985 *Phys. Rev. A* **32** 2909
- [181] Denton A R and Ashcroft N W 1989 *Phys. Rev. A* **39** 4701
- [182] Barrat J L and Xu H 1990 *J. Phys.: Condens. Matter* **2** 9445
- [183] Carraro C 2002 *Phys. Rev. Lett.* **89** 115702
- [184] Das C and Krishnamurthy H R 1998 *Phys. Rev. B* **58** R5889
- [185] Mermin N D and Wagner H 1966 *Phys. Rev. Lett.* **17** 1133
- [186] Halperin B I and Nelson D R 1978 *Phys. Rev. Lett.* **41** 121
- [187] Nelson D R and Halperin B I 1979 *Phys. Rev. B* **19** 2457
- [188] Young A P 1979 *Phys. Rev. B* **19** 1855

- [189] Kosterlitz J M and Thouless D J 1972 *J. Phys. C: Solid State Phys.* **5** L124  
Kosterlitz J M and Thouless D J 1973 *J. Phys. C: Solid State Phys.* **6** 1181
- [190] Chui S T 1982 *Phys. Rev. Lett.* **48** 933  
Chui S T 1983 *Phys. Rev. B* **28** 178
- [191] Strandburg K J 1988 *Rev. Mod. Phys.* **60** 161
- [192] Strandburg K J (ed) 1992 *Bond Orientational Order in Condensed Matter Systems* (New York: Springer)
- [193] Gray C G and Gubbins K E 1984 *Theory of Molecular Fluids* (Oxford: Clarendon) chapter 2 and appendix C
- [194] Maitland G C, Rigby M, Smith E B and Wakeham W A 1981 *Intermolecular Forces: Their Origin and Determination* (Oxford: Clarendon)
- [195] Nicholson D 1991 *Fundamentals of Adsorption* ed A B Mersmann and S E Scholl (New York: Engineering Foundation) p 3
- [196] Nicholson D and Pellenq R J M 1998 *Adv. Colloid Interface Sci.* **76/77** 179
- [197] Steele W A 1973 *Surf. Sci.* **36** 317
- [198] Steele W A 1974 *The Interaction of Gases with Solid Surfaces* (Oxford: Pergamon)
- [199] Peterson B K, Walton J P R B and Gubbins K E 1986 *J. Chem. Soc. Faraday Trans.* **2** 1789
- [200] Maddox M W and Gubbins K E 1995 *Langmuir* **11** 3988
- [201] Pellenq R J M and Nicholson D 1995 *Langmuir* **11** 1626
- [202] Lachet V, Boutin A, Tavitian B and Fuchs A H 1998 *J. Phys. Chem. B* **102** 9224
- [203] Cracknell R F, Gubbins K E, Maddox M W and Nicholson D 1995 *Acc. Chem. Res.* **28** 281
- [204] Nicholson D 1987 *Surf. Sci.* **181** L189
- [205] Bruch L W, Cole M W and Zaremba E 1997 *Physical Adsorption: Forces and Phenomena* (Oxford: Clarendon)
- [206] Vasiliev I, Ogut S and Chelikowski J R 2002 *Phys. Rev. B* **65** 115416
- [207] Hench L L and West J K 1995 *Annu. Rev. Mater. Sci.* **25** 37
- [208] Chang E K, Shirley E L and Levine Z H 2002 *Phys. Rev. B* **65** 035205
- [209] Serra L and Rubio A 1997 *Phys. Rev. Lett.* **78** 1428
- [210] Tell J L, Maris H J and Seidel G M 1983 *Phys. Rev. B* **28** 5122
- [211] Warnock J, Awschalom D D and Shafer M W 1986 *Phys. Rev. Lett.* **57** 1753
- [212] Krim J, Coulomb J P and Bouzidi J 1987 *Phys. Rev. Lett.* **58** 583–6
- [213] Torii R H, Maris H J and Seidel G M 1990 *Phys. Rev. B* **41** 7167
- [214] Sokol P E, Ma W J, Herwig K E, Soon W M, Wang Y, Koplik J and Banavar J R 1992 *Appl. Phys. Lett.* **61** 777
- [215] Molz E, Wong A P Y, Chan M H W and Beamish J R 1993 *Phys. Rev. B* **48** 5741
- [216] Unruh K M, Huber T E and Huber C A 1993 *Phys. Rev. B* **48** 9021
- [217] Overloop K and Van Gerven L 1993 *J. Magn. Reson. A* **101** 179
- [218] Edler K J, Reynolds P A, Trow F and White J W 1996 *J. Chem. Soc. Chem. Commun.* 155
- [219] Morishige K and Nobuoka K 1997 *J. Chem. Phys.* **107** 6965
- [220] Sliwinska-Bartkowiak M, Gras J, Sikorski R, Radhakrishnan R, Gelb L D and Gubbins K E 1999 *Langmuir* **15** 6060
- [221] Israelachvili J N, McGuiggan P M and Homola A M 1988 *Science* **240** 189
- [222] Hu H W, Carson G A and Granick S 1991 *Phys. Rev. Lett.* **66** 2758  
Granick S 1991 *Science* **253** 1374
- [223] Christenson H K 1997 *Colloids Surf.* **123/124** 355
- [224] Watanabe A and Kaneko K 1999 *Chem. Phys. Lett.* **305** 71
- [225] Radhakrishnan R, Gubbins K E, Watanabe A and Kaneko K 1999 *J. Chem. Phys.* **111** 9058
- [226] Kaneko K, Watanabe A, Iiyama T, Radhakrishnan R and Gubbins K E 1999 *J. Phys. Chem. B* **103** 7061
- [227] Sliwinska-Bartkowiak M, Radhakrishnan R and Gubbins K E 2001 *Mol. Simul.* **27** 323
- [228] Sliwinska-Bartkowiak M, Dudziak G, Sikorski R, Gras R, Gubbins K E and Radhakrishnan R 2001 *Phys. Chem. Chem. Phys.* **3** 1179
- [229] Castro M A, Clarke S M, Inaba A and Thomas R K 1997 *J. Phys. Chem. B* **101** 8878
- [230] Sliwinska-Bartkowiak M, Dudziak G, Gras R, Sikorski R, Radhakrishnan R and Gubbins K E 2001 *Colloids Surf. A* **187/188** 523
- [231] Hung F R, Dudziak G, Sliwinska-Bartkowiak M and Gubbins K E 2004 *Mol. Phys.* **102** 223
- [232] Evans R and Marini Bettolo Marconi U 1987 *J. Chem. Phys.* **86** 7138
- [233] Miyahara M and Gubbins K E 1997 *J. Chem. Phys.* **106** 2865
- [234] Raviv U, Laurat P and Klein J 2001 *Nature* **413** 51
- [235] Raviv U, Giasson S, Frey J and Klein J 2002 *J. Phys.: Condens. Matter* **14** 9275
- [236] Mugele F, Persson B, Zilberman S, Nitzan A and Salmeron M 2002 *Tribol. Lett.* **12** 123
- [237] Maddox M and Gubbins K E 1997 *J. Chem. Phys.* **107** 9659
- [238] Kanda H, Miyahara M and Higashitani K 2000 *Langmuir* **16** 8529

- [239] Radhakrishnan R and Gubbins K E 1999 *Mol. Phys.* **96** 1249
- [240] Sliwiska-Bartkowiak M, Dudziak G, Sikorski R, Gras R, Radhakrishnan R and Gubbins K E 2001 *J. Chem. Phys.* **114** 950
- [241] Heinbuch U and Fisher J 1989 *Phys. Rev. A* **44** 1044
- [242] Landman U, Luedtke W D and Ribarsky M W 1989 *J. Vac. Sci. Technol. A* **7** 2829
- [243] Bitsanis I and Hadziioannou G 1990 *J. Chem. Phys.* **92** 3827
- [244] Cui S T, Cummings P T and Cochran H D 1999 *J. Chem. Phys.* **111** 1273
- [245] Porcheron F, Rousseau B, Schoen M and Fuchs A H 2001 *Phys. Chem. Chem. Phys.* **3** 1155
- [246] Porcheron F, Rousseau B and Fuchs A H 2002 *Mol. Phys.* **100** 2109
- [247] Porcheron F, Schoen M and Fuchs A H 2002 *J. Chem. Phys.* **116** 5816
- [248] Thompson P A and Robbins M O 1990 *Phys. Rev. A* **41** 6930
- [249] Thompson P A and Robbins M O 1990 *Science* **250** 792
- [250] Gee M L, Mc Guiggan P M, Israelachvili J N and Homola A M 1990 *J. Chem. Phys.* **93** 1895
- [251] Lupkowski M and Van Swol F 1991 *J. Chem. Phys.* **95** 1995
- [252] Schoen M, Rhykerd C L, Diestler D J and Cushman J H 1989 *Science* **245** 1223
- [253] Cui S T, Cummings P T and Cochran H D 2001 *J. Chem. Phys.* **114** 7189
- [254] Cui S T, Cummings P T and Cochran H D 2001 *Fluid Phase Equilib.* **183/184** 381
- [255] Cui S T, Mc Cabe C, Cummings P T and Cochran H D 2003 *J. Chem. Phys.* **118** 8941
- [256] Persson B N J, Samoilov V N, Zilberman S and Nitzan A 2002 *J. Chem. Phys.* **117** 3897
- [257] Cottin-Bizonne C, Barrat J L, Bocquet L and Charlaix E 2003 *Nat. Mater.* **2** 237
- [258] Thompson P A, Grest G S and Robbins M O 1992 *Phys. Rev. Lett.* **68** 3448
- [259] Thompson P A, Robbins M O and Grest G S 1995 *Isr. J. Chem.* **35** 93
- [260] Bitsanis I O and Pan C 1993 *J. Chem. Phys.* **99** 5520
- [261] Manias E, Bitsanis I, Hadziioannou G and Ten Bricke G 1996 *Europhys. Lett.* **33** 371
- [262] Manias E, Hadziioannou G and Ten Bricke G 1996 *Langmuir* **12** 4587
- [263] Gao J, Luedtke W D and Landman U 1997 *J. Phys. Chem. B* **101** 4013
- [264] Wang J C and Fichtorn K 1998 *J. Chem. Phys.* **108** 1653
- [265] Bock H and Schoen M 2000 *J. Phys.: Condens. Matter* **12** 1569
- [266] Schoen M, Diestler D J and Cushman J H 1993 *Phys. Rev. B* **47** 5603
- [267] Ghatak C and Ayappa K G 2001 *Phys. Rev. E* **64** 051507
- [268] Ghatak C and Ayappa K G 2002 *Colloids Surf. A* **205** 111
- [269] Ayappa K G and Ghatak C 2002 *J. Chem. Phys.* **117** 5373
- [270] Vishnyakov A and Neimark V 2003 *J. Chem. Phys.* **118** 7585
- [271] Bock H, Gubbins K E and Ayappa K G 2005 *J. Chem. Phys.* **122** 094709
- [272] Patrykiewicz A, Sokolowski S, Zientarski T and Binder K 1995 *J. Chem. Phys.* **102** 8221
- [273] Patrykiewicz A, Sokolowski S and Zientarski T 1997 *Langmuir* **13** 1036
- [274] Patrykiewicz A, Sokolowski S, Zientarski T and Binder K 1999 *Langmuir* **15** 3642
- [275] Patrykiewicz A, Sokolowski S, Zientarski T and Binder K 1999 *Surf. Sci.* **421** 308
- [276] Patrykiewicz A and Sokolowski S 2001 *Langmuir* **17** 938
- [277] Patrykiewicz A, Sokolowski S and Binder K 2002 *Surf. Sci.* **512** 1
- [278] Patrykiewicz A, Sokolowski S and Binder K 2002 *J. Chem. Phys.* **117** 3369
- [279] Patrykiewicz A, Sokolowski S and Binder K 2000 *Surf. Sci. Rep.* **37** 207
- [280] Rhykerd C L, Schoen M, Diestler D J and Cushman J H 1987 *Nature* **330** 461
- [281] Curry J E, Zhang F, Cushman J H, Schoen M and Diestler D J 1994 *J. Chem. Phys.* **101** 10824
- [282] Patrykiewicz A, Salamacha L and Sokolowski S 2003 *J. Chem. Phys.* **118** 1891
- [283] Salamacha L, Patrykiewicz A, Sokolowski S and Binder K 2003 *J. Chem. Phys.* **120** 1017
- [284] Dominguez H, Patrykiewicz A and Sokolowski S 2003 *Mol. Phys.* **101** 1867
- [285] Camara L G and Bresme F 2003 *J. Chem. Phys.* **119** 2792
- [286] Vishnyakov A, Piotrovskaya E M and Brodskaya E N 1998 *Adsorption* **4** 207
- [287] Morineau D, Dosshe G, Alba-Simionesco C and Llewellyn P 1999 *Phil. Mag. B* **11/12** 1847
- [288] Morineau D, Guegan R, Xia Y and Alba-Simionesco C 2004 *J. Chem. Phys.* **121** 1466
- [289] Bellissent-Funel M C 2002 *J. Mol. Liq.* **96/97** 287
- [290] Hartnig C, Witshel W, Spohr E, Gallo P, Ricci M A and Rovere M 2000 *J. Mol. Liq.* **85** 127
- [291] Takei T, Konishi T, Fuji M, Watanabe T and Chikazawa M 1995 *Thermochim. Acta* **267** 159
- [292] Kempinski M, Sliwiska-Bartkowiak M and Kempinski W 2003 *Rep. Mol. Phys.* **55** 76
- [293] Kempinski M, Sliwiska-Bartkowiak S and Kempinski W 2004 *Nonlinear Dielectrics Phenomena in Complex Liquids (NATO Science Series II, Mathematics, Physics and Chemistry, 157)* ed S Rzoska and V Zhelezny, Kluwer Academic pp 387–2

- [294] Stankowski J, Piekara-Sady L, Kempinski W, Huminiecki O and Szczaniecki P B 1997 *Fullerene Sci. Technol.* **5** 1203
- [295] Buttet J, Car R and Myles C W 1982 *Phys. Rev. B* **26** 2414
- [296] Myles C W 1982 *Phys. Rev. B* **26** 2648
- [297] Stapf S and Kimmich R 1997 *Chem. Phys. Lett.* **275** 261
- [298] Dosseh G and Fuchs A H 1991 *Z. Naturf. A* **46** 917
- [299] Mu R, Xue Y, Henderson D O and Frazier D O 1996 *Phys. Rev. B* **53** 6041
- [300] Jackson C L and McKenna G B 1996 *Chem. Mater.* **8** 2128
- [301] Sklari S, Rahiala H, Stathopoulos V, Rosenholm J and Pomonis P 2001 *Micropor. Mesopor. Mater.* **49** 1
- [302] Baker J M, Dore J C and Behrens P 1997 *J. Phys. Chem. B* **101** 6226
- [303] Morishige K and Kawano K 1999 *J. Chem. Phys.* **110** 4867
- [304] Morishige K and Iwasaki H 2003 *Langmuir* **19** 2808
- [305] Dore J, Webber B, Hartl M, Behrens P and Hansen T 2002 *Physica A* **314** 501
- [306] Schreiber A, Ketelsen I and Findenegg G H 2001 *Phys. Chem. Chem. Phys.* **3** 1185
- [307] Faivre C, Bellet D and Dolino G 1999 *Eur. Phys. J. B* **7** 19
- [308] Tombari E, Salvetti G, Ferrari C and Johari G P 2005 *J. Chem. Phys.* **122** 104712
- [309] Koga K, Zeng X C and Tanaka H 1997 *Phys. Rev. Lett.* **76** 5262  
Koga K, Tanaka H and Zeng X C 2000 *Nature* **408** 564  
Koga K 2002 *J. Chem. Phys.* **116** 10882
- [310] Koga K and Tanaka H 2005 *J. Chem. Phys.* **122** 104711
- [311] Koga K, Gao G T, Tanaka H and Zeng X C 2001 *Nature* **412** 802
- [312] Takahara S, Nakano M, Kittaka S, Kuroda Y, Mori T, Hamano H and Yamaguchi T 1999 *J. Phys. Chem. B* **103** 5814
- [313] Wallacher D and Knorr K 2001 *Phys. Rev. B* **63** 104202
- [314] Pindak R, Moncton D E, Davey S C and Goodby J W 1981 *Phys. Rev. Lett.* **46** 1135
- [315] Brock J D, Birgeneau R J, Lister J D and Aharony A 1989 *Phys. Today* **42** 52
- [316] Brock J D, Aharony A, Birgeneau R J, Evans-Lutterodt K W, Litster J D, Horn P M, Stephenson G B and Tajbakhsh A R 1986 *Phys. Rev. Lett.* **57** 98
- [317] Chao C Y, Chou C F, Ho J T, Hui S W, Jin A J and Huang C C 1996 *Phys. Rev. Lett.* **77** 2750
- [318] Chou C F, Jin A J, Huang S W and Ho J T 1998 *Science* **280** 1424
- [319] Jiang I M, Stoebe T and Huang C C 1996 *Phys. Rev. Lett.* **76** 2910
- [320] Lin D L, Ou J T, Shi L P, Wang X R and Jin A J 2000 *Europhys. Lett.* **50** 615
- [321] Heiney P A, Stephens P W, Birgeneau R J, Horn P M and Moncton D E 1983 *Phys. Rev. B* **28** 6416
- [322] Specht E D, Sutton M, Birgeneau R J, Moncton D E and Horn P M 1984 *Phys. Rev. B* **30** 1589
- [323] McTague J P, Als-Nielsen J, Bohr J and Nielsen M 1982 *Phys. Rev. B* **25** 7765
- [324] Nagler S E, Horn P M, Rosenbaum T F, Birgeneau R J, Sutton M, Mochrie S G J, Moncton D E and Clarke R 1983 *Phys. Rev. B* **32** 7373
- [325] Greiser N G, Held A, Frahm R, Greeme R L, Horn P M and Suter M 1987 *Phys. Rev. Lett.* **59** 1625
- [326] Motteler F C 1985 *PhD Thesis* University of Washington
- [327] Kim H K, Zhang Q M and Chan M H W 1986 *Phys. Rev. Lett.* **56** 1579
- [328] Zhang Q M, Feng, Kim H K and Chan M H W 1986 *Phys. Rev. Lett.* **57** 1456
- [329] Zhang Q M, Kim H K and Chan M H W 1986 *Phys. Rev. B* **33** 5149
- [330] Bagchi K, Andersen H C and Swope W 1996 *Phys. Rev. Lett.* **76** 255
- [331] Jaster A 1999 *Phys. Rev. E* **59** 2594
- [332] Murray C H and Van Winkle D H 1988 *Phys. Rev. Lett.* **58** 1200
- [333] Marcus A H and Rice S A 1997 *Phys. Rev. E* **55** 637
- [334] Karnchanaphanurach P, Lin B and Rice S A 2000 *Phys. Rev. E* **61** 4036
- [335] Bladon P and Frenkel D 1995 *Phys. Rev. Lett.* **74** 2519
- [336] Zahn K, Lenke R and Maret G 1999 *Phys. Rev. Lett.* **82** 2721
- [337] Sliwinska-Bartkowiak M, Radhakrishnan R and Gubbins K E 2005 *Preprint*
- [338] Lee J and Kosterlitz J M 1990 *Phys. Rev. Lett.* **65** 137
- [339] De Gennes P G and Prost J 1995 *Molecular Theory of Liquid Crystals* (Oxford: Oxford University Press)
- [340] Stanley H E 1971 *Introduction to Phase Transitions and Critical Phenomena* (New York: Oxford University Press)
- [341] Jackle J 1986 *Rep. Prog. Phys.* **49** 171
- [342] Angell C A 1995 *Science* **267** 1924
- [343] Tarjus G, Kivelson D and Kivelson S 1997 *Supercooled Liquids: Advanced and Novel Application* ed J Fourkas *et al* (Baltimore, MD: American Chemical Society)

- [344] Ediger M D, Angell C A and Nagel S 1996 *J. Phys. Chem.* **100** 13200
- [345] Ngai K L 2000 *J. Non-Cryst. Solids* **275** 7
- [346] Alba-Simionesco C 2001 *C. R. Acad. Sci. Paris IV* (Editon speciale)
- [347] Adam G and Gibbs J H 1965 *J. Chem. Phys.* **43** 139
- [348] Kivelson D, Kivelson S A, Zhao X, Nussinov Z and Tarjus G 1995 *Physica A* **219** 27
- [349] Fischer E W, Donth E and Steffen W 1992 *Phys. Rev. Lett.* **68** 2344
- [350] Donati C and Jäckle J 1996 *J. Phys.: Condens. Matter* **8** 2733
- [351] Tarjus G, Kivelson S A, Nussinov Z and Viot P 2005 *J. Phys.: Condens. Matter* **17** R1–40
- [352] Kohlrausch R 1854 *Pogg. Ann. Phys.* **12** 393  
Kohlrausch R 1866 *Pogg. Ann. Phys.* **1** 207  
Kohlrausch R 1866 *Pogg. Ann. Phys.* **1** 399
- [353] Williams G and Watts D C 1970 *Trans. Faraday Soc.* **66** 80
- [354] Brawer S A 1984 *J. Chem. Phys.* **81** 954
- [355] Sillescu H 1999 *J. Non-Cryst. Solids* **243** 8
- [356] Ediger M D 2000 *Annu. Rev. Phys. Chem.* **51** 99
- [357] Schiener B, Bohmer R, Loidl A and Chamberlin R V 1996 *Science* **274** 752 and references therein
- [358] Kob W, Donati C, Plimton S J, Poole P H and Glotzer S C 1997 *Phys. Rev. Lett.* **79** 2827
- [359] Richert R 2000 *J. Chem. Phys.* **113** 8404
- [360] Fehr T and Löwen H 1995 *Phys. Rev. E* **52** 4016
- [361] Scheidler P, Kob W and Binder K 2000 *Europhys. Lett.* **52** 277
- [362] Scheidler P, Kob W and Binder K 2000 *J. Physique IV* **10** 33
- [363] Alm eras Y, Barrat J-L and Bocquet L 2000 *J. Physique IV* **10** 27
- [364] Yamamoto R and Kim K 2000 *J. Physique IV* **10** 15
- [365] Varnik F, Baschnagel J and Binder K 2001 *Phys. Rev. E* **65** 021507
- [366] Teboul V and Alba-Simionesco C 2002 *J. Phys.: Condens. Matter* **14** 5699
- [367] Koga K, Zeng X C and Tanaka H 1998 *Chem. Phys. Lett.* **285** 278
- [368] Krakoviack V 2005 *Phys. Rev. Lett.* **94** 065703
- [369] Drake J M and Klafter J (ed) 1989 *Molecular Dynamics in Restricted Geometries* (New York: Wiley)
- [370] McKenna G B 2000 *J. Physique IV* **10** 7–343  
See however for polymer films the recent work by Long D and Lequeux L 2001 *Eur. Phys. J.* **4** 371
- [371] Ngai K L, Riande E and Ingram M D 1998 *J. Non-Cryst. Solids* **235–237** 1
- [372] Simon S L, Park J-Y and McKenna G B 2002 *Eur. Phys. J. E* **8** 209
- [373] Lequellec C, Dosseh G, Brodie N and Alba-Simionesco C, 2005 in preparation
- [374] Jackson C L and McKenna G B 1991 *J. Non-Cryst. Solids* **131–133** 221
- [375] Kremer F 2002 *J. Non-Cryst. Solids* **305** 1
- [376] Sch nhals A, Frick B and Zorn R, private communication
- [377] Zorn R, Hartmann L, Frick B, Richter D and Kremer F 2002 *J. Non-Cryst. Solids* **307–310** 547
- [378] Dubochet J, Adrian M, Teixeira J, Alba C, Kadiyala K, Mac Farlane D R and Angell C A 1984 *J. Phys. Chem.* **88** 6727
- [379] Alba-Simionesco C, Teixeira J and Angell C A 1989 *J. Chem. Phys.* **91** 395
- [380] Wang L M, He F and Richert R 2004 *Phys. Rev. Lett.* **92** 95701
- [381] Reed T M and Gubbins K E 1973 *Applied Statistical Mechanics* (New York: McGraw Hill)
- [382] Coasne B, Czwartos J, Gubbins K E, Hung F R and Sliwinska-Bartkowiak M 2004 *Mol. Phys.* **102** 2149
- [383] Coasne B, Czwartos J, Gubbins K E, Hung F R and Sliwinska-Bartkowiak M 2005 *Adsorption* **11** 301
- [384] Czwartos J, Coasne B, Gubbins K E, Hung F R and Sliwinska-Bartkowiak M 2005 *Mol. Phys.* **103** 3103